CRANFIELD UNIVERSITY

Andrew Potter

The hot corrosion of nickel-base disc alloys

School of applied sciences

MSc Thesis
Academic Year: 2011

Supervisor: Dr N. J. Simms and Dr A. Encinas-Oropesa
November 2011

CRANFIELD UNIVERSITY

School of applied sciences

MSc Thesis

Academic Year 2011

Andrew Potter

The hot corrosion of nickel-base disc alloys

Supervisor: Dr N. J. Simms and Dr A. Encinas-Oropesa
November 2011

Acknowledgements

I would like to acknowledge and thank the supervisors Dr Nigel Simms and Dr Adriana Encinas-Oropesa for giving me the opportunity for further education and greater involvement with the research I have been working on for a number of years previously.

Thanks must also go to Zhai Rongrong, Minh-Anh Tu, Li Xia, Bao Rui and He Yuanyuan for helping me to become a proper research student and showing by example what it means to work hard. Additional thanks must go to Dr Joy Sumner for encouragement and stand in supervision.

Finally my biggest thanks go to my family for unwavering support and without whom I would quite literally not be here today!

Abstract

The efficiency of a jet's engines has a direct affect on its economic and environmental impact through the quantity of aviation fuel consumed and CO_2 emitted. These factors are becoming increasingly important due to higher fuel costs and a greater global awareness of environmental issues.

To date, most of the corrosion research work concerning jet turbines has focused on the hottest parts, the turbine blades vanes and combustion chamber. However, as the engines run hotter and with more stress, new superalloys have also been developed for the turbine disc. Although extensive research has been carried out with regard to the mechanical properties of these alloys, relatively little research has been done into their corrosion resistance.

The aim of this research is to investigate the hot corrosion characteristics of both the existing and more recently developed disc alloys. Based on these data, the corrosion performance of these alloys was modelled and compared.

These aims have been achieved using data from a series of "deposit recoat" corrosion tests on the relevant alloys carried out at Cranfield during the last 6 years. The alloys that are the focus of this study are: Waspaloy, Inconel 718, U720, and RR1000. RR1000 is of particular interest since it is the most recently developed alloy and relatively little is known about its corrosion properties. The tests have been carried over a range of temperatures relevant to the current operating temperatures and the desired higher operating temperatures of the turbine discs. The effects of deposition flux, deposit composition and exposure time have also been investigated as part of this study.

A quantitative assessment of the corrosion damage has been carried out and provided metal loss data which has been used to generate empirical models and to compare the effects of variables. The data generated suggest that in the propagation stage of hot corrosion the rate of corrosion is approximately the same between alloys. Therefore the important factor when modelling a disc alloy's corrosion behaviour is the length of the incubation period.

The changes in elemental composition undergone at the alloy surface during corrosion have been investigated using a scanning electron microscope (SEM) equipped with an energy dispersive X-ray spectroscopy (EDX). The results support the literature in that type II corrosion exhibits no preferential alloy depletion underneath the corrosion deposits.

Contents

List of figures

List of tables

List of equations

1. Introduction

1.1 Project background

The use of aircraft for travel, freight and the military has become an integral part of today's society. Despite the recent economic downturn, the forecast for aviation demand is one of sustained growth. Airbus' global market forecast 2009-2028 [1] predicts the overall world passenger traffic will increase at a rate of 4.7% per annum, this equates to doubling over 15 years as shown in Figure 1.1.

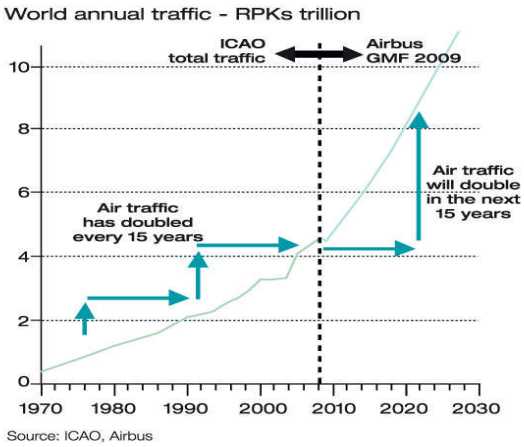

Figure 1.1: Revenue passenger kilometre forecast [1]

The same report stated that the air freight industry had suffered a severe downturn linked to the global economic situation. However, freight traffic is predicted to grow at a rate of 5.2% per annum over the 2009-2028 period as shown in Figure 1.2.

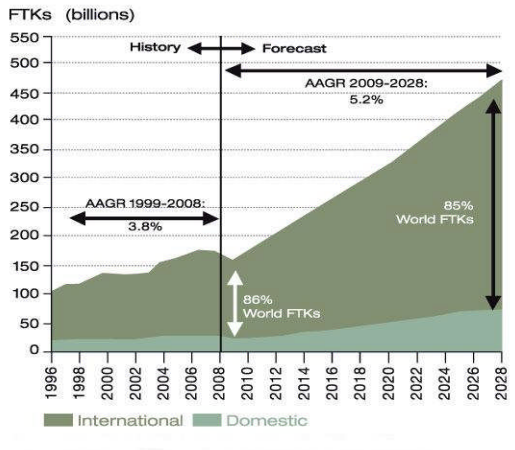

Figure 1.2: Freight ton kilometre forecast [1]

The price of aviation fuel is a very important factor in air freight economics where all passenger related costs are non-applicable. Between the start of 2005 and the middle of 2008 fuel prices rose significantly. This highlighted the inefficiencies of older aircraft and the need to develop more fuel efficient airplanes. It was predicted in the Airbus report [1] that 72% of today's freighters will have retired by 2028, implying that they will need to be replaced by more efficient aircraft.

As the world's population becomes ever more aware of environmental issues, an increasing amount of pressure is being put upon nations and organisations to reduce pollution levels. Gases that contribute to the enhanced greenhouse effect are of particular concern. The greenhouse effect is a process by which gases in the earth's atmosphere have an insulating effect, reducing the amount of heat that can radiate away from the planet [37].

International airline emissions were not included in the 1997 Kyoto protocol [39]. However, in 2009, the European Union legislated that as of 2012, aviation emissions would be included in the EU emissions trading scheme. In addition, the International Air Transport Association made a pledge to reduce carbon emissions by 50 percent by 2050 at their 2009 general meeting [16]. To fulfil these pledges in an expanding market, new technologies must be exploited.

The effects of both current and future projected technologies on aircraft fuel consumption and CO_2 emissions have been investigated in a report by QinetiQ [15]. This report takes into consideration five possible scenarios ranging from no technological improvements to a predicted technology level plus a penalty cost of $100 per tonne of CO_2 emitted. In conclusion this predicts that for the year 2030, in the scenario whereby new technologies are exploited, fuel consumption and CO_2 emissions are 22.5% lower than in a scenario where technology is frozen at the 2002 level[15]. The report also predicts that in the case involving the most technological advance (that with a $100 per tonne CO_2 cost), a fuel consumption and CO_2 emission reduction of 39.7% could be possible[15].

As a result of the widespread use of jet aircraft, small improvements in efficiency can have large financial and environmental impacts. Current research into jet engine development aims to improve fuel efficiency and decrease emissions by burning the fuel at a higher temperature and reducing component cooling. However, such developments present multiple challenges that must be overcome; for example, the greater combustion temperatures tend to produce more NOx. More relevant to this study, the engine hot gas path components must work at higher metal temperatures, or have improved cooling systems/thermal barrier coatings. This can be particularly significant for the components that are exposed to potentially corrosive environments in the power turbine section of the engine, such as blades, vanes and discs [25; 28]. With increasing metal temperatures surface oxidation becomes more significant, but in appropriate environments (alkali salts and sulphur species) these components can also experience hot corrosion in specific metal

temperature regimes. Low temperature (or Type II) hot corrosion peaks at ~ 700 °C, whereas high temperature (or Type I) hot corrosion peaks at ~850-900 [8].

1.2 Aims and objectives

This project aims to investigate the hot corrosion characteristics of both current and newer disc alloy materials under varying hot corrosion exposure conditions. These aims have been achieved by fulfilling a series of objectives which are listed:

A series of corrosion tests investigating the following variables has been carried out to form a corrosion test matrix described in Chapter 3.

- Alloy material: four different disc alloy materials are considered to make up the scope of this study; Waspaloy, Inconel 718, U720, and RR1000. The composition of these alloys is shown in table 2.1. Because RR1000 is a relatively new addition to the superalloy family, comparatively little previous research has been conducted regarding its corrosion performance [5].
- Test length: by varying exposure time, the degradation of each sample over time can be investigated microscopically and models for the material lifespan can be developed.
- Temperature: with engine operating temperature being proportional to fuel efficiency, studying the effects of different temperatures is of great importance. The range of temperatures considered include that of aircraft currently in service and more desired component operating temperatures.
- Deposit composition and quantity: these variables provide an insight into their effect on the hot corrosion process.

Selected samples have had their post exposure morphology investigated using an ESEM (environmental scanning electron microscope) equipped with an energy dispersive X-ray spectrometer (EDX). This allowed comparisons to be made with previous work in the literature and an identification of the chemical reaction taking place during exposures.

Experimental data obtained was plotted to give empirical models showing the effects of the corrosion test variables. These effects are discussed in Chapter 5.

2. Literature Review

This chapter reviews the previous work published with subject matter relating to the hot corrosion of the turbine disc in jet engines. This includes describing the nature of a turbine engine and the materials used for the turbine disc before discussing the chemical processes they undergo during operation.

2.1 Jet turbine engines

The idea of a jet propulsion engine was first patented by the French engineer Rene Lorin in 1913[31]. However the technology available at the time was insufficient to put such a design into practice.

In 1930, Frank Whittle was able to develop the idea and patented a design for a jet turbine engine, however it wasn't until 11 years later that his engine would complete its first flight. A basic schematic of this is shown in Figure 2.1 [31].

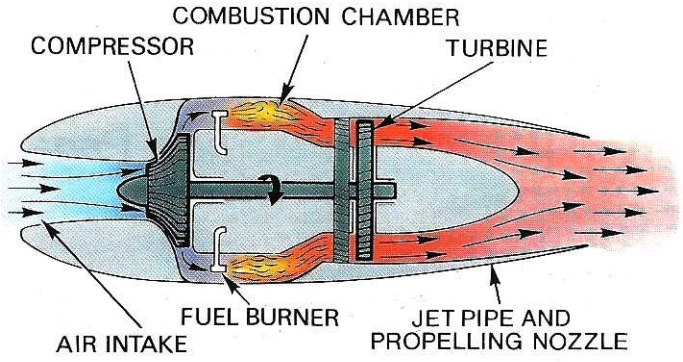

Figure 2.1: Frank Whittle jet turbine engine [31].

In principle a modern jet turbine engine works by taking in air, which is then compressed via a series of rotor blades and stator vanes that decrease in size. The compressed air is then mixed with fuel in a combustion chamber and ignited. The combustion of the fuel causes a rapid expansion of gas, which is then fed through a series of stators and rotors in the power turbine to provide mechanical power for the compressor. Finally the high pressure gas leaves the engine through a nozzle, providing the aircraft with propulsion.

2.1.1 Turbines

The power turbine in most modern jet engines consists of several stages each employing one row of stationary nozzle guide vanes and one row of moving blades. The turbine blade tips may rotate at speeds in excess of 130 meters per second while the gas entering the turbine from the combustion chamber may be travelling at a velocity of over 220 meters per second and with a temperature of between 850 and 1700 °C [32].

One method employed to decrease the turbine component temperature and thus allow higher combustion temperatures is to cool such components with air. Part of the air flow in particular stages of the compressor is siphoned off to cool a corresponding stage of the power turbine. The increase in combustion efficiency more than compensates for the small reduction of air flow through the compressor. However this method for cooling allows contaminants in the air access to the power turbine components. Of specific interest to this study is the deposition of salts found in the atmosphere on the turbine disc.

The speed of the turbine blade has a considerable effect on the efficiency of the engine at each of the stages. Because the stress inflicted on the turbine disc increases exponentially with an increasing revolution speed, to make the engine turn faster thicker engine components must be used and consequently the engine weight increases. Therefore, a compromise must be reached between weight and efficiency. However, if the turbine inlet temperature is increased (or the diverted cooling air is reduced) then the engine can become more thermally efficient and therefore the power to weight ratio can be improved. It is this principle that is the driving force behind the need to use disc alloy materials at higher temperatures.

Because Aviation fuel contains various contaminants, including sulphur [11; 12], upon combustion these species become gaseous and are carried downstream through the turbine section of the engine. These elements play a key role in the corrosion of components of the gas turbine, including the turbine disc.

It should be noted that increasing the combustor temperature also has the undesirable effect of increasing NOx emissions. However there is ongoing research into combustor technology that aims to drastically reduce the quantity of NOx produced from the combustion of fuel [29; 42].

2.2 Disc alloy materials

2.2.1 Superalloys

A superalloy is defined by Sims, Stoloff and Hagel [38] as an alloy developed for elevated temperature service, usually based on group VIIIA elements, where relatively severe mechanical stressing is encountered, and where high surface stability is frequently required.

Over the last 60 years superalloys have seen constant improvements to keep up with the ever increasing demands of aviation and power generation industries. Early developments focused on the removal of impurities through forging in a vacuum. Subsequently, the alloys adopted a casting process, improving the percentage of γ′ in the structure through the technique of precipitation hardening. The more recent superalloys designed for the most demanding applications (such as power turbine blades) have a monocrystalline structure, eliminating the need for grain-boundary strengthening elements such as boron or carbon in the composition [30].

There are three main categories of superalloy: nickel-based, cobalt-based and iron-based. There is also a notable subdivision of the nickel-based superalloys that have a relatively large iron content, known as nickel – iron superalloys. It is nickel-based superalloys that are most often used in the hottest environments where good mechanical strength, creep resistance and corrosion resistance are required. Therefore it is these alloys that are used in the manufacture of modern power turbine discs for jet engines.

2.2.2 Chemical composition

Nickel – based superalloys typically have 9 or more different elemental constituents that are accurately controlled. Most nickel – based alloys contain 5-20 wt.% chromium, up to 8 wt.% aluminium and titanium, 5-10 wt.% cobalt and small amounts of boron, zirconium and carbon. Other common additions to this mixture are molybdenum, tungsten, niobium, tantalum and hafnium. Figure 2.2 shows how the alloying elements tend to be grouped together in the periodic table.

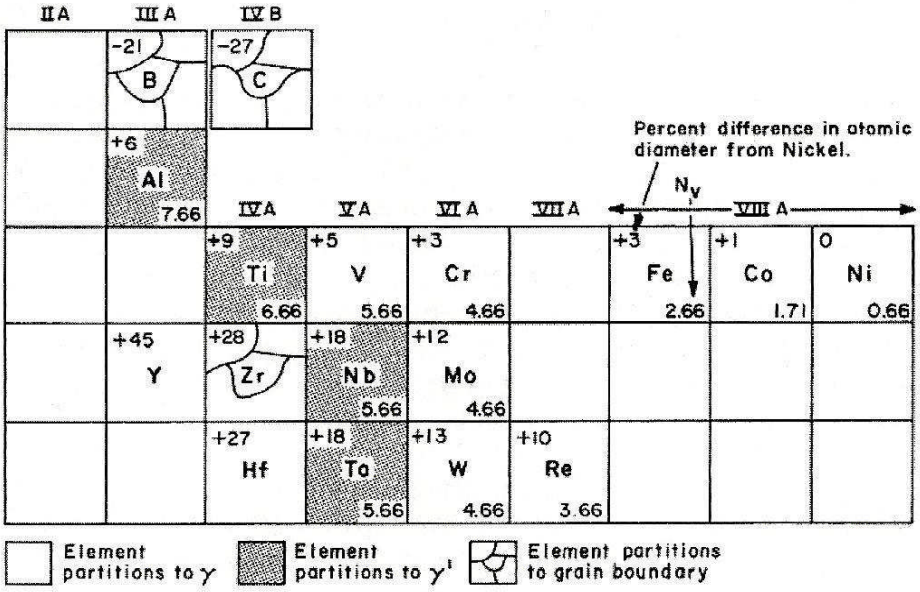

Figure 2.2: The elements used in the composition of nickel-base superalloys [38].

These Elements can be classified into three main groups. The first class consists of elements that adopt the face centred cubic (FCC) austenitic (γ) matrix. These are from groups V, VI, VII and VIII and include nickel, cobalt, iron, chromium, molybdenum and tungsten. The second class of elements are from groups III, IV and V and make up the γ´ precipitate, Ni_3X. These elements include aluminium, titanium, niobium, tantalum and hafnium. The FCC structure of γ and γ´ is shown in Figure 2.3 [30][38]. A third class of elements from groups II, III and IV including boron carbon and zirconium tend to form precipitates along the grain boundaries. These elements are unusual in that the atomic diameter of boron and carbon is significantly smaller than that of nickel, whereas the atomic diameter of zirconium is significantly larger. In addition to these three classifications, there are two subgroups, those that form carbides and those that form oxides [4].

Table 2.1 shows the alloys that make up the scope of this study and their elemental compositions. The materials are listed in chronological order with the oldest first.

Alloy	Cr	Ni	Co	Mo	W	Nb	Ti	Al	Fe	C	B	Zr	Ta	Cu	Hf
Waspaloy	19.50	57.00	13.50	4.30	0.00	0.00	3.00	1.40	2.00	0.07	0.00	0.09	0.00	0.00	0.00
IN 718	19.00	52.00	0.00	3.00	0.00	5.10	0.90	0.50	18.50	0.08	0.00	0.00	0.00	0.15	0.00
U 720LI	16.00	57.00	15.00	3.00	1.20	0.00	5.00	2.50	0.00	0.02	0.01	0.03	0.00	0.00	0.00
RR1000	15.00	52.85	18.00	5.00	0.00	0.00	3.60	3.00	0.00	0.03	0.02	0.00	2.00	0.00	0.50

Table 2.1: Elemental composition (wt.%) of Disc Alloys [4; 14]**.**

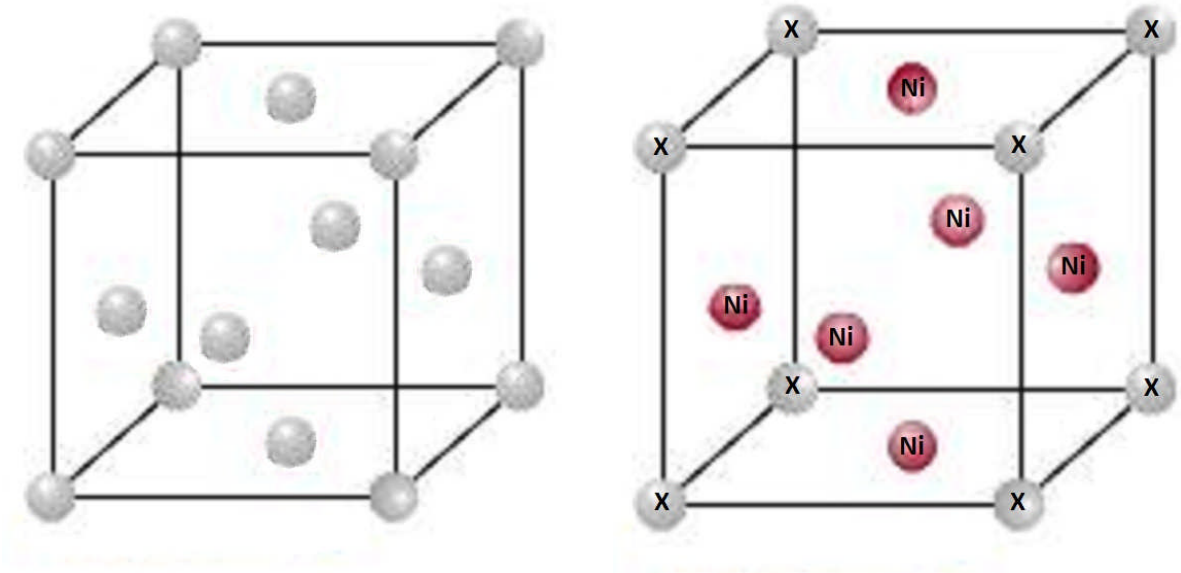

Figure 2.3: (Left) FCC γ structure where the element distribution is random. (Right) FCC structure of γ´ where X could be aluminium, titanium, niobium, tantalum or hafnium.

2.3 High temperature oxidation

The science behind high temperature oxidation has been thoroughly researched and presented by a number of authors [2; 18; 19]. The following theory and equations are common in all of them.

Under most conditions of use metals are thermodynamically unstable with respect to ambient gases. Depending on their composition and the reaction conditions, they will react to form oxides, sulphides, carbides, nitrides etc. or mixtures of reaction products. In dry oxygen atmospheres at room or low temperatures this instability may be of no consequence for many metals because the reaction rates are so low. However, the reaction rates increase rapidly with temperature, and in applications of metals at elevated temperatures the question of oxidation resistance becomes of paramount importance [19].

2.3.1 Thermodynamics of oxidation

The reaction of a pure metal (M) with oxygen (O_2) may be written as:

$$M(s) + O_2(g) = MO_2(s) \qquad \textbf{Equation 1}$$

The change in thermodynamic potential energy, known as Gibbs free energy, is the driving force behind the reaction of metal with oxygen. Thermodynamically speaking, the oxide will only be formed if the pressure of oxygen present is larger than that of the dissociation pressure of the oxide in equilibrium with the metal [19].

Gibbs free energy change for the formation of the oxide shown in equation 1 can be written as:

$$\Delta G^o = -RT \ln\left(\frac{a_{MO_2}}{a_M P_{O_2}}\right) \qquad \textbf{Equation 2}$$

Where a_{MO} is the activity of the oxide, a_M is the activity of the metal, p_{O_2} is the partial pressure of oxygen, R is the gas constant and T is the temperature.

Assuming the pure metal is insoluble in the oxide, the activities of the metal and the metal oxide will be the same. This equation can then be simplified to:

$$\Delta G^{o} = RT\ln\left(P_{O_2}\right) \qquad \textbf{Equation 3}$$

Gibbs free energy of formation of an oxide as a function of temperature and the dissociation pressure of the oxide can be shown in the form of an Ellingham/Richardson diagram such as Figure 2.4 [18]. Although the Ellingham/Richardson diagram shows if a reaction is thermodynamically favourable, it does not show the rate of the reaction.

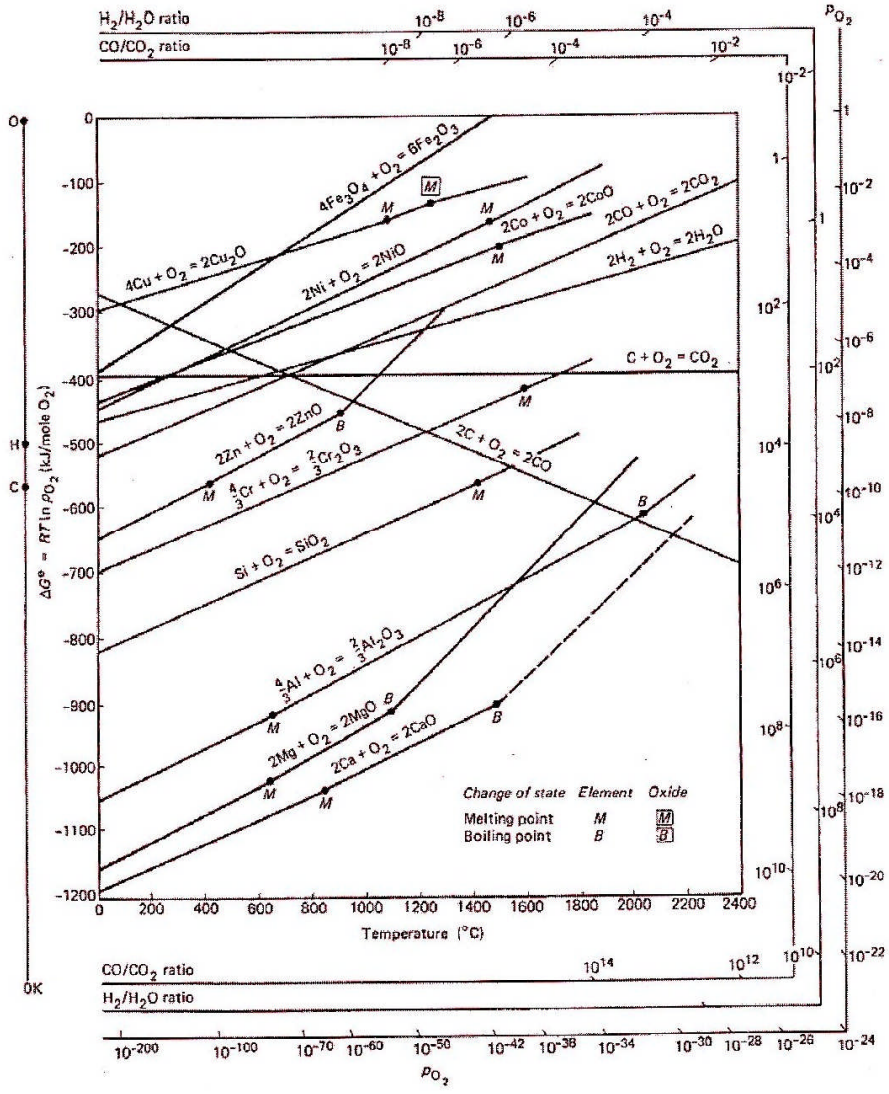

Figure 2.4: Ellingham/Richardson diagram for the formation on various oxides [2].

The more negative the standard free energy change of formation is, the more stable the resulting compound will be. This means that compounds found in the lower part of the Ellingham/Richardson diagrams are more stable than those found in the upper section, and would therefore be able to reduce them. It should be noted that certain experimental inconsistencies have been observed with the Ellingham/Richardson diagram [7]. Reactive elements can promote oxide growth in Cr_2O_3 forming alloys, but have been found to not promote oxide growth in Al_2O_3 forming alloys despite having a more negative $\Delta G°$ than either compound. Theoretically their oxides would be more stable than either Cr_2O_3 or Al_2O_3 and should therefore provide preferential sites for the formation of Cr_2O_3 or Al_2O_3 and thus the selective oxidation of Cr and Al [7].

The presence of metal oxide is of great importance in the study of hot corrosion. Because metal oxides are fundamentally more stable than the parent metal or alloy, they protect the underlying metal from more aggressive forms of attack. However, for the oxide scale to be properly protective it must grow slowly with good integrity and be adherent.

2.3.2 Oxidation mechanisms

If a flawless oxide layer has initially been formed, it is apparent that for the oxidation reaction to continue either metal cations must migrate through the metal oxide scale to react with oxygen or oxygen anions must migrate across the scale to react with the metal. This is demonstrated in Figure 2.5. Previous research has shown that the formation of Cr_2O_3 (which is most relevant to this study) is propagated almost entirely by the outward migration of chromium cations across the oxide scale [13].

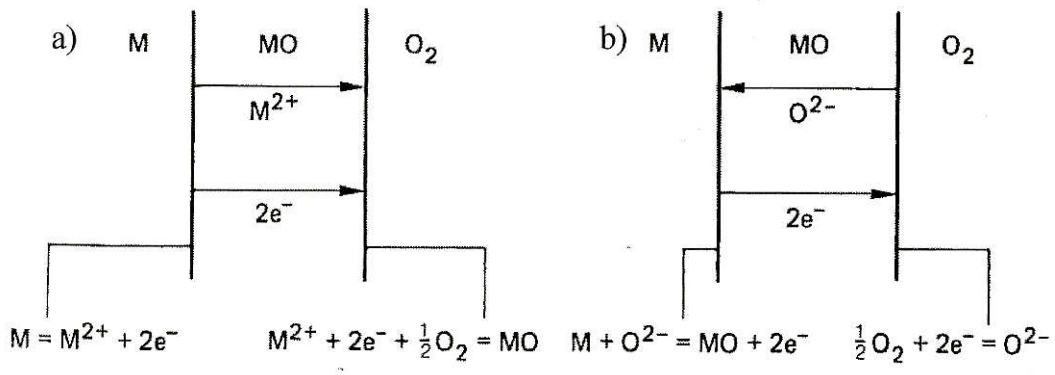

Figure 2.5: The interfacial reactions and both the cation migration (a) and anion migration (b) in the oxidation mechanism [2]**.**

Oxidation rates may vary as a function of time due to a variety of factors. Three main trends have been discovered; logarithmic, parabolic and linear [2; 18]. These three idealistic trends are illustrated in Figure 2.6.

- Logarithmic: This behaviour is commonly observed in metals oxidised at low temperatures (between 300 and 400 °C).
- Parabolic: Oxides that produce a continuous protective oxide scale exhibit this trend. Here it is the transport of cations or anions across the scale that is the rate limiting factor. Metals or alloys for use in high temperature applications generally have a parabolic reaction rate curve.
- Linear: With this behaviour, the reaction rate remains constant. This is observed when the speed of the metal-oxygen reaction is the rate limiting step; the thickness of the oxide scale has no bearing on the reaction rate.

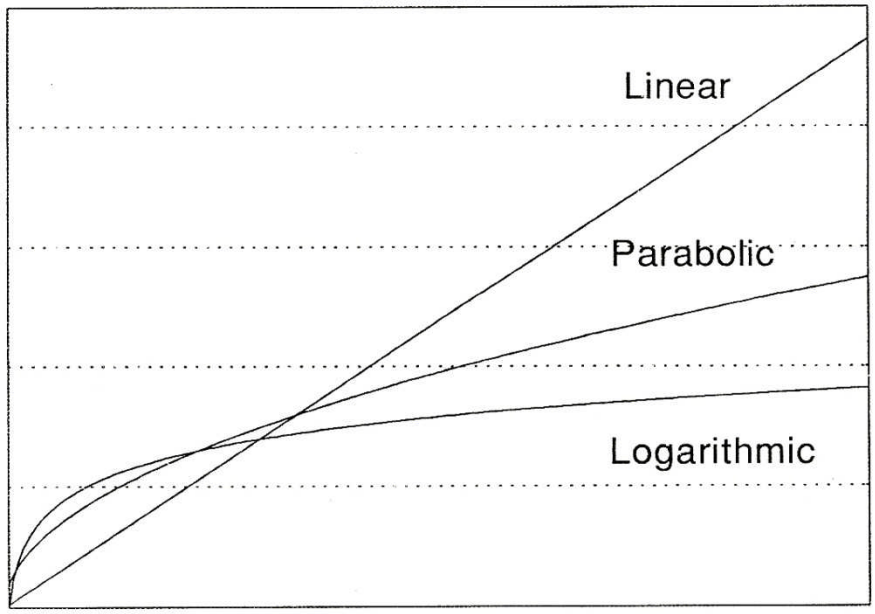

Figure 2.6: Schematic showing the oxidation rate laws [36]**.**

An alloy, or alloy coating, can be designed to grow a particular protective oxide scale with good integrity by carefully controlling its composition. This allows the oxide scale to be chosen to match the specific requirements of the alloy's operating conditions [33]. An oxide map such as Figure 2.7 can be used to determine which oxide will be predominant and form the protective scale.

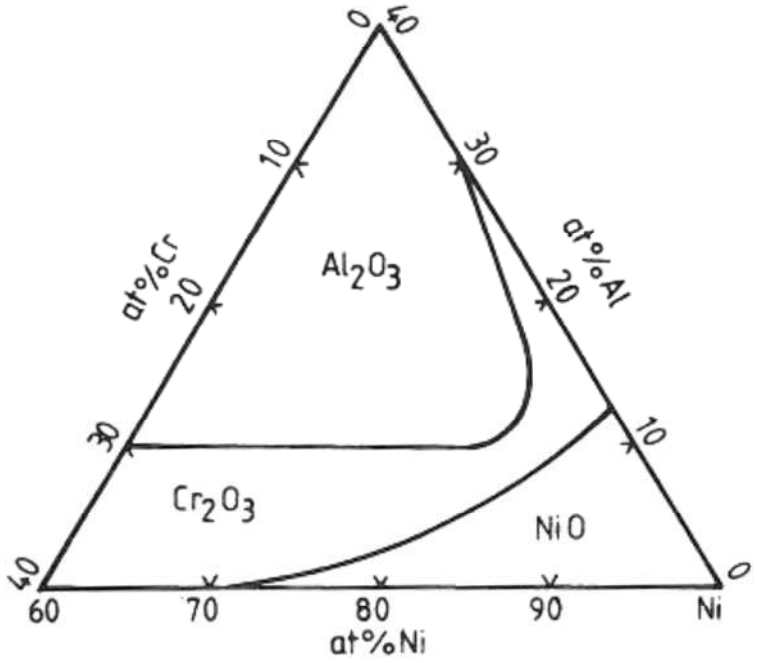

Figure 2.7: Oxide map of a Ni-Cr-Al system at 1100°C [33]**.**

2.3.3 Transient oxides

Transient oxides are relatively small amounts of oxide formed during the initial stages of oxidation that can end up being situated above or within the continuous protective oxide scale that forms later. When a fresh alloy surface is exposed to oxygen for the first time, each element for which it is thermodynamically favourable to do so, will begin to form an oxide nuclei. Eventually, depending on relative abundance, affinity for oxygen, oxide thickening rate and oxide lateral spread rate, one element will form a continuous oxide scale [40; 41]. This process is shown schematically for Ni-Cr binary alloys in Figure 2.8. As discussed in section 2.2, the superalloys that make up the scope of this study have a relatively large number of element constituents and therefore can potentially form a complicated array of transient oxides [35]. A study by Chen et al [17] used X-ray diffraction

to detect the oxides Cr_2O_3, TiO_2 and $NiCr_2O_4$ that had formed in the external scale of Waspaloy and Udimet 720 after isothermal oxidation in air at 750°C.

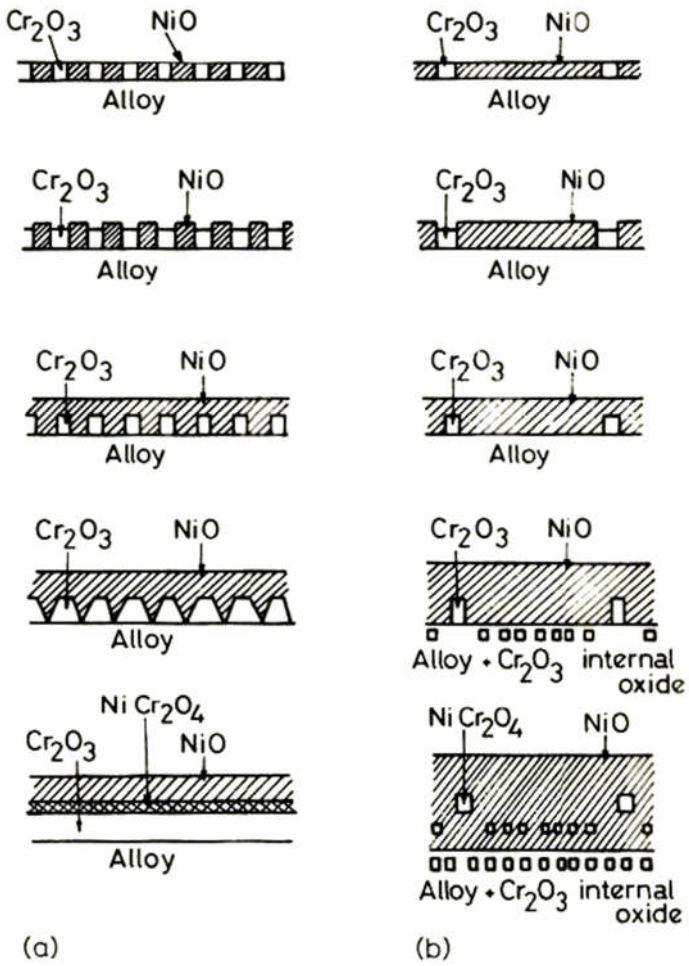

Figure 2.8: Schematic diagram of transient oxidation for Ni-Cr alloys that are (a) Cr-rich and (b) Cr-lean [40]**.**

2.4 High temperature corrosion

The lifespan of certain jet engine components, such as turbine blades and discs, is often limited by a particularly aggressive mode of attack known as hot corrosion; a process that has been defined as “The deposit modified gas induced degradation of metals and alloys” [36].

The phenomenon of hot corrosion was first noticed in boilers, gas turbines and combustion systems during the 1940s. However, it wasn’t until the 1960s that the problem gained importance and attracted increased interest as severe corrosion was found to be afflicting the gas turbine engines of military aircraft during the Vietnam conflict [27]. Initial analysis of corroded components revealed the formation of sulphides of nickel and chromium and therefore the process was initially known as sulphidation. However, follow up research [9][3] revealed that the formation of the sulphides was in fact due to reactions with a thin layer of molten salt deposited on the component’s surface. Because this process resembles in some ways traditional atmospheric corrosion with an aqueous film at ambient temperatures, it has been termed hot corrosion. However research has shown that, where atmospheric corrosion most often occurs through reactions with oxygen dissolved in the aqueous film, the soluble oxidant in the fused salt during hot corrosion is SO_3 that is in one view believed to form $S_2O_7^{2-}$ ions [27].

Studies into this field have established several models for the various mechanisms that the hot corrosion process may use; these are described in a number of publications e.g. [2; 18; 19].

Hot corrosion can be categorised into two different types dependant on the temperatures involved; type I and type II. Type I hot corrosion typically occurs at approximately 900°C; well above the melting point of the salt deposit. This type of corrosion features a uniform attack of the alloy surface with characteristic internal sulphidation of the base alloy. As the temperature is decreased from 900°C, the corrosion rate is reduced until it peaks again between 650°C and 700°C. In this temperature range the salt deposit is well below its melting point. However, the deposit is able to form a eutectic mixture with the oxidation products of the alloy in the presence of ambient SO_3. This mode of corrosion is termed type II and unlike type I the corrosion distribution is frequently irregular (often referred to as pitting) with little or no internal sulphidation of the base alloy.

2.4.1 Degradation sequence

C.S. Giggins and F.S. Pettit proposed a theory that hot corrosion consists of two stages; initiation followed by propagation [8].

In the first stage (initiation), the rate of attack is relatively slow, similar to that in the absence of any deposit, and can often be characterised by a slight increase in sample weight [8]. During this stage the alloy surface and oxide scale is being altered, making the alloy more susceptible to attack. This manipulation may include the diffusion of sulphur through the oxide scale, the depletion of the elements in the alloy that form the oxide scale, the dissolution of oxides into the salt deposit or the development of cracks, stresses or spalling of the oxide layer. The transition from the initiation stage to the propagation stage occurs when there is a failure of the protective oxide scale, allowing molten salt to access and react with the alloy. The propagation stage is characterised by a rapid and catastrophic increase in the corrosion rate. Such an increase in the rate of corrosion usually heralds the imminent failure of the component [2; 18; 19].

Figure 2.9 shows the initiation and propagation stages for three different kinds of oxidation/corrosion tests in terms of net weight change. It can be seen that the length of the initiation stage can vary greatly. Depending on the composition of the alloy, deposit and gaseous environment, the temperature, pressure and whether the component experiences high temperatures in a series of cycles, this stage could be thousands of hours or merely seconds [2]. Because there is currently no way to prevent hot corrosion from occurring in the environmental conditions that allow it, the approach taken to improve an alloys corrosion performance is to extend the length of the initiation stage as far as possible.

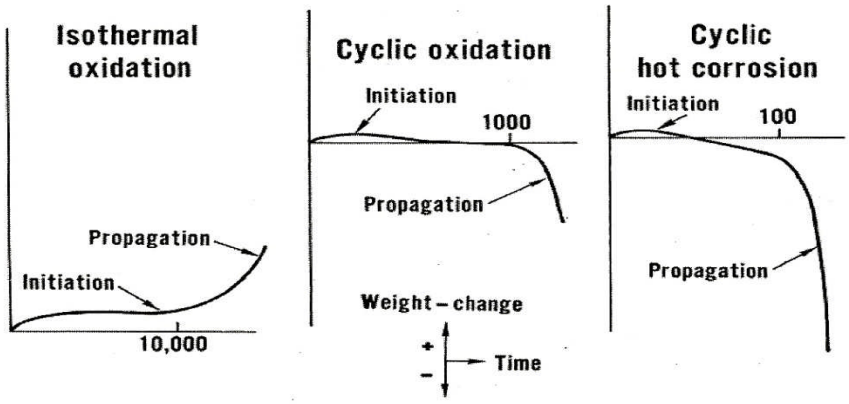

Figure 2.9: Weight change versus time curves illustrating the initiation and propagation stages of the corrosion sequences for isothermal oxidation, cyclic oxidation and cyclic hot corrosion [8]**.**

It is generally accepted that for hot corrosion of either type to take place, a molten salt phase is required. The melting point of pure Na_2SO_4 is 884°C; however there are several methods by which the melting point of a deposit may be lowered.

In practical applications, salt deposits are unlikely to be pure and may have a number of different constituents. Phase diagrams such as Figure 2.10, can show how a mixture of salts may have a lower melting point than any of its individual components.

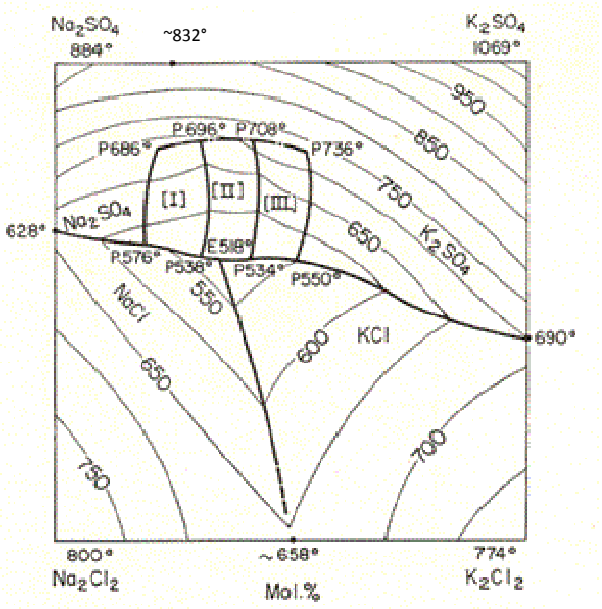

Figure 2.10: Phase diagram for a Na_2SO_4, NaCl, K_2SO_4 and K_2Cl_2 system. I, II and III are unknown interior phases (temperatures in °C) [20]**.**

At lower temperatures a deposit may react with SO_3 (present in most combustion systems) to form a product with a lower melting point. The following equation shows the formation of $Na_2S_2O_7$, which has a melting point of 401 °C.

$$Na_2SO_4 + SO_3 = Na_2S_2O_7 \qquad \textbf{Equation 4}$$

In addition to reacting with the ambient gas, reactions may also occur between the deposit, the oxide scale and any transient oxides to form a complex mixture of salts.

2.4.2 Thermodynamics

After a salt deposit becomes established on the surface of an alloy, either the reactants from the ambient gas must diffuse through the deposit to react with the alloy/oxide or elements of the alloy/oxide must dissolve into the deposit to reach the gas interface. Such a diffusion of reactants through the deposit may cause changes to the reactants composition [2].

Na_2SO_4 is commonly a large constituent of the salt deposits found in power generation and jet turbine applications [6]. Na_2SO_4 can be divided into basic and acidic parts with the following equation:

$$Na_2SO_4 \leftrightarrow Na_2O_{(basic)} + SO_{3(acidic)} \qquad \textbf{Equation 5}$$

This equation can be expressed in terms of the activity of the separate components:

$$a_{Na_2O}\, a_{SO_3} = constant(K) a_{Na_2SO_4} \qquad \textbf{Equation 6}$$

If the activity of Na_2SO_4 is assumed to be 1, this equation shows that the activity of Na_2O is related inversely to the activity of SO_3.

A thermodynamic stability diagram for the Na–O–S system is shown in Figure 2.11. This shows how the Na_2SO_4 melt is able to become either more acidic or more basic depending on the partial pressure of SO_3 and consequently the activity of Na_2O. Because of this amphoteric behaviour, the fluxing mechanisms for hot corrosion can be broadly categorised into two kinds; acidic fluxing and basic fluxing.

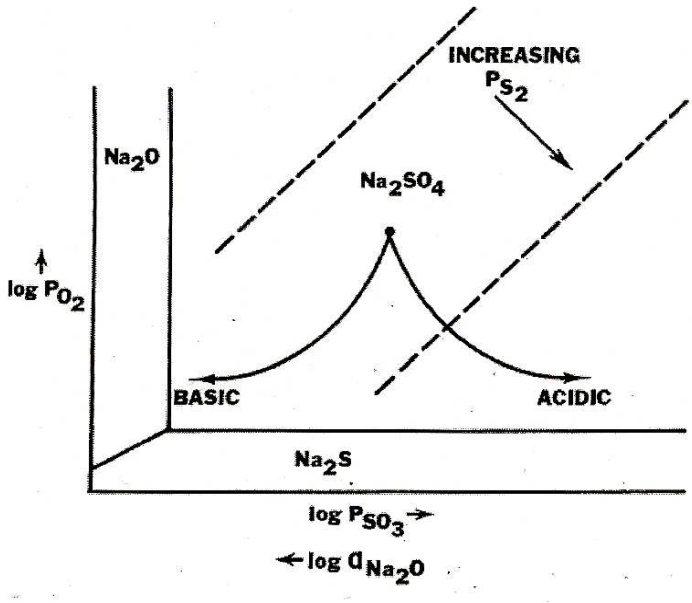

Figure 2.11: Thermodynamic stability diagram for the Na – O – S system [38]**.**

Solubility measurements of various relevant oxides in fused Na_2SO_4 at 1200K have been compiled [27] and are shown in Figure 2.12. The shapes of the curves produced by these data are explained by the formation of a single acid solute and a single basic solute for each oxide upon dissolution. Figure 2.12 also shows how conditions that lead to the basic dissolution of one oxide may lead to the acidic dissolution of another. The operation of gas turbines in practical environments often involves a partial pressure of SO_3 in the range that both Al_2O_3 and Cr_2O_3 have their lowest solubility. This makes the oxide scale formed by these metals particularly effective at protecting gas turbine components.

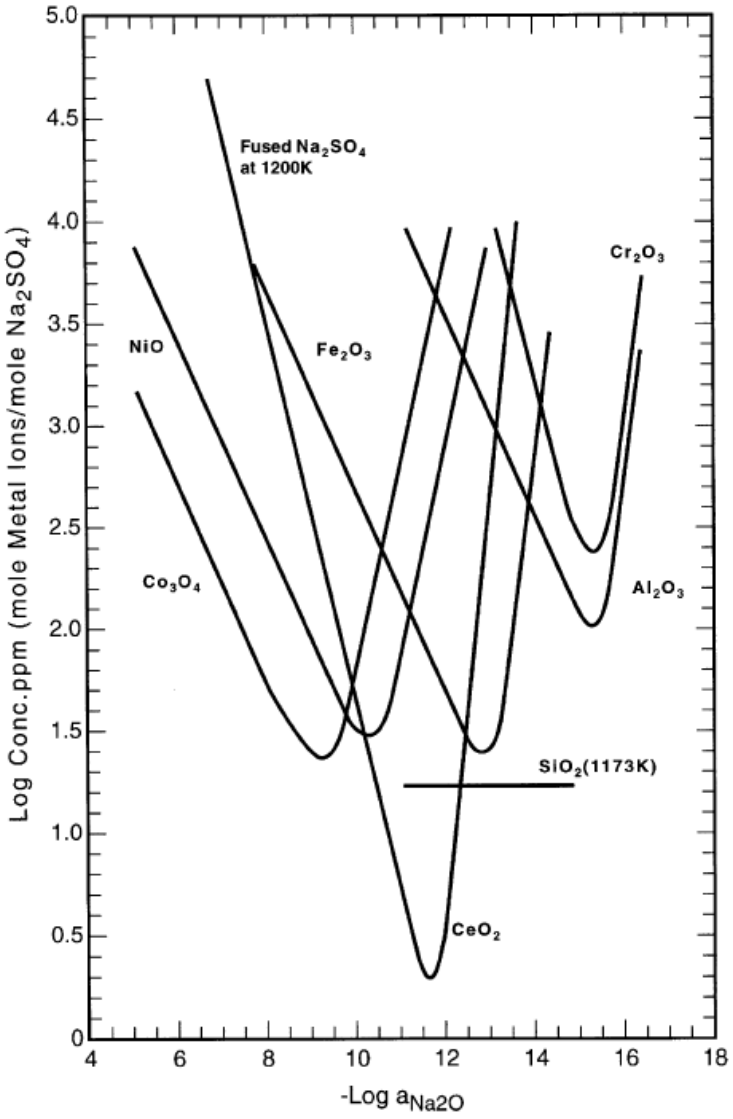

Figure 2.12 The solubility of various oxides in fused Na_2SO_4 at 1200K [27]**.**

2.4.3 Basic Fluxing

As already discussed, basic fluxing prevails when SO_3 is either absent or present with a sufficiently low partial pressure [2]. For this reason the mechanism will be described in terms of the degradation of nickel in oxygen. This process has been presented schematically in Figure 2.13. Initially, nickel oxide is formed on the surface of the nickel. However some of the oxygen for this reaction is taken from the Na_2SO_4 deposit, this in turn causes the sulphur potential in the Na_2SO_4 melt to increase. Consequently, sulphur from the melt is able to penetrate the nickel oxide scale and form a layer of nickel sulphide below it.

The removal of sulphur and oxygen from the Na_2SO_4 melt has the effect of increasing the oxide-ion concentration and therefore the activity of Na_2O. This is shown in the following equations using hypothetical intermediate compounds:

$$SO_4^{2-} = O^{2-}{}_{(in\ Na_2SO_4)} + \tfrac{3}{2}O_2\ (used\ to\ from\ NiO) + \tfrac{1}{2}S_2\ (used\ to\ form\ NiS) \qquad \textbf{Equation 7}$$

$$Na_2SO_4 = Na_2O\ _{(in\ Na_2SO_4)} + \tfrac{3}{2}O_2\ (used\ to\ form\ NiO) + \tfrac{1}{2}S_2\ (used\ to\ form\ NiS) \qquad \textbf{Equation 8}$$

Since these reactions occur at the interface of the deposit and the metal oxide scale, a solubility gradient exists across the fused salt layer. As NiO_2^{2-} ions diffuse away from the metal oxide scale, they decompose into NiO (which precipitates out into particles) and O^{2-} ions. These NiO paricles (now distributed towards the outside of the deposit) do not form a continuous protective layer and so the initial protective NiO scale has been destroyed [2].

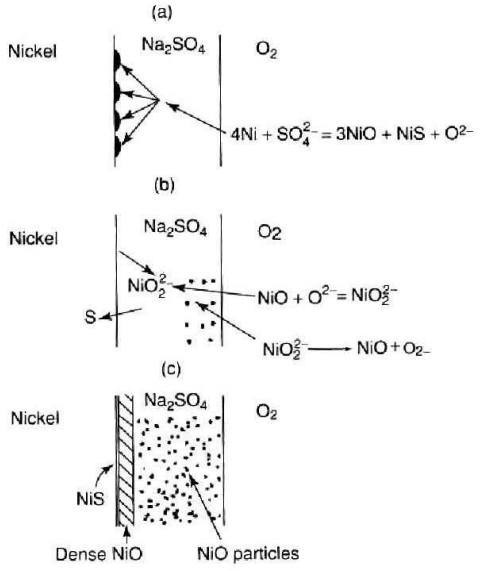

Figure 2.13 Mechanism for the Na_2SO_4 induced accelerated oxidation of nickel in oxygen [2]**.**

Because this reaction involves the removal of sulphur from Na_2SO_4, over time the sulphur activity potential in the deposit will decrease until this deposit can no longer react with the nickel. Therefore this reaction is not self sustaining and can only continue if there is further deposition of Na_2SO_4.

It has been noted that alloys forming Cr_2O_3 protective oxide scales are particularly effective in resisting this kind of accelerated oxidation attack. Cr_2O_3 is able to establish an oxide ion activity within the Na_2SO_4 melt that is insufficient to cause basic fluxing while being too high to allow acidic fluxing [10].

2.4.4 Acidic fluxing

Acidic fluxing can be subdivided into two different mechanisms: alloy induced acidic fluxing, where the acidic conditions result from reactions of certain species in the alloy, and gas phase induced acidic fluxing where reactions with the gas phase establish the acidic conditions [19].

Alloy induced acidic fluxing

This form of acidic fluxing results from the formation of certain oxides such as MoO_3, V_2O_5 and WO_3 in the molten salt deposit. As discussed in section 2.2, Mo, V and W are common constituents of superalloys used in high temperature applications. By reducing the concentration of these elements in the alloy, the effect of this kind of corrosion can be reduced; however this may adversely affect the characteristics of the alloy unless other alloying elements are added to compensate.

A model for the mechanism of alloy induced acidic fluxing has been proposed [10], and is described schematically in Figure 2.14 for a Ni-31Al-Mo alloy. This suggests that, in addition to MoO_3 formed prior to the development of the protective Al_2O_3 scale, MoO_3 is able to form from Mo rich particles in the alloy. The formation of this oxide reduces the oxide ion activity within the Na_2SO_4 and therefore produces acidic conditions. As a consequence, oxide ions from the Al_2O_3 scale are donated to the modified Na_2SO_4 melt which results in the breaking down of protective layer. Vaporisation of MoO_3 at the deposit/gas interface produces a region of low MoO_3 activity which allows Al_2O_3 to precipitate out forming a porous non protective layer. This reaction can be said to be self-sustaining because MoO_3 can be continuously produced from the alloy [10].

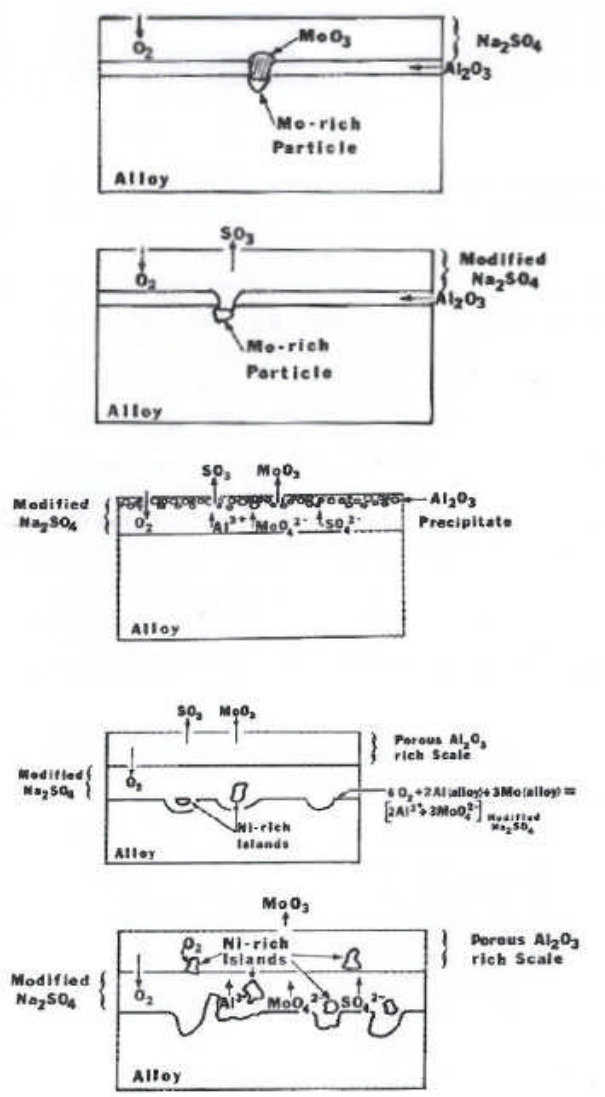

Figure 2.14: The alloy induced acidic fluxing model for Ni-31AL-Mo [10]**.**

The typical reactions undergone by Mo in this process are listed below [2]:

$$Mo + \tfrac{3}{2}O_2 = MoO_3 \qquad \textbf{Equation 9}$$

$$MoO_3 + Na_2SO_4 = Na_2MoO_4 + SO_3 \qquad \textbf{Equation 10}$$

$$Al_2O_3 + 3MoO_{3\,(in\,Na_2SO_4)} = 2Al^{3+} + 3MoO_4^{2-} \qquad \textbf{Equation 11}$$

$$Cr_2O_3 + 3MoO_{3\,(in\,Na_2SO_4)} = 2Cr^{3+} + 3MoO_4^{2-} \qquad \textbf{Equation 12}$$

$$3NiO + 3MoO_{3\,(in\,Na_2SO_4)} = 3Ni^{2+} + 3MoO_4^{2-} \qquad \textbf{Equation 13}$$

Gas phase induced acidic fluxing

This mechanism pertains to type II or low temperature hot corrosion; operating in a temperature range between approximately 650 and 750°C. In this type of acidic fluxing, the acidic conditions are caused by reactions between the gas phase and the deposit. Examples of these reactions are shown below [2].

$$SO_3 + O^{2-} = SO_4^{2-}$$ **Equation 14**

$$SO_3 + SO_4^{2-} = S_2O_7^{2-}$$ **Equation 15**

It can be seen from these equations that the reactions, and therefore the severity of corrosion, are dependent on the pressure of SO_3 in the gas phase. If the temperature is increased towards 800°C, the SO_3 partial pressure consequently decreases and less sulphate ions can form. In addition, at higher temperatures a protective Cr_2O_3 scale can form more quickly which would have the effect of slowing corrosion rates.

An initial mechanism for this reaction was suggested by Luthra and Shores [21] based on the corrosion of Ni-30Cr and Co-30Cr alloys. The authors proposed that the transient oxides of Ni or Co respectively come into contact with the Na_2SO_4 deposit while SO_3 is present in the gas phase. $NiSO_4$ and $CoSO_4$ then form via the following reactions:

$$NiO + SO_3 = NiSO_4$$ **Equation 16**

$$CoO + SO_3 = CoSO_4$$ **Equation 17**

$$\tfrac{1}{3}Co_3O_4 + SO_3 = CoSO_4 + \tfrac{1}{6}O_2$$ **Equation 18**

This contamination of the deposit has the effect of lowering its melting point via the formation of eutectics and a liquid phase may form. Other possible methods for the formation of a liquid phase (discussed in section 2.4.1) include the formation of low melting point compounds such as $Na_2S_2O_7$ or eutectic $Na/K/SO_4/Cl$ mixtures. Once a liquid phase has formed, the rapid sulphation of Ni or Co oxides prevent a continuous protective Cr_2O_3 scale from forming and the alloy can be attacked directly. Their research showed that minimising the growth of transient oxides prior to exposure had the effect of retarding the corrosion process, but could never stop it completely.

Because the protective oxide scale plays an important part in the rate of type II corrosion; it should be carefully considered. For good corrosion resistance, the alloy should include a sufficient concentration of the element that produces the protective scale. In addition, a heat treatment process can allow the oxide scale to fully establish itself as continuous and sufficiently protective.

2.4.5 Corrosion morphology

As previously explained; hot corrosion can be defined either as type I or type II. A key feature of this distinction, other than the mechanism, is the difference in the alloy surface and corrosion product morphology.

Visual inspection of a corroded alloy can only provide limited information as to the nature of the corrosion attack. Observations can vary greatly depending on composition of the sample alloy, however the formation of adhered corrosion product, the spalling of oxide scale and corrosion product, and changes to the colouration of the alloy surface are all common.

Microscopic investigation of a cross section through a corroded alloy can reveal more exact information regarding the type of corrosion attack. Type I corrosion is characterised by a honeycomb structure at the surface of the alloy and sulphide particles formed internally in the alloy. This is accompanied by the depletion of alloying elements in and below the internal sulphide zone. These features tend to be continuous and even; distributed over the whole of the afflicted surface of the alloy. Type II corrosion exhibits an uneven distribution of attack often forming pit like features (referred to as pitting). In addition, because there is an ionic gradient across the molten deposit, different corrosion product species form in different places. Oxides of nickel and cobalt tend to be situated at the gas-deposit interface while oxides and sulphides of other alloying elements such as chromium aluminium and titanium precipitate out at the deposit-metal interface. The result of this is that the corrosion product tends to build up in layers that may or may not spall away. Finally, little or no depletion of the alloying elements is found internally to the alloy below type II damage. The features of both type I and type II corrosion are displayed in Figure 2.15.

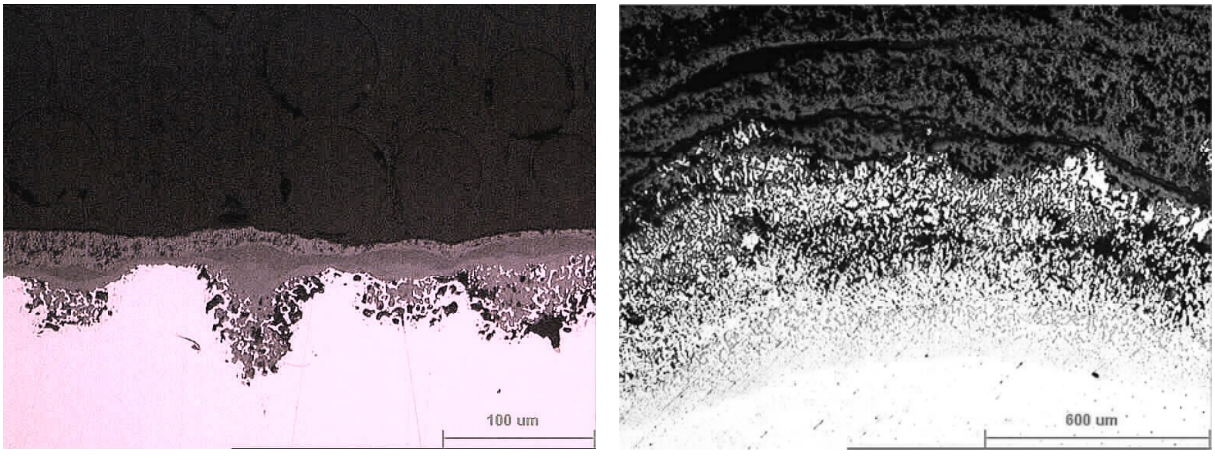

Figure 2.15: Typical morphological features of type II (left) and Type I (right) hot corrosion [6]**.**

2.5 Literature review summery

In this chapter the literature of topics relating to the hot corrosion of power turbine discs has been reviewed. The most relevant points to this research are as follows:

- The disc component of a jet power turbine is exposed to salt deposition and SO_2 at temperatures in excess of 650°C during takeoff and climb.
- The thermal efficiency of the engine can be improved by operating at a higher temperature.
- Superalloys used in turbine discs are designed to withstand large stresses at high temperature. Their composition is such as to oxidise to form a continuous scale of either Al_2O_3 or Cr_2O_3.
- The oxide scale of a superalloy forms, at a parabolic rate, a protective layer that is less reactive than the alloying elements found underneath.
- Hot corrosion can be defined as a deposit modified, gas induced degradation of metals. For hot corrosion to occur the deposit must enter a molten state, this can be achieved via the formation of eutectic mixtures and reactions with the gas phase.
- Type II hot corrosion involves the chemical breakdown of the protective oxide scale exposing the alloy to further more rapid attack. The rate for type II hot corrosion peaks at approximately 700°C.

The next chapter will describe the experimental test procedures and the methods used to measure the degree of corrosion and further investigate the changes in morphology. Details of the experimental program and the corrosion test matrix are also given.

3. Experimental Procedures

This chapter details the scope of the experimental work carried out and describes how they were completed practically. Finally, the techniques employed post exposure to assess the degree of corrosion and investigate the changes in surface morphology are discussed.

As stated in Chapter 1, 9 corrosion tests make up the scope of this study. Each test was run with its own specific objectives (for reasons not related to this MSc project). However, samples from these tests may be linked as follows:

- Test 1: compares the older Waspaloy and U720 disc alloys with the more recent RR 1000 at the more desired component temperature of 700°C. The test parameters of 300ppm of SO_2 in air, using 10µm/cm²/h of 98% Na_2SO_4 2% NaCl deposit were designed to replicate the corrosion conditions found in a practical environment.
- Test 2: Follows up on test 1 by keeping the test conditions the same but altering the deposit composition and quantity independently of each other on Waspaloy, U720 and RR 1000 samples.
- Tests 3 and 4: at 700°C and 750°C respectively, with 300ppm of SO_2 in air, and a deposit flux of 10µm/cm²/h of 98% Na_2SO_4 2% NaCl. The RR1000 samples were subjected to shot peening prior to exposure. This process involved bombarding the alloy surface with glass or ceramic beads to compress and can deform the outer grains and promote oxide scale growth.
- Tests 5, 6, 7 and 8: these tests investigated the corrosion performance of IN718, Waspaloy, U720 and RR1000 at 620, 650 and 700°C with an atmosphere of 300ppm of SO_2 in air, using 10µm/cm²/h of 98% Na_2SO_4 2% NaCl deposit.
- Test 9: RR1000 with a coarse grain size, exposed at 700°C with 300ppm of SO_2 in air, and a deposit flux of 10µm/cm²/h of 98% Na_2SO_4 2% NaCl.

The sample test matrix (table 1.2) is made up from 9 separate corrosion tests covering the variables listed in Chapter 1.2. Because each test had its own specific objectives, there are certain duplicate samples within the test matrix.

			Salt		Corrosion test length				
Test number	Sample Material	Temperature °C	Type	Flux µg/cm²/h	100	200	300	400	500
1	Waspaloy	700	2% NaCl 98% Na_2SO_4	10		X	X		X
1	U720	700	2% NaCl 98% Na_2SO_4	10		X	X		X
1	RR 1000	700	2% NaCl 98% Na_2SO_4	10		X	X		X
2	U720	700	5% NaCl 95% Na_2SO_4	10		X	X		X
2	U720	700	2% NaCl 98% Na_2SO_4	2		X	X		X
2	Waspaloy	700	5% NaCl 95% Na_2SO_4	10		X	X		X
2	Waspaloy	700	2% NaCl 98% Na_2SO_4	2		X	X		X
2	RR 1000	700	5% NaCl 95% Na_2SO_4	10		X	X		X
2	RR 1000	700	2% NaCl 98% Na_2SO_4	2		X	X		X
3	RR 1000	700	2% NaCl 98% Na_2SO_4	10		X			X
4	RR 1000	750	2% NaCl 98% Na_2SO_4	10		X			X
5	IN718	620	2% NaCl 98% Na_2SO_4	10	X	X			
5	Waspaloy	620	2% NaCl 98% Na_2SO_4	10	X	X			
5	U720	620	2% NaCl 98% Na_2SO_4	10	X	X			
5	RR 1000	620	2% NaCl 98% Na_2SO_4	10	X	X			
6	IN718	650	2% NaCl 98% Na_2SO_4	10	X	X			
6	Waspaloy	650	2% NaCl 98% Na_2SO_4	10	X	X			
6	U720	650	2% NaCl 98% Na_2SO_4	10	X	X			
6	RR 1000	650	2% NaCl 98% Na_2SO_4	10	X	X			
7	IN718	700	2% NaCl 98% Na_2SO_4	10	X	X			
7	Waspaloy	700	2% NaCl 98% Na_2SO_4	10	X	X			
7	U720	700	2% NaCl 98% Na_2SO_4	10	X	X			
7	RR 1000	700	2% NaCl 98% Na_2SO_4	10	X	X			
8	IN718	650	2% NaCl 98% Na_2SO_4	10					X
8	Waspaloy	650	2% NaCl 98% Na_2SO_4	10					X
8	U720	650	2% NaCl 98% Na_2SO_4	10					X
8	RR 1000	650	2% NaCl 98% Na_2SO_4	10					X
9	RR 1000	700	2% NaCl 98% Na_2SO_4	10	X	X			X

Table 3.1: Sample testing matrix

Disregarding the manufacture of the samples, the process of corrosion testing can be divided into five parts: sample preparation and pre exposure metrology, corrosion test, post-test sample preparation, sample analysis (including microscopy and dimensional metrology) and data analysis.

3.1 Sample preparation

Each sample underwent the following procedure to prepare them for the corrosion test:

• Cutting: the samples were provided from the manufacturer in the form of a bar made up from a series of bobbins. The bobbins were separated from the bar using a precision saw with a CBN cut off wheel. The cut was made so as to allow a small protrusion at the base for the sample to sit on, and a larger one at the top to aid handling the sample with tweezers.

Once separated from the bar, a notch was made on the top protrusion with a dremel. This notch would act as a reference to give the cylindrical sample an orientation while measuring.

• Cleaning: the samples then went through a two stage cleaning process. In the first stage the samples were ultrasonically cleaned in a beaker of volasil for ten minutes. The purpose of this was to remove any oil contaminants from the sample. The second stage involved ultrasonic cleaning in propanol for a further ten minutes. This removed all traces of the volasil and any other contaminants.

• Metrology: each sample was assigned a code and position number for the purpose of identification and the dimensions were measured using a micrometer with a resolution of ±0.001mm. The samples diameter was measured at eight equally spaced intervals around the circumference of each sample. This data is used to calculate the surface area and also provide a dimensional comparison with regard to metal loss at the end of the test.

• Crucible preparation: in preparation for the test, the crucibles that would hold the samples also went through a cleaning process. Each crucible was ultrasonically cleaned in propanol for ten minutes before being heat treated at 1000°C for 24 hours.

• Initial weight data: immediately before the start of the test, the sample weight was recorded using a fully calibrated balance measuring in grams to five decimal places. Each crucible was also weighed to allow the degree of sample spalling to be calculated.

• Reference sample: one sample of each material underwent exactly the same pre-test procedure but was not exposed. These samples were used as a reference to provide a comparison with samples exposed in the various tests.

3.2 Corrosion tests

The samples were exposed to the corrosive environment using a vertical tube furnace with an alumina reaction vessel, as shown in Figure 3.1. Before exposing the samples, the temperature profile of the furnace was measured and calibrated to ensure accuracy. The sample containing crucibles were suspended in the hot zone (defined as ±5°C of the target temperature) of the furnace on a six layer alumina ceramic carousel with a capacity for twenty four samples.

The test gas was admitted to the bottom of the reaction vessel through an alumina tube that connects to the sealing plate and supports the sample carousel. The gas flow was limited to fifty standard cubic centimetres per minute by a pre-calibrated mass flow controller upstream of the test vessel.

The exhaust gas passes through an NaOH scrubber solution to remove acid gas species, before being vented to the atmosphere from the roof of the lab. The first scrubber bottle in the exhaust line is empty to prevent the scrubber solution being sucked back into the furnace in the event of a power failure.

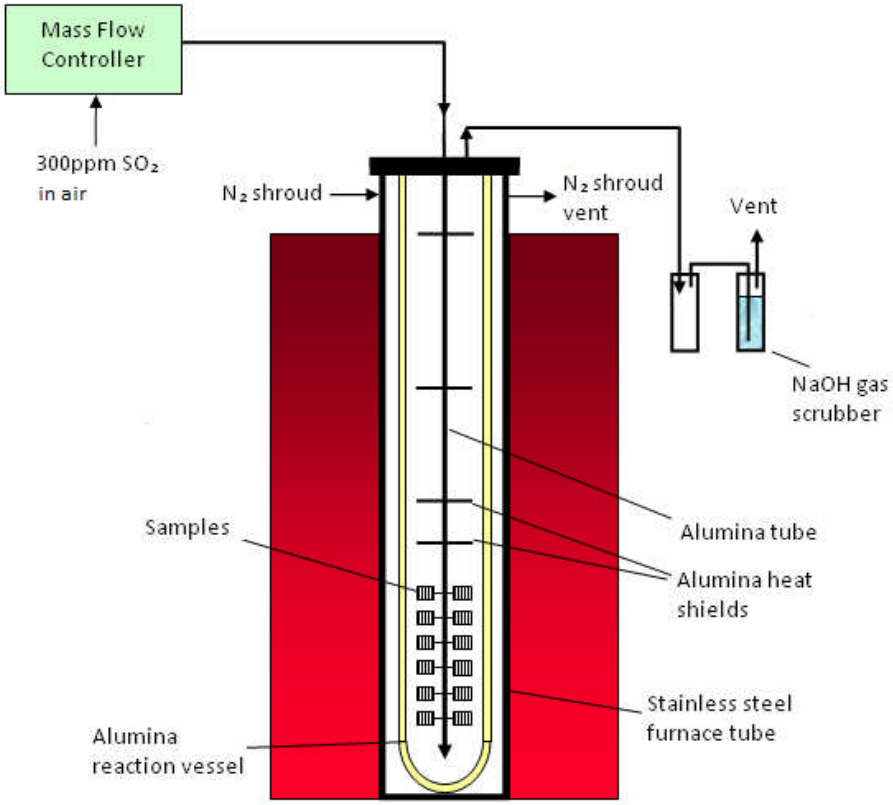

Figure 3.1: Test furnace schematic.

At the start of the test, and at every cycle, each sample went through a set weighing and salt spraying procedure:

- The samples were cooled to room temperature (if necessary) and weighed.
- After heating to ≥100°C the samples were weighed for a second time.
- Whilst hot each sample was sprayed with the correct amount of test salt solution before being weighed again. Care was taken to ensure that the salt was applied evenly around the circumference of the cylindrical samples.
- The samples were allowed to cool back down to room temperature before being weighed for a final time.

All sample weights were measured on a calibrated balance with a resolution of ±10 μg. For the purpose of calculating the weight change data over a cycle, the cold sample weight measured immediately prior to the start of the cycle was compared with the cold sample weight immediately after that cycle had completed. This prevented any spalling incurred due to handling and salt spraying from affecting the results.

The above procedure has been used in a number of previous studies [5; 26; 34] and is referred to as the deposit recoat technique.

3.3 Post-exposure preparation

In preparation for microscopic examination, the samples were mounted in resin using a special jig shown in Figure 3.2. The samples were pushed against two vertical pins by blade on a spring loaded arm. This ensured that the samples had a vertical orientation, ensuring the cross-section of the samples was perpendicular to the cylindrical axis of the sample and thus minimising metrological errors in the analytical stage. Additionally, the blade provided a reference point on the circular cross section.

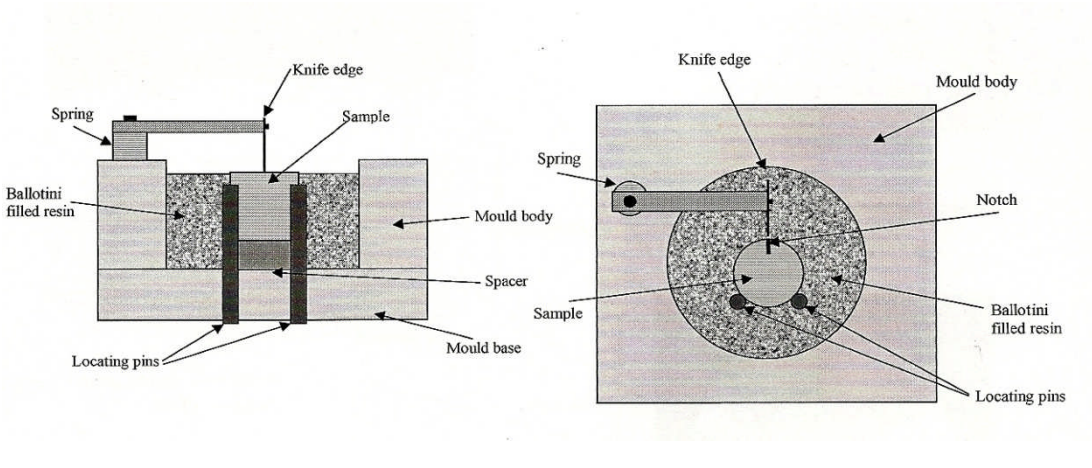

Figure 3.2: Sample mounting jig [36].

The samples were completely encased in an even mixture of epoxy resin and ballotini (0.04-0.07 mm silica glass beads), which reduced the resin shrinkage whilst it set. To ensure a good interface between the resin and sample, the prepared jig was subjected to a vacuum thus removing any trapped pockets of air in the resin mixture.

A precision saw was used to cross-section the samples at their approximate midpoint before a semi-automated grinding and polishing machine was used to prepare the surface to a 1 µm finish. During these procedures, oil was used as a lubricant instead of water (which is usually used during metallographic sample preparation) to prevent water soluble species that may be present on the sample from dissolving.

3.4 Sample analysis

An accurate method for measuring the degree of damage suffered during the corrosion process is required to draw reliable conclusions [34]. To achieve this, a reflected light microscope with a calibrated X, Y stage was used to measure the coordinates of the remaining metal and any internal damage on sample cross-sections after exposure. The analysis software achieves this by taking a series of photograph images around the circumference of the sample and then combining these into a mosaic depicting the sample surface outline. For each of these combined mosaics, a line is drawn from the centre of the sample bisecting the circumference of the remaining metal. This position is marked and the coordinates stored, along with the position of any internal damage along this line. To obtain a statistically significant number of measurements, 30 mosaics were obtained equally spaced out around the circumference of the sample [24]. The data attained by this technique was inputted into a spreadsheet that can re plot the sample outline and compare it with the original dimensions of the sample to determine the amount of metal lost at each point that was measured. This is shown graphically in Figure 3.3.

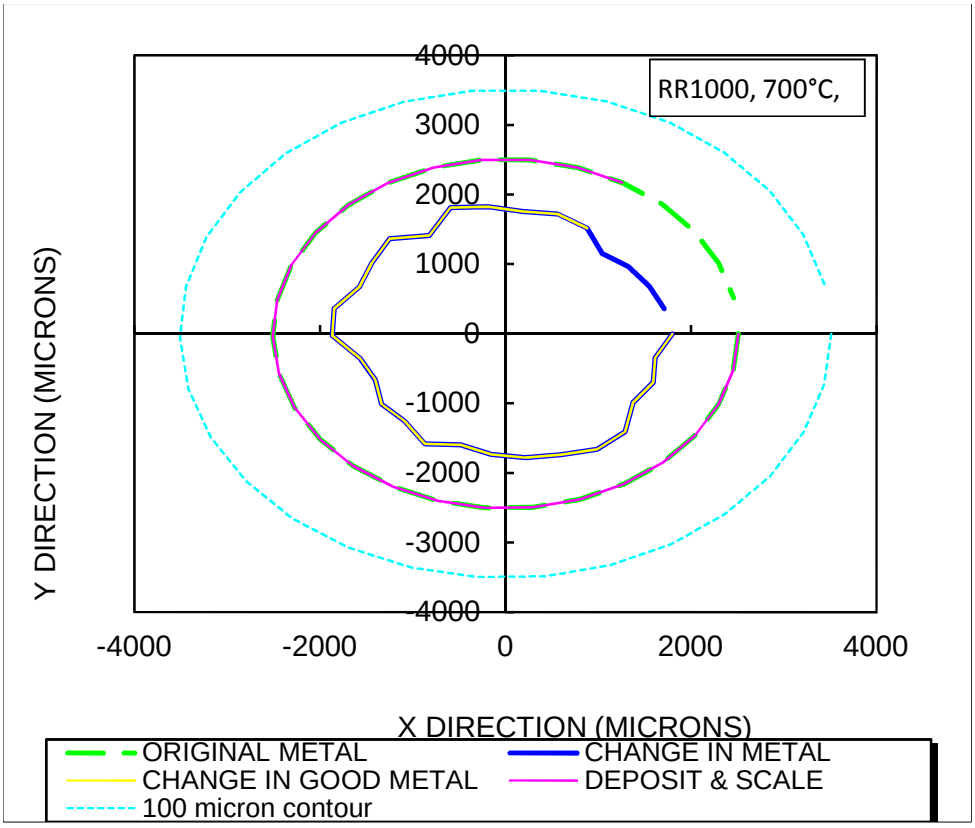

Figure 3.3: Polar plot of the combined data set showing the magnified difference between the original and post exposure sample dimensions.

The metal loss data is then ranked in order of severity and graphically presented as a function of cumulative probability derived from the following equation [24]:

$$cumulative\ probability\ (\%) = \frac{n}{N+1} \times 100$$

Where *n* is the rank number and *N* is the total number of points.

An example of such a graphical plot is shown in Figure 3.4 (assuming a normal distribution of data). The gradient of each data series is proportional to the standard deviation and gives an indication of how uniform the surface (and corrosion distribution) of that sample is; a steeper gradient corresponds to a more uneven surface. Data points with a low probability but with a large amount of metal loss compared to the rest of the sample describe pitting features that may form during exposure. Such features are important because they are susceptible to further rapid corrosion and are likely initiation points for the formation of cracks caused by stresses. Thus a component susceptible to pitting may fail even if the total amount of metal lost is relatively small.

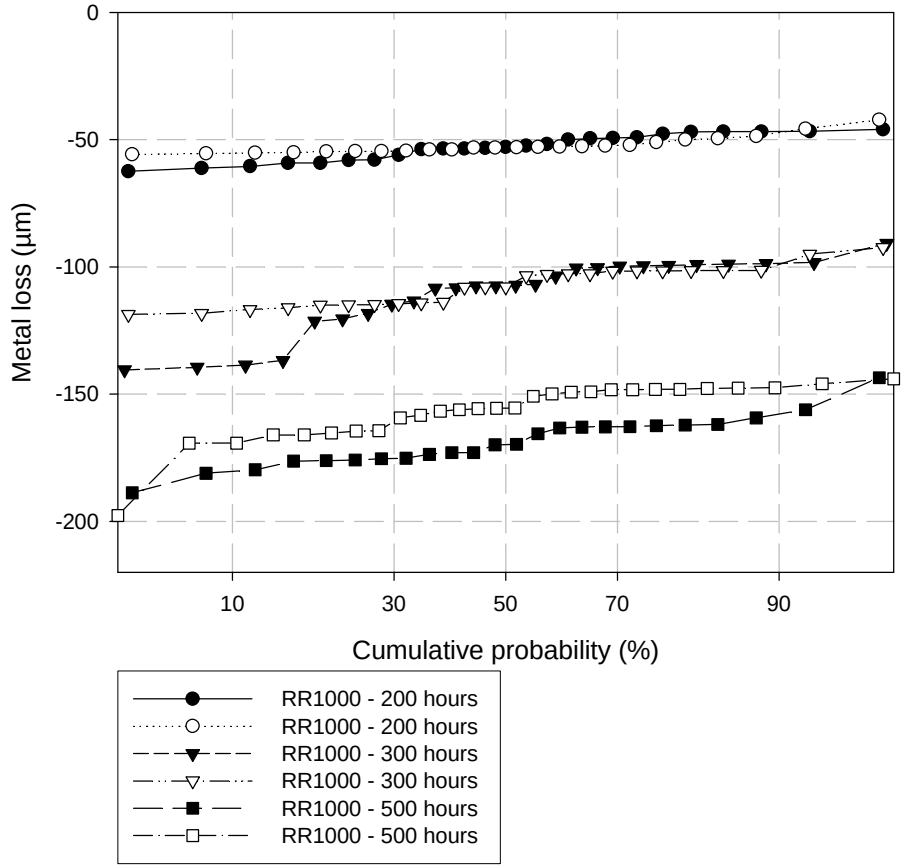

Figure 3.4: Example of a normal cumulative probability of metal loss exceedance plot.

A second analytical method used a reflected light microscope to take optical pictures of the surface of each sample. As well as showing the general condition of the sample surface, any interesting corrosion features were identified and photographed with this technique. Because the degree of corrosion product that spalls is often variable, the amount of corrosion product visible does not give any reliable information. Although this technique provides limited information for these types of corrosion test, it is both quick and simple and can identify features that can be later investigated by more thorough methods.

The third method of analysis was the use of an ESEM (environmental scanning electron microscope) equipped with an energy dispersive X-ray (EDX) to investigate the sample surface under much greater resolution. In addition, the EDX analysis feature was used to determine the elemental composition of samples at various distances into the metal or its deposit/scale.

To take images of the sample cross-section at magnifications that exceed the capability of optical microscopes, the ESEM was set up to detect backscattered electrons. In a backscattered imaging mode, brightness is proportional to the average atomic number of the material being hit by the electron beam. Therefore this type of detection allows a good contrast between areas of different elemental composition as is found at the surface of a corroded sample, Figure 3.5 is an example of this kind of image showing a pitting feature at 1000 times magnification. Oxides generally show up as darker than metals using this imaging technique but precipitates of other phases can sometimes be seen in metals, deposits and scales if their average atomic number is sufficiently different.

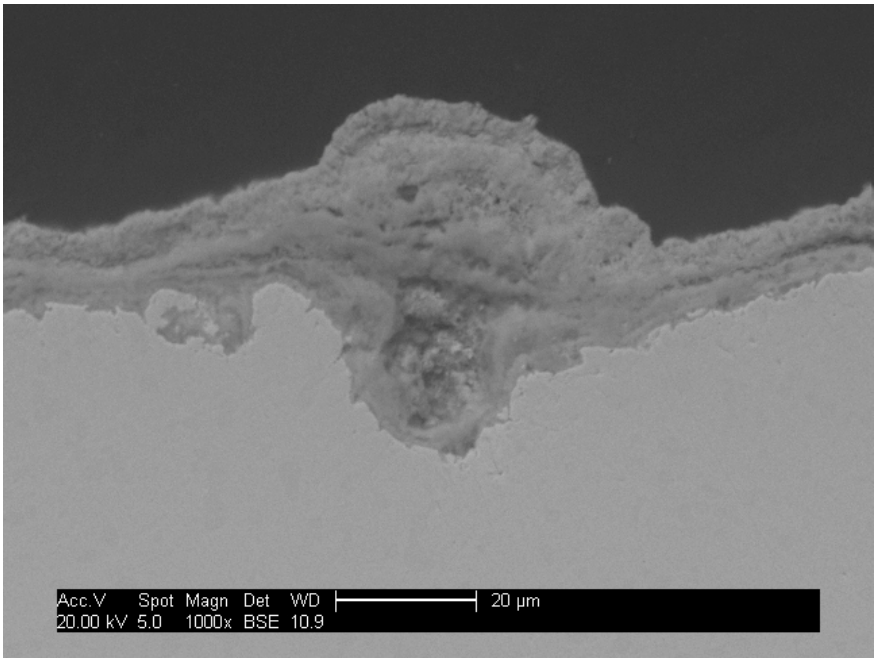

Figure 3.5: ESEM image showing the formation of a pitting feature.

The EDX feature of the ESEM is able to identify and quantify the elements present at any given point or area on the sample. This is achieved by detecting the characteristic X-ray photons that are created when high energy electrons are focused onto the sample surface.

To determine the best method for using the EDX function, three different approaches were tried. The first method was to use a mapping function to show the concentration of selected elements over an area of the sample surface with a depth of approximately 250 µm into the sample. Figure 3.6 shows an elemental map of a cross section through the surface of a RR1000 sample exposed for 500 hours in test 1. Although these images give a good indication of where the selected elements are concentrated, it does not give accurate statistical information which would be useful to provide comparisons with other samples in the test program.

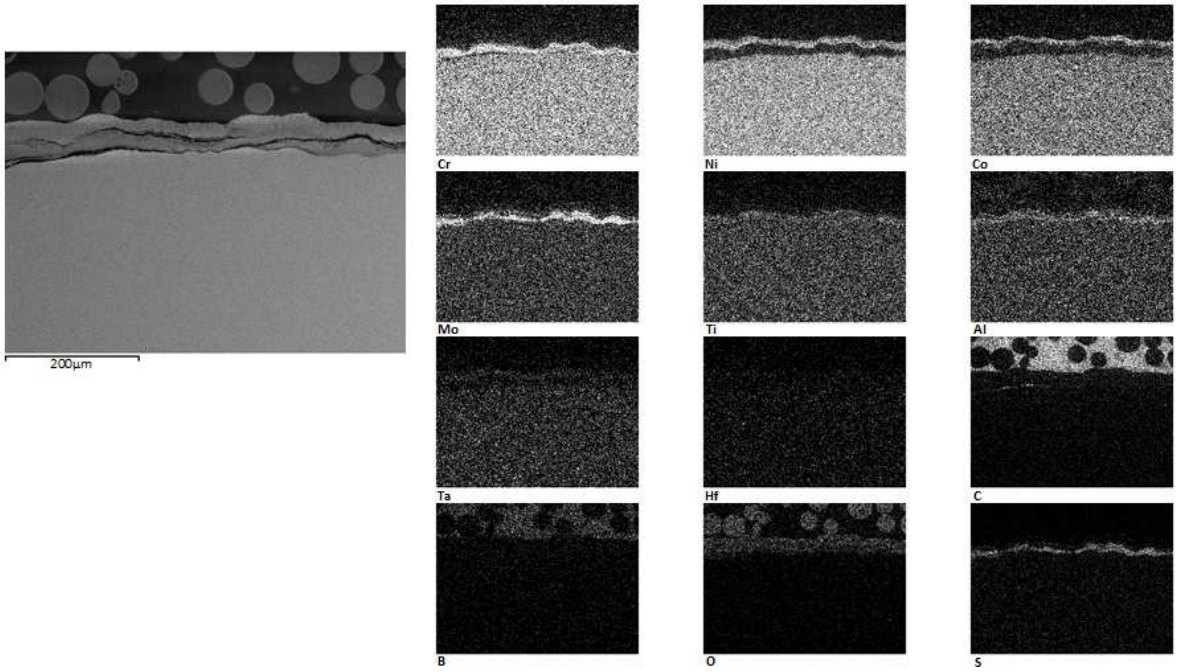

Figure 3.6: Example of an EDX element map of an exposed RR1000 sample

For a more quantifiable investigation of how the elements present after exposure are distributed, a series of areas at specific points were analysed. To achieve this, strips of the sample measuring approximately 10 µm in width and over 250 µm in length were scanned in intervals of 50 µm in depth from the sample surface. This scanning pattern is shown in Figure 3.7 and provides information on how the corrosion process changes the elemental composition of the alloy and to what depth into the remaining metal it has an effect. This method of analysis assumes that the relevant change in elemental composition occurs perpendicular to the sample surface and not laterally. For this reason, the site on the sample surface chosen for investigation has no features penetrating into the sample surface such as a pit.

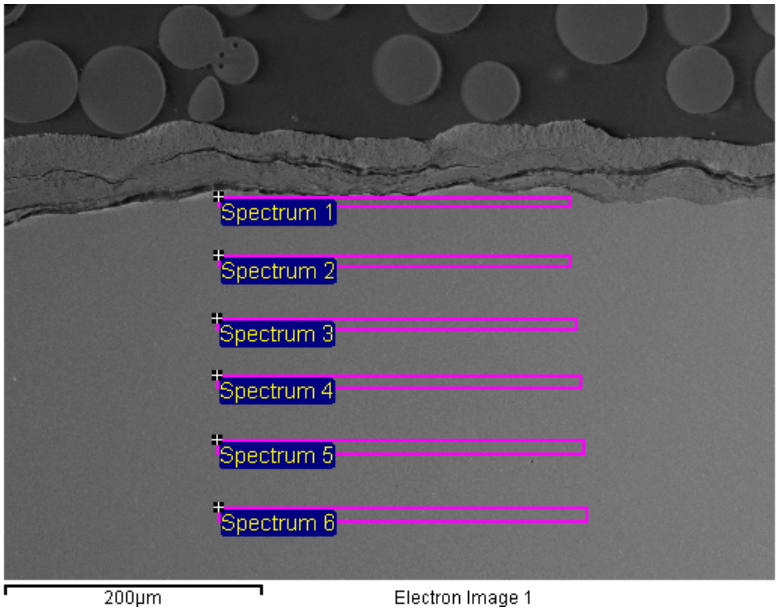

Figure 3.7: Scanning pattern for analysing alloy composition change internally to the sample.

4. Results

In this chapter, the results for all the corrosion tests are presented. Four types of diagnostic method been used to give a thorough sample analysis;

- Mass change data: this provides an approximate assessment of the sample corrosion rate using cumulative mass change data obtained periodically throughout the sample exposure.
- Dimensional metal loss: this information is a more quantitative assessment of the corrosion damage suffered by each sample over the duration of the test.
- Optical Microscopy: the images produced by optical microscopy allow for a visual assessment and comparison of the changes in surface morphology between each sample cross-section.
- Scanning electron microscopy (SEM) and energy dispersive X-ray analysis (EDX): this form of microscopy can more accurately investigate surface features previously identified using optical microscopy. In addition, the EDX function can be used to give a chemical assessment of the corrosion process.

Due to time and resource constraints, not every sample could be analysed optically or by using the SEM. This form of analysis is reserved for samples that make a particular contribution to the study.

4.1 Test 1

The parameters for test one were selected to produce a type and degree of corrosion that could be found on the turbine disc of a jet engine (these conditions are now believed to be too aggressive). These parameters were used as a standard in this study, from which the various variables can be altered and investigated. To ensure accuracy, pairs of each alloy were exposed; a summary of the test conditions is listed below:

- Temperature: 700°C
- Materials: Waspaloy, U720 and RR1000
- Exposure times: 200, 300 and 500 hours
- Deposit composition: 2% NaCl 98% Na_2SO_4 (molar %)
- Deposit flux: 10 µg/cm²/h
- Atmosphere: 300ppm SO_2 in air

4.1.1 Cumulative net weight change data

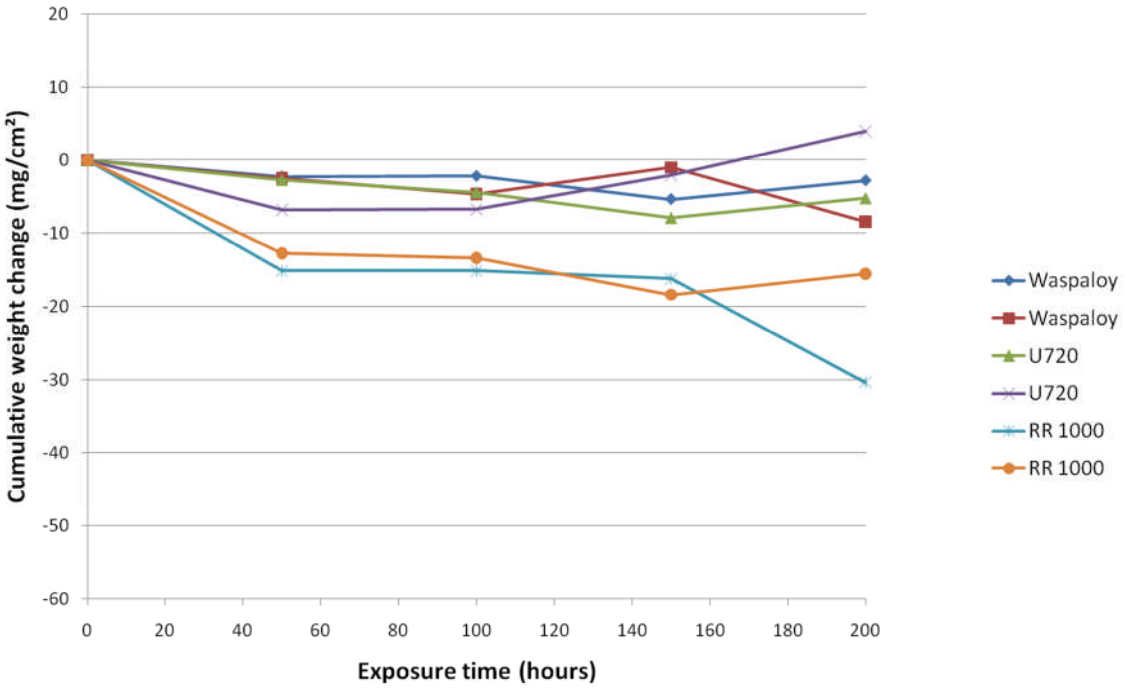

Figure 4.1: Test 1, 200 hour weight change data. 700°C, using 10 µg/cm²/h of a 2% NaCl 98% Na_2SO_4 deposit.

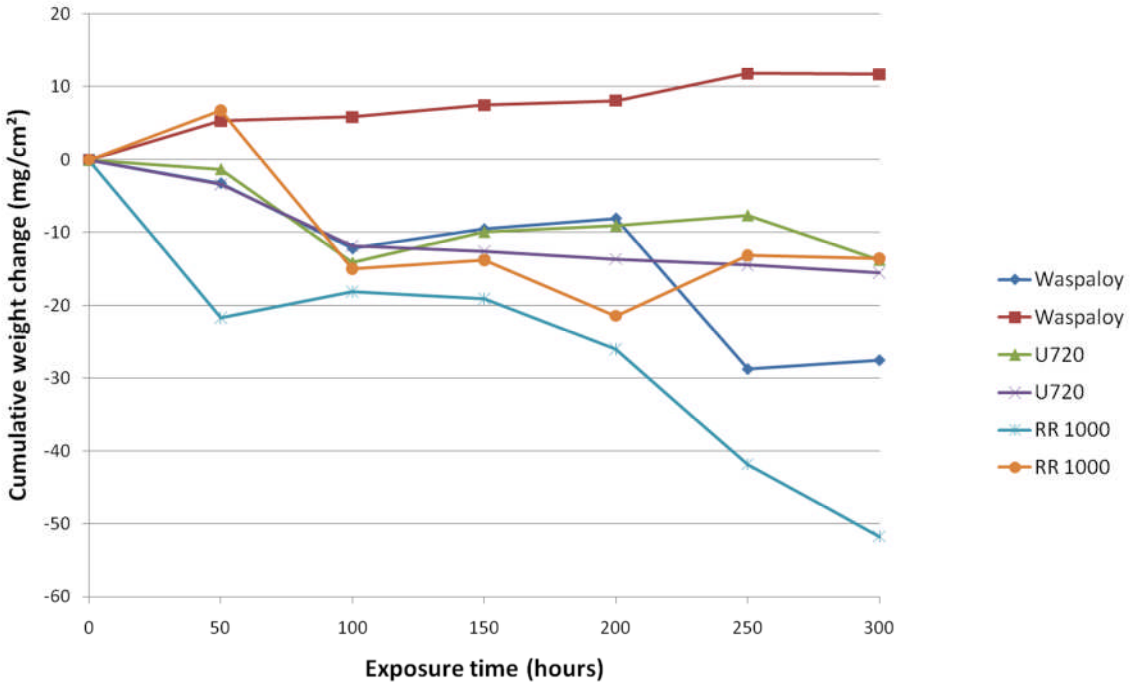

Figure 4.2: Test 1, 300 hour weight change data. 700°C, using 10 µg/cm²/h of a 2% NaCl 98% Na_2SO_4 deposit.

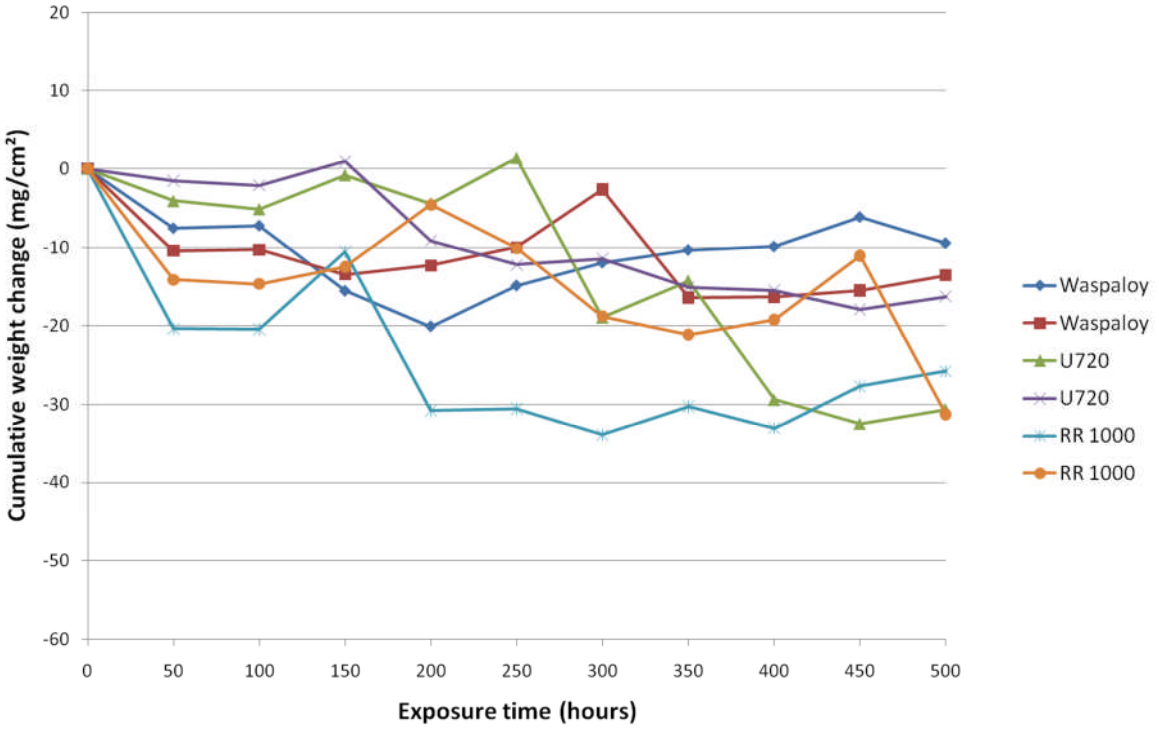

Figure 4.3: Test 1, 500 hour weight change data. 700°C, using 10 µg/cm²/h of a 2% NaCl 98% Na_2SO_4 deposit.

Figures 4.1, 4.2 and 4.3 show that there is considerable variance in the weight change data when comparing samples of the same material. However, despite this variance, it can be observed that RR1000 generally suffers the greatest amount of weight change at each stage of the exposure. At 200 and 300 hours there is little difference in the performance of Waspaloy and U720. However, over the 500 hour time period, U720 shows a greater degree of weight change.

4.1.2 Dimensional metal loss data

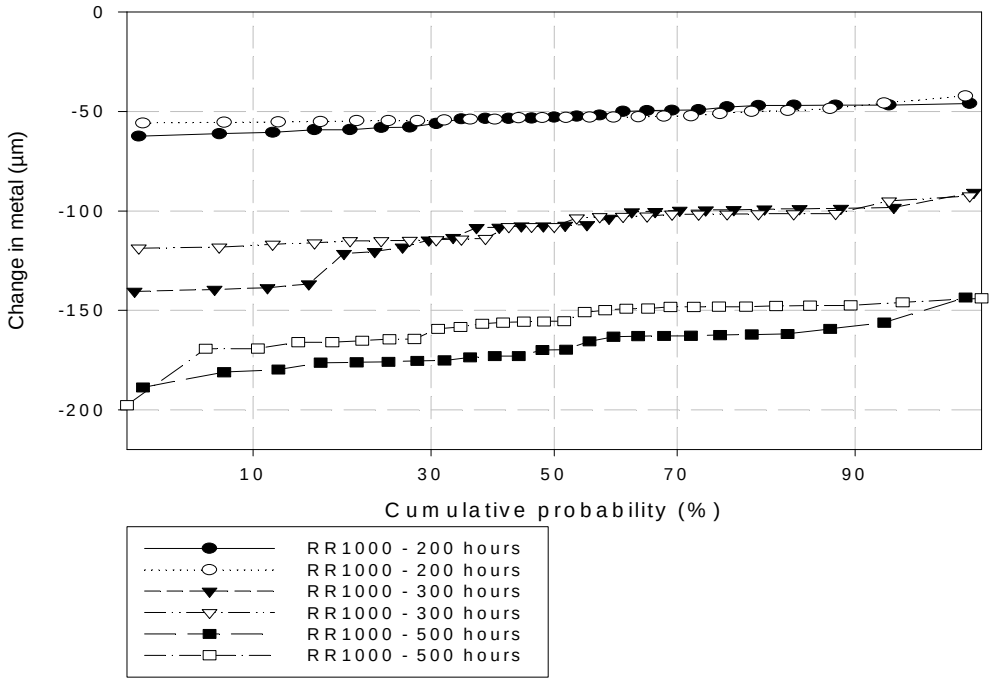

Figure 4.4: Dimensional metal loss as a function of cumulative probability for RR 1000 samples using 10 µg/cm²/h of a 2% NaCl 98% Na_2SO_4 deposit.

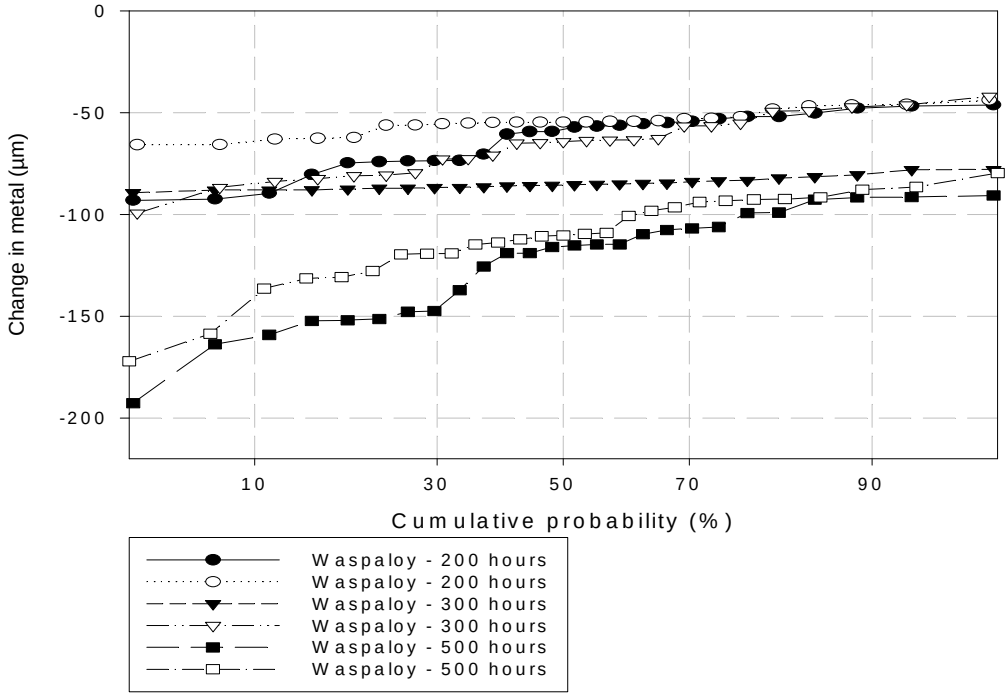

Figure 4.5: Dimensional metal loss as a function of cumulative probability for Waspaloy samples using 10 µg/cm²/h of a 2% NaCl 98% Na_2SO_4 deposit.

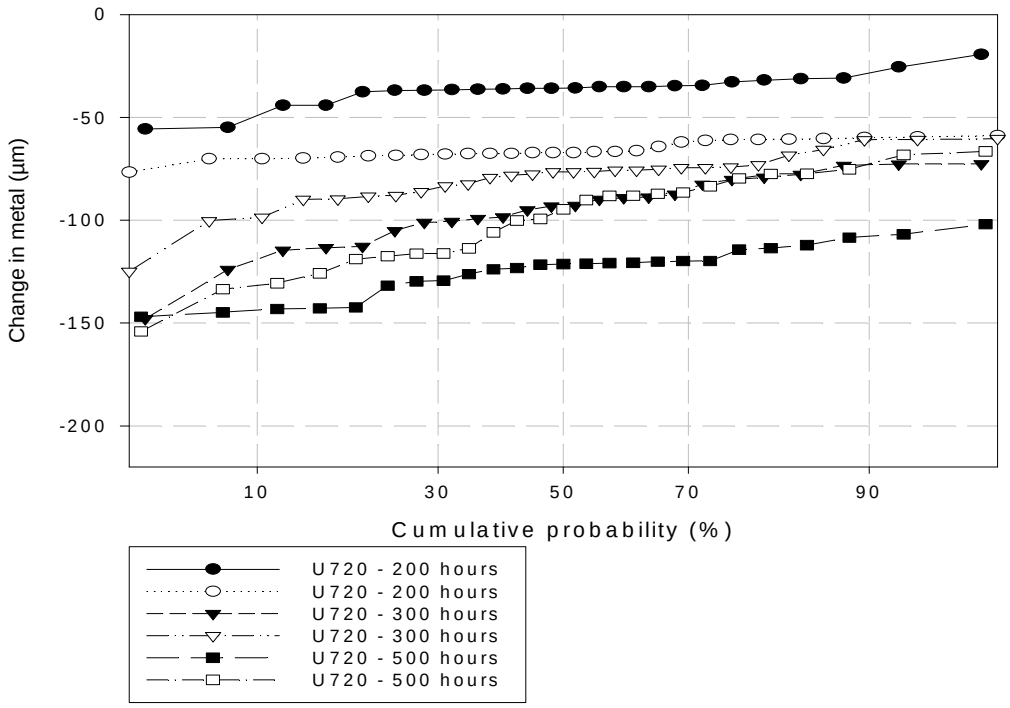

Figure 4.6: Dimensional metal loss as a function of cumulative probability for U720 samples using 10 µg/cm²/h of a 2% NaCl 98% Na_2SO_4 deposit.

Figures 4.4, 4.5 and 4.6 confirm the trend indicated by the weight change data; that in terms of median metal loss, RR1000 exhibits a greater change in metal than the other two alloys. For example, after 500 hours exposure, the average median metal loss for RR1000 is 163 µm compared to 108 µm for U720 and 113 for Waspaloy.

The gradient of data series plots show how evenly distributed the corrosion damage on the surface of the sample is. A steep gradient indicates an uneven distribution of damage over the surface of the sample. The gradients of Figure 4.5 data plots are steeper after a 500 hour exposure than exposures of 200 and 300 hours showing that Waspaloy shows more areas of localised attack after 500 hours of exposure.

It can be observed that metal loss data in Figure 4.4 (for RR1000) are comparatively repeatable for the different exposure times. The data plots of Figures 4.5 and 4.6 (for Waspaloy and U720) are more variable at the different exposure times.

4.2 Test 2

Test 2 investigates the effects of varying the deposit composition and flux. The other test parameters were kept the same as test 1 to allow comparisons to be made. The full test conditions are as follows:

- Temperature: 700°C
- Materials: Waspaloy, U720 and RR1000
- Exposure times: 200, 300 and 500 hours
- Deposit composition: 2% NaCl 98% Na_2SO_4 and 5% NaCl 95% Na_2SO_4 (molar %)
- Deposit flux: 2 µg/cm²/h and 10 µg/cm²/h
- Atmosphere: 300ppm SO_2 in air

4.2.1 Cumulative net weight change data

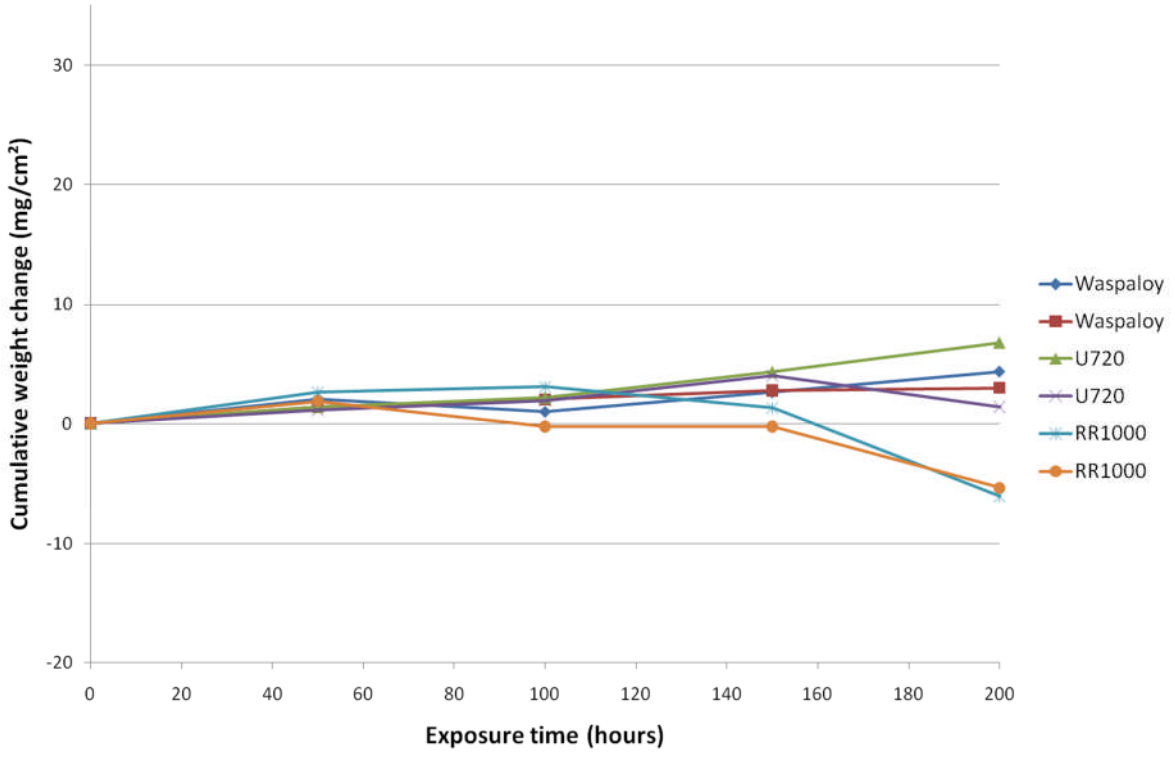

Figure 4.7: Test 2, 200 hour weight change data for samples with a 2 µg/cm²/h, 2% NaCl 98% Na_2SO_4 deposit at 700°C with 300ppm SO_2 in air.

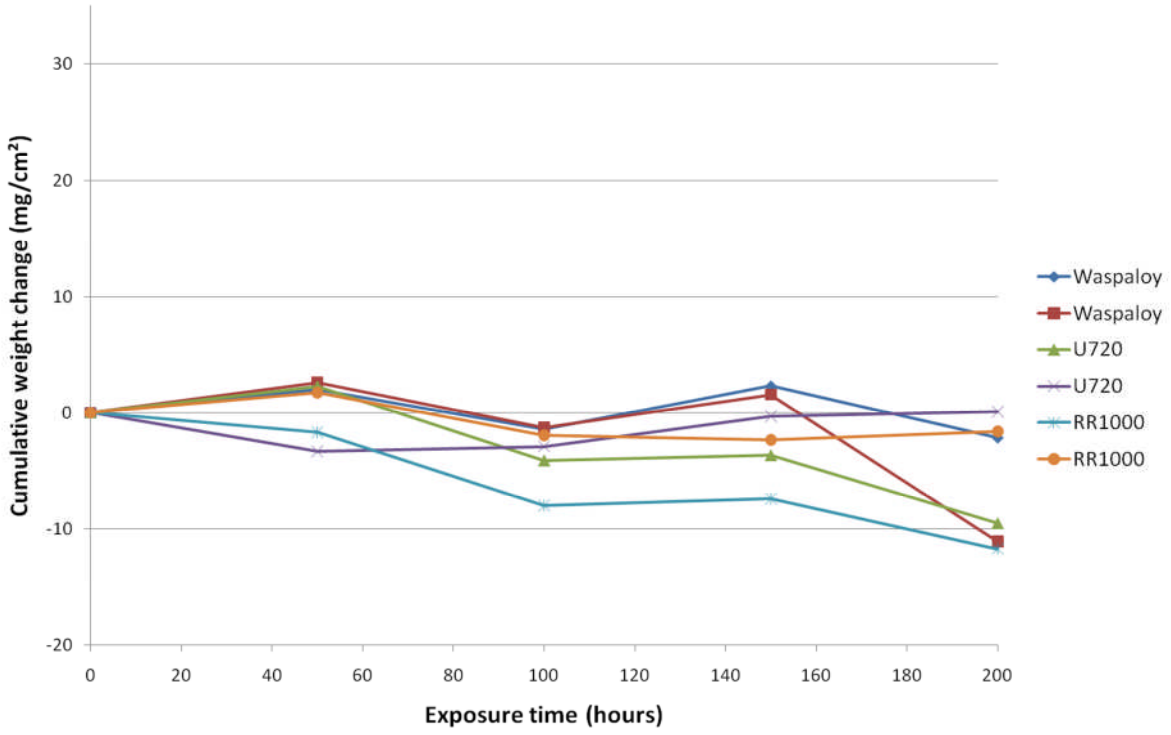

Figure 4.8: Test 2, 200 hour weight change data for samples with a 10 µg/cm²/h, 5% NaCl 95% Na_2SO_4 deposit at 700°C with 300ppm SO_2 in air.

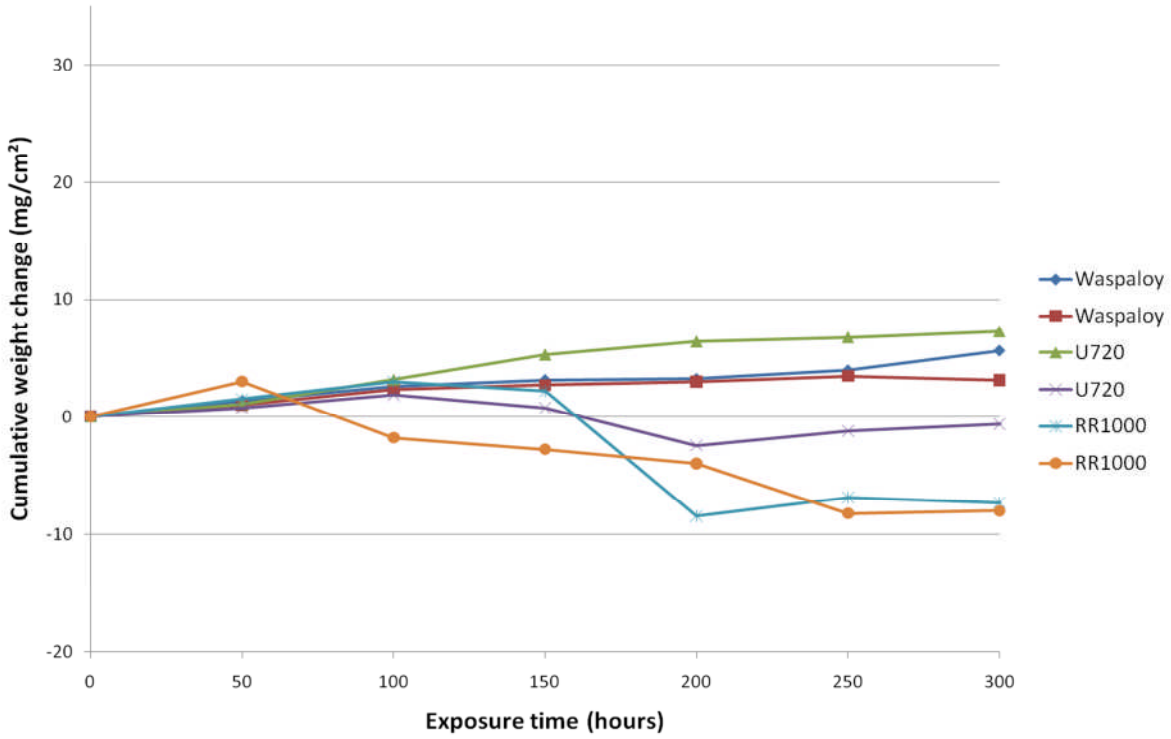

Figure 4.9: Test 2, 300 hour weight change data for samples with a 2 µg/cm²/h, 2% NaCl 98% Na_2SO_4 deposit at 700°C with 300ppm SO_2 in air.

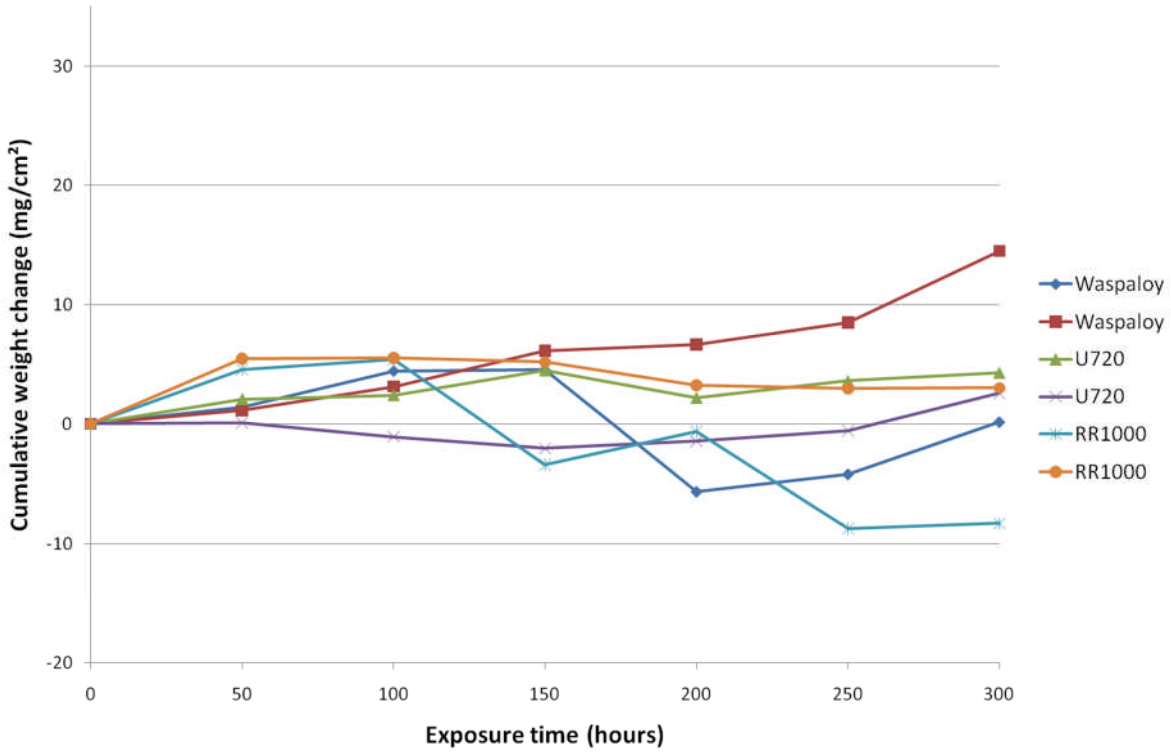

Figure 4.10: Test 2, 300 hour weight change data for samples with a 10 µg/cm²/h, 5% NaCl 95% Na_2SO_4 deposit at 700°C with 300ppm SO_2 in air.

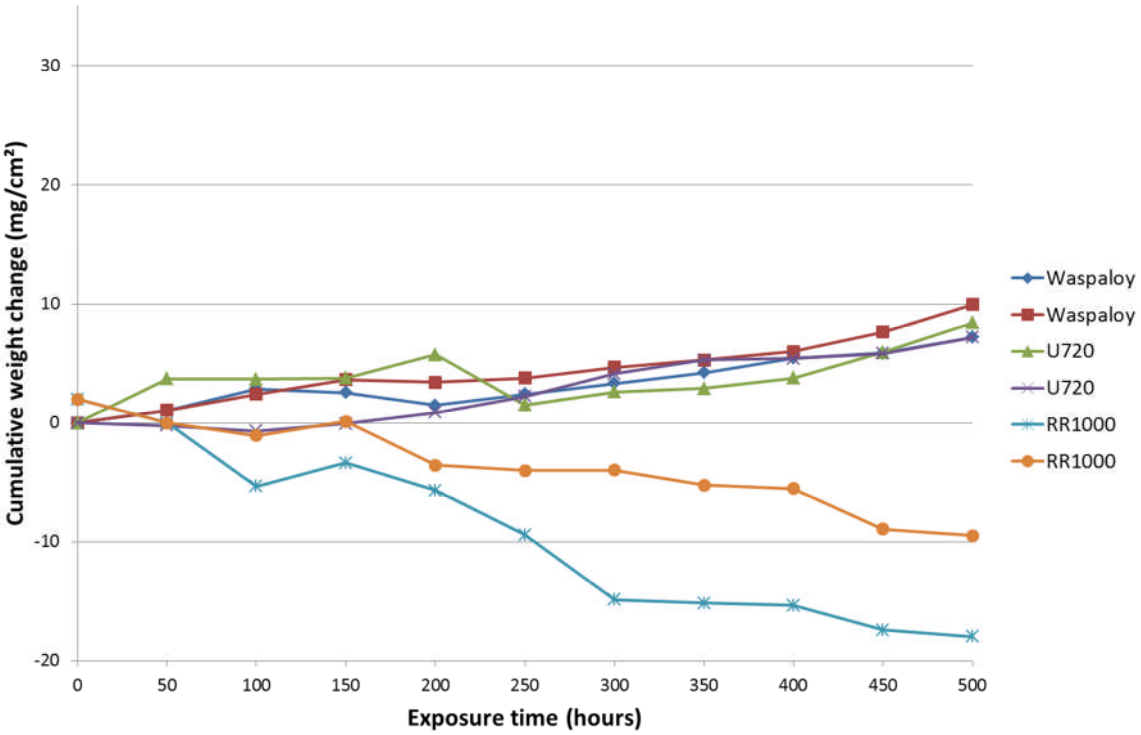

Figure 4.11: Test 2, 500 hour weight change data for samples with a 2 µg/cm²/h, 2% NaCl 98% Na_2SO_4 deposit at 700°C with 300ppm SO_2 in air.

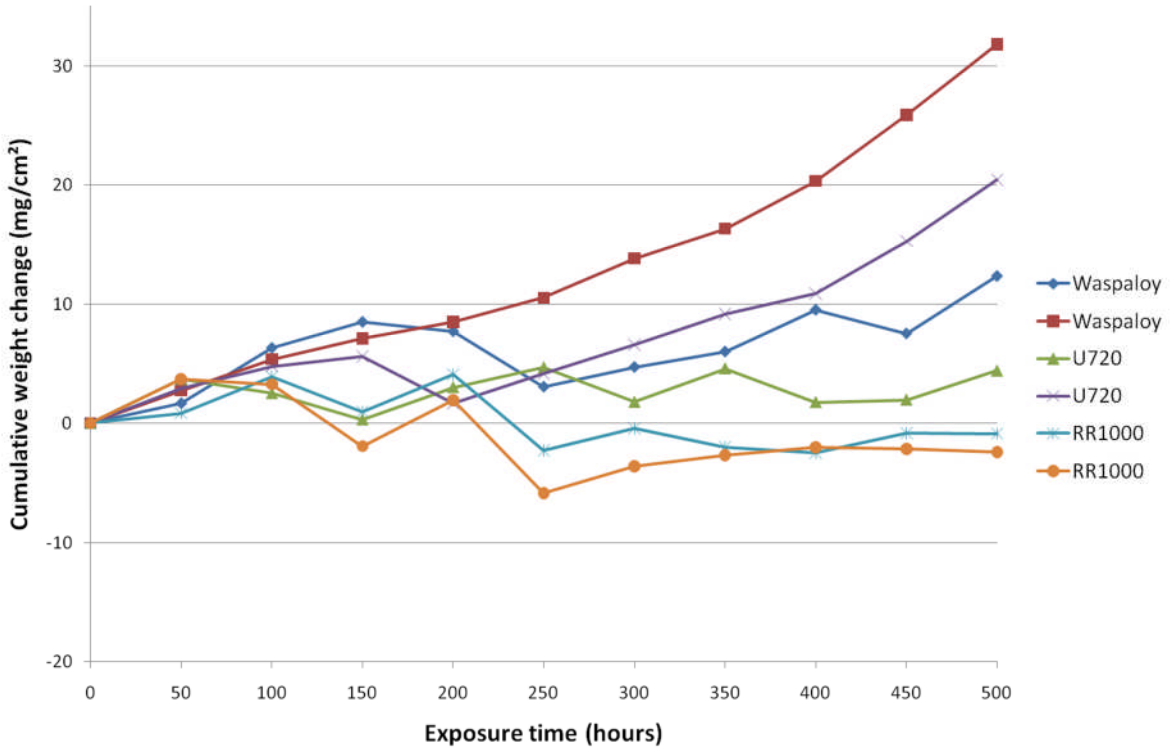

Figure 4.12: Test 2, 500 hour weight change data for samples with a 10 µg/cm²/h, 5% NaCl 95% Na_2SO_4 deposit at 700°C with 300ppm SO_2 in air.

For both deposit parameters used in test 2 (2 µg/cm²/h of a 2% NaCl 98% Na_2SO_4 deposit and 10 µg/cm²/h of a 2% NaCl 98% Na_2SO_4 deposit), the magnitude of the cumulative weight change is less than those of test 1 (2 µg/cm²/h of a 2% NaCl 98% Na_2SO_4 deposit) over the same exposure period. As with the test 1 data, there is considerable variability between duplicate samples although RR1000 generally shows a greater negative cumulative weight change value. Because of the variance in the data, it is difficult to make comparisons between the two deposit parameters. However, Figures 4.8, 4.10 and 4.12 for samples sprayed with 10 µg/cm^2/h of 5% NaCl 95% Na_2SO_4, tend to have a more positive cumulative weight change value than Figures 4.7, 4.9 and 4.11 sprayed with 2 µg/cm^2/h of 2% NaCl 98% Na_2SO_4.

4.2.2 Dimensional metal loss data

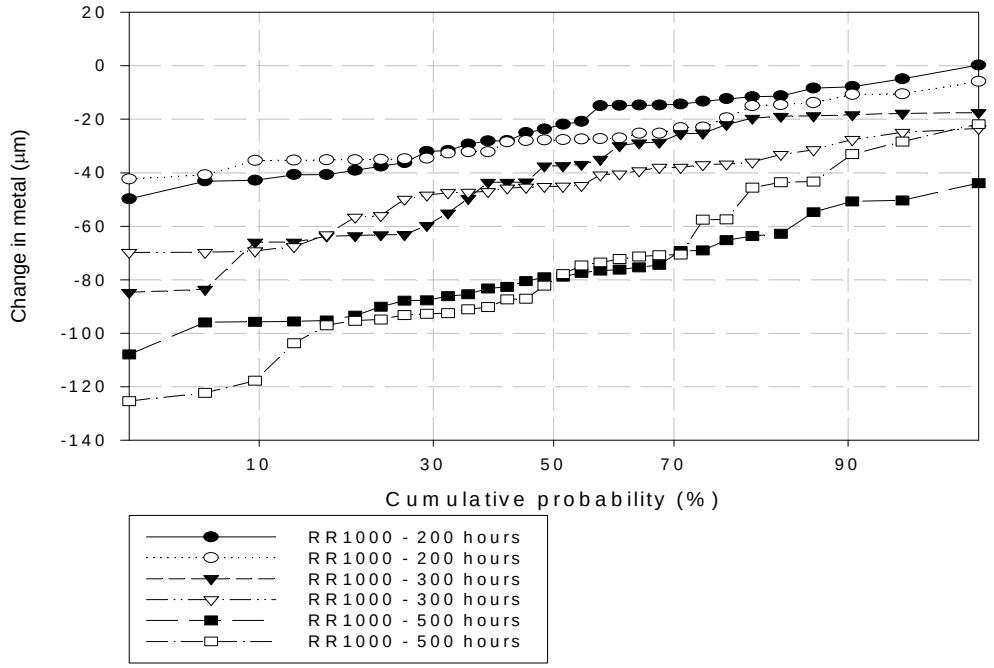

Figure 4.13: Cumulative normal probability plot for RR1000 samples sprayed with a 2 µg/cm²/h, 2% NaCl 98% Na_2SO_4 deposit.

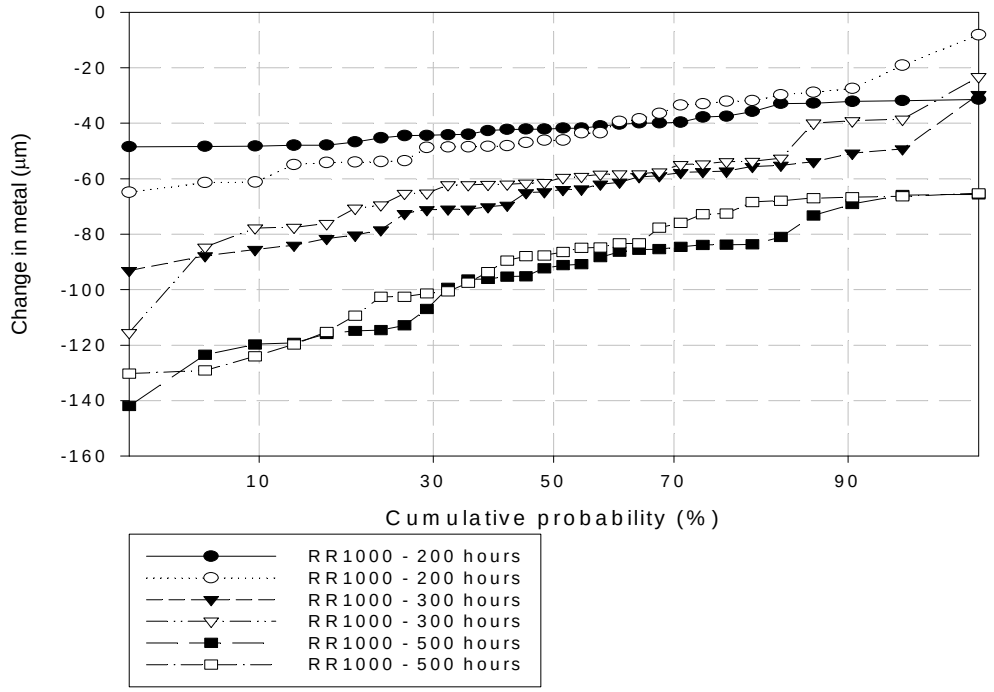

Figure 4.14: Cumulative normal probability plot for RR1000 samples sprayed with a 10 µg/cm²/h, 5% NaCl 95% Na_2SO_4 deposit.

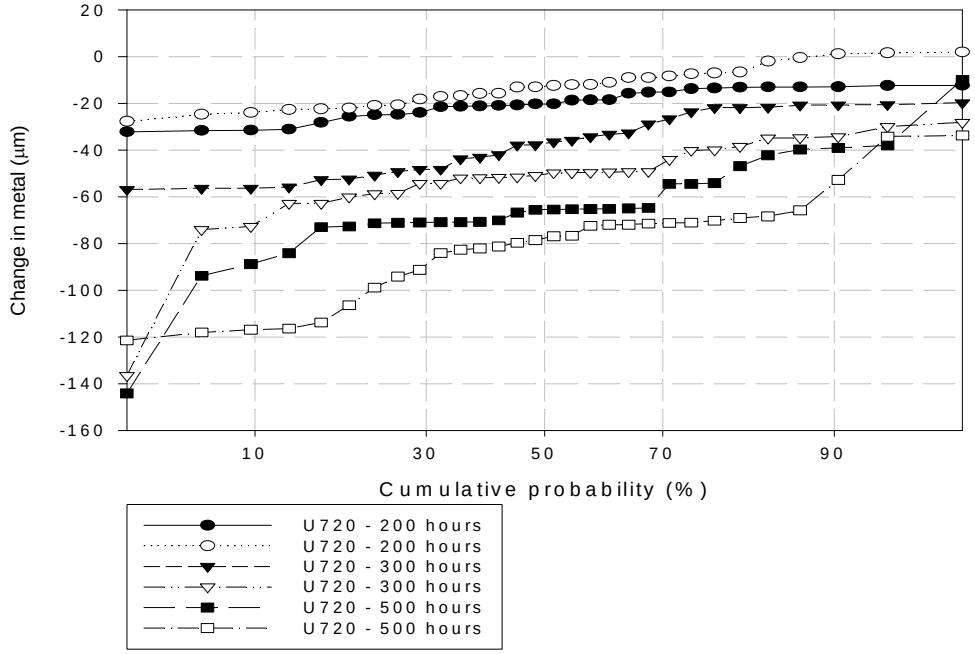

Figure 4.15: Cumulative normal probability plot for U720 samples sprayed with a 2 µg/cm²/h, 2% NaCl 98% Na_2SO_4 deposit.

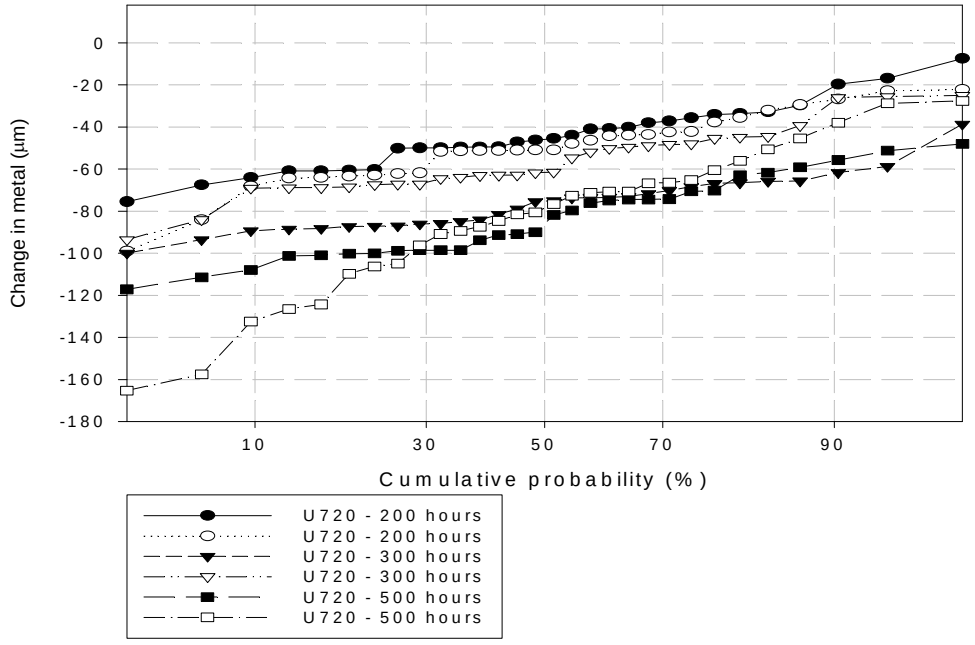

Figure 4.16: Cumulative normal probability plot for U720 samples sprayed with a 10 µg/cm²/h, 5% NaCl 95% Na_2SO_4 deposit.

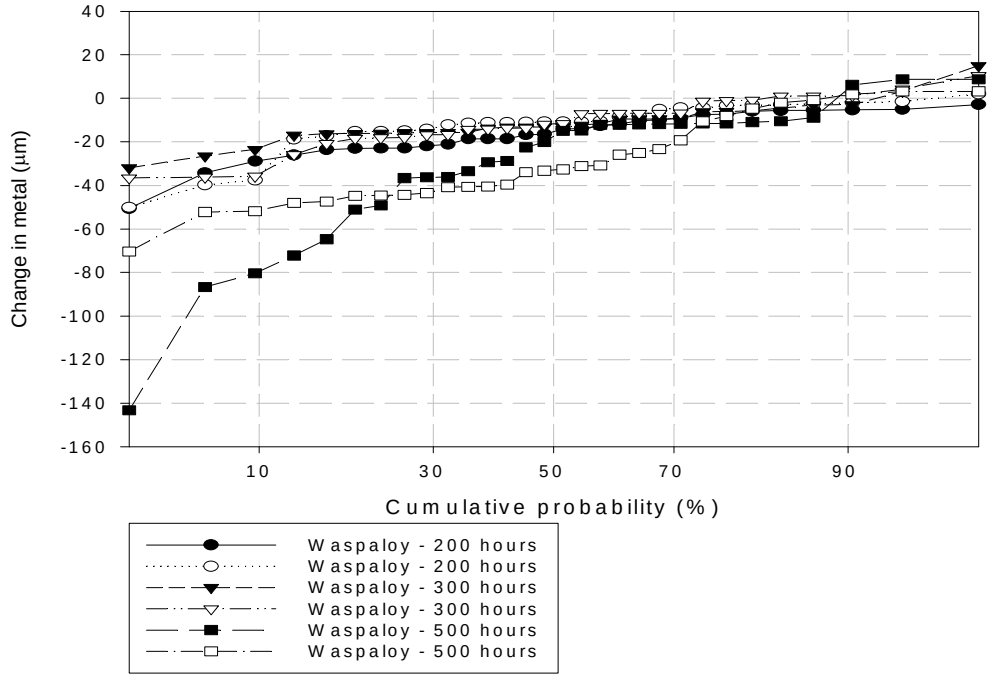

Figure 4.17: Cumulative normal probability plot for Waspaloy samples sprayed with a 2 µg/cm²/h, 2% NaCl 98% Na_2SO_4 deposit.

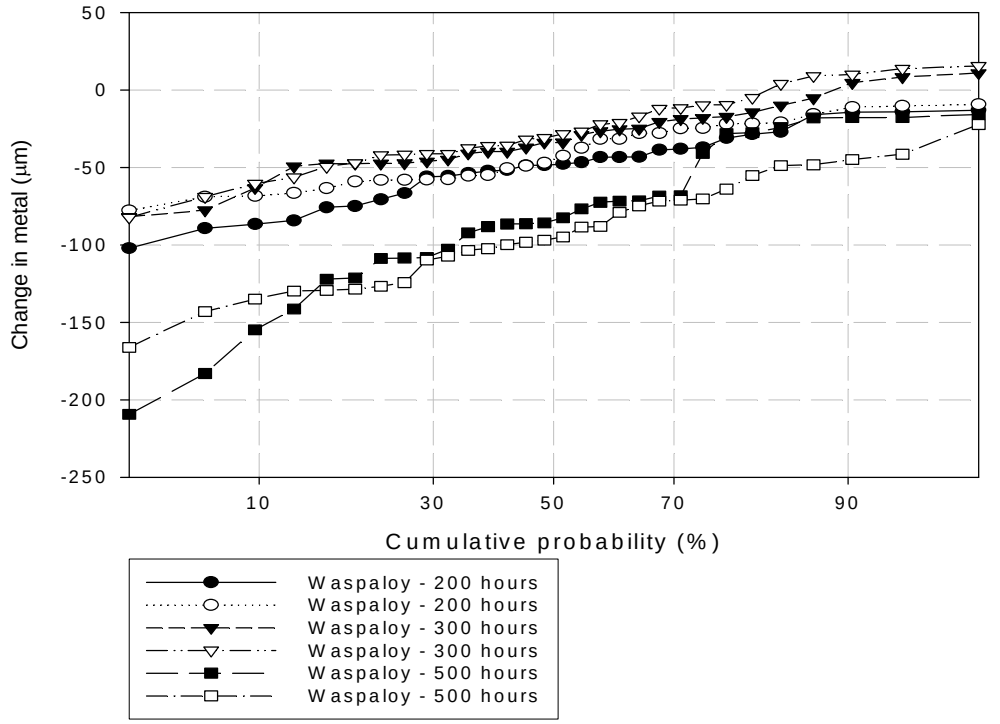

Figure 4.18: Cumulative normal probability plot for Waspaloy samples sprayed with a 10 µg/cm²/h, 5% NaCl 95% Na_2SO_4 deposit.

As with the cumulative probability of metal loss exceedance plots for test 1 (Figures 4.4 to 4.6), this type of measurement of corrosion is more repeatable and coherent than the equivalent cumulative mass change data. However, in accordance with the cumulative mass change data, samples sprayed with either of test 2 deposit fluxes (10 μg/cm²/h of 5% NaCl 95% Na_2SO_4 and 2 μg/cm²/h of 2% NaCl 98% Na_2SO_4), display less corrosion than the same samples in test 1 (10 μg/cm²/h of 2% NaCl 98% Na_2SO_4). Additionally, it can be seen that samples sprayed with a 2μg/cm²/h, 2% NaCl 98% Na_2SO_4 deposit (Figures 4.13, 4.15 And 4.17) suffer even less corrosion than those sprayed with a 10μg/cm²/h, 5% NaCl 95% Na_2SO_4 deposit (figures 4.14, 4.16 And 4.18).

Once again the change in metal loss over the 500 hour period is greater for RR1000 (Figures 4.13 and 4.14) compared to Waspaloy (Figures 4.17 and 4.17) with the distribution of damage more unevenly spread on Waspaloy.

4.3 Tests 3 and 4

These tests investigate the effect of shot peening of RR1000 samples prior to exposure. Test 3 was run under the same conditions as test 1, whereas the temperature was increased to 750°C for test 4. The following summarises the test parameters:

- Temperature: 700 and 750°C
- Materials: RR1000 (shot peened)
- Exposure times: 200 and 500 hours
- Deposit composition: 2% NaCl 98% Na_2SO_4 (molar %)
- Deposit flux: 10µg/cm²/h
- Atmosphere: 300ppm SO_2 in air

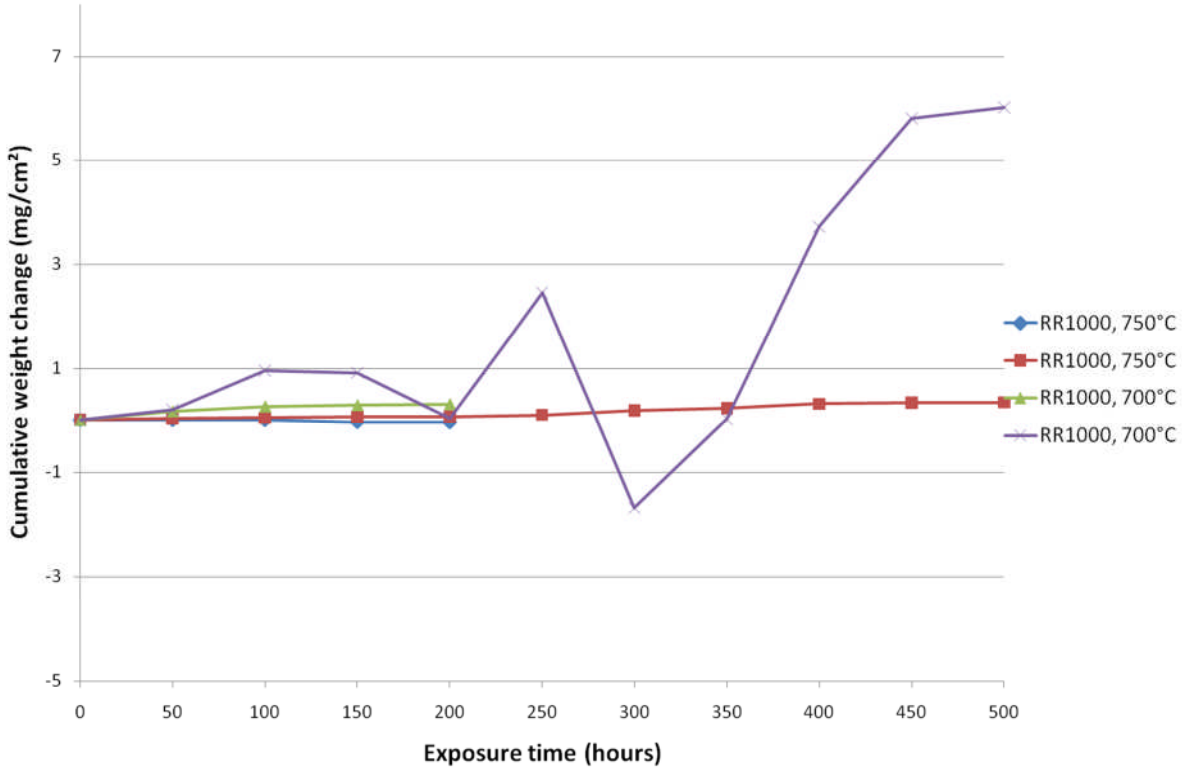

Figure 4.19: Tests 3 and 4 weight change data using 10 µg/cm²/h of a 2% NaCl 98% Na_2SO_4 deposit.

Figure 4.19 shows that RR1000 samples exposed at 750°C exhibit very little weight change and therefore appear to have suffered very little corrosion even after 500 hours of exposure. The sample exposed at 700°C for 200 hours also has undergone very little weight change; however the sample exposed for 500 hours shows a greater weight change, especially after 200 hours of exposure.

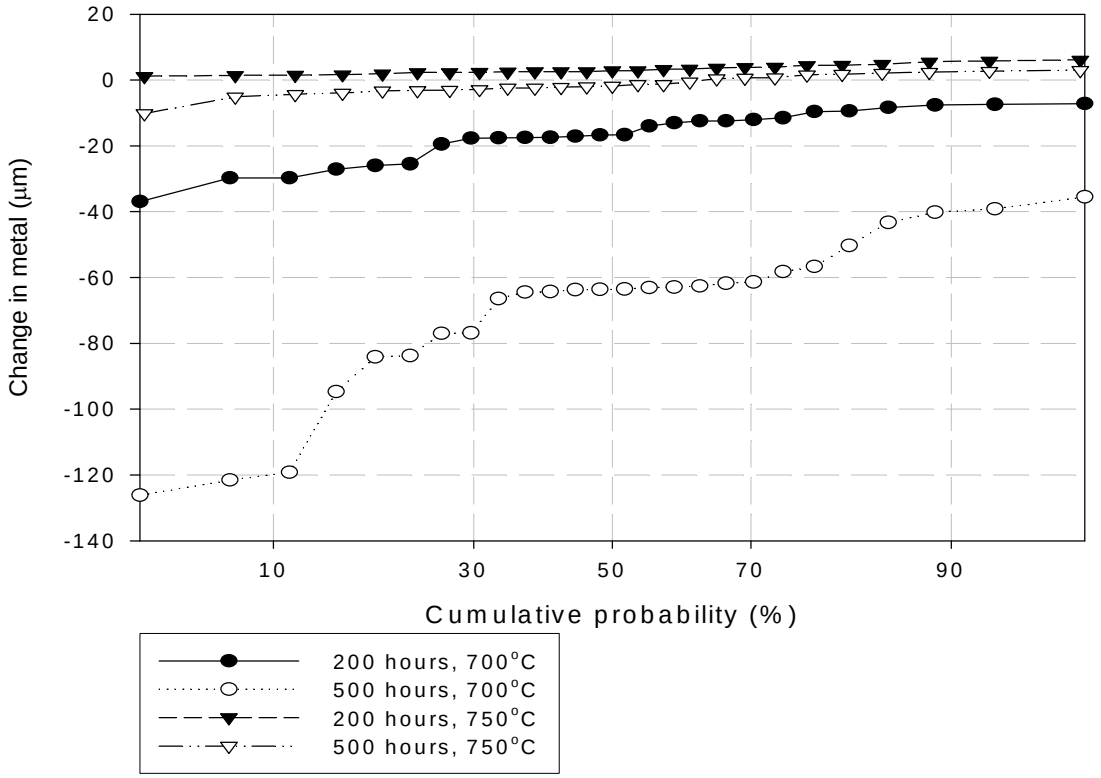

Figure 4.20: Cumulative normal probability plot for test 3 and 4 samples using 10 µg/cm²/h of a 2% NaCl 98% Na_2SO_4 deposit.

Figure 4.20 confirms that the RR1000 samples exposed at 750°C have suffered significantly less corrosion than those exposed at 700°C. Because the samples exposed at 700°C have been subjected to the same conditions as the RR1000 samples in test 1, these data can be used to investigate the effect of shot peening (section 5.5).

4.4 Test 5

The aim of this test was to determine the corrosion performance of certain disc alloys at 620°C. The exposure time was limited to a maximum of 200 hours to focus on the initial stage of corrosion and the transition into the second stage. The full test conditions are listed below.

- Temperature: 620°C
- Materials: IN718, Waspaloy, U720 and RR1000
- Exposure times: 100 and 200 hours
- Deposit composition: 2% NaCl 98% Na_2SO_4 (molar %)
- Deposit flux: 10 µg/cm²/h
- Atmosphere: 300ppm SO_2 in air

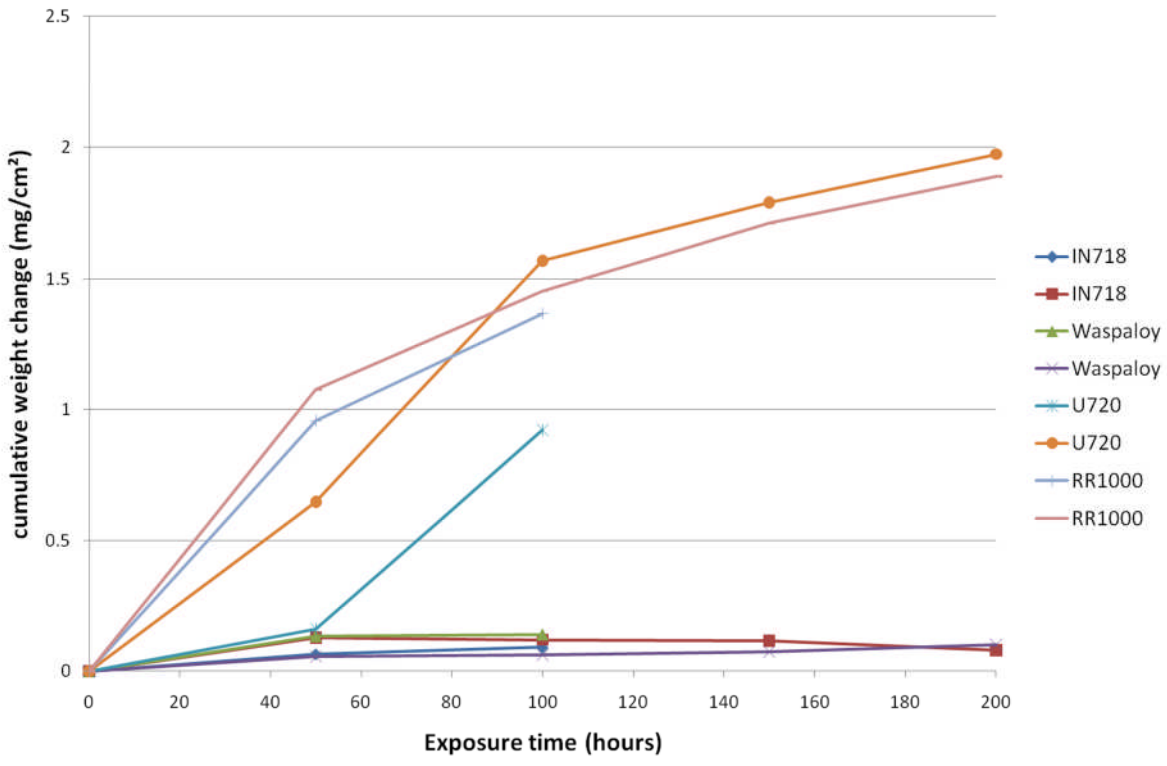

Figure 4.21: Test 5 weight change data using 10 µg/cm²/h of a 2% NaCl 98% Na_2SO_4 deposit.

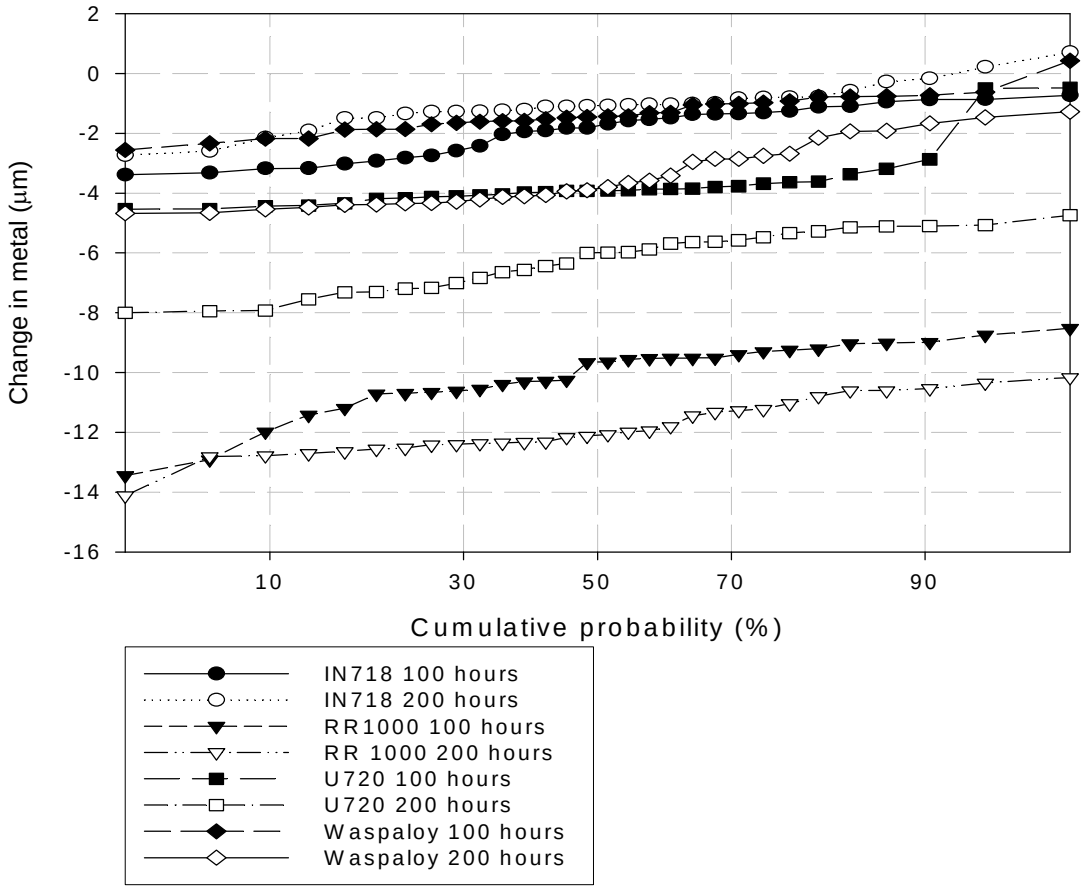

Figure 4.22: Cumulative normal probability plot for test 5 using 10 µg/cm²/h of a 2% NaCl 98% Na_2SO_4 deposit (change in metal scale from 2 to -16).

Figures 4.21 and 4.22 show that both IN718 and Waspaloy display similar corrosion behaviour at 620°C; suffering a relatively mild degree of attack with low metal losses. In accordance with the previous tests at 700°C, RR1000 has again undergone the greatest degree of corrosion whereas the result of U720 is roughly half way between RR1000 and Waspaloy.

4.5 Test 6

Similarly to test 5, this test investigates corrosion performances at a different temperature. This test was run in the same manner as the previous test but at a temperature of 650°C. The following is a summary of the test conditions:

- Temperature: 650°C
- Materials: IN718, Waspaloy, U720 and RR1000
- Exposure times: 100 and 200 hours
- Deposit composition: 2% NaCl 98% Na_2SO_4 (molar %)
- Deposit flux: 10 µg/cm²/h
- Atmosphere: 300ppm SO_2 in air

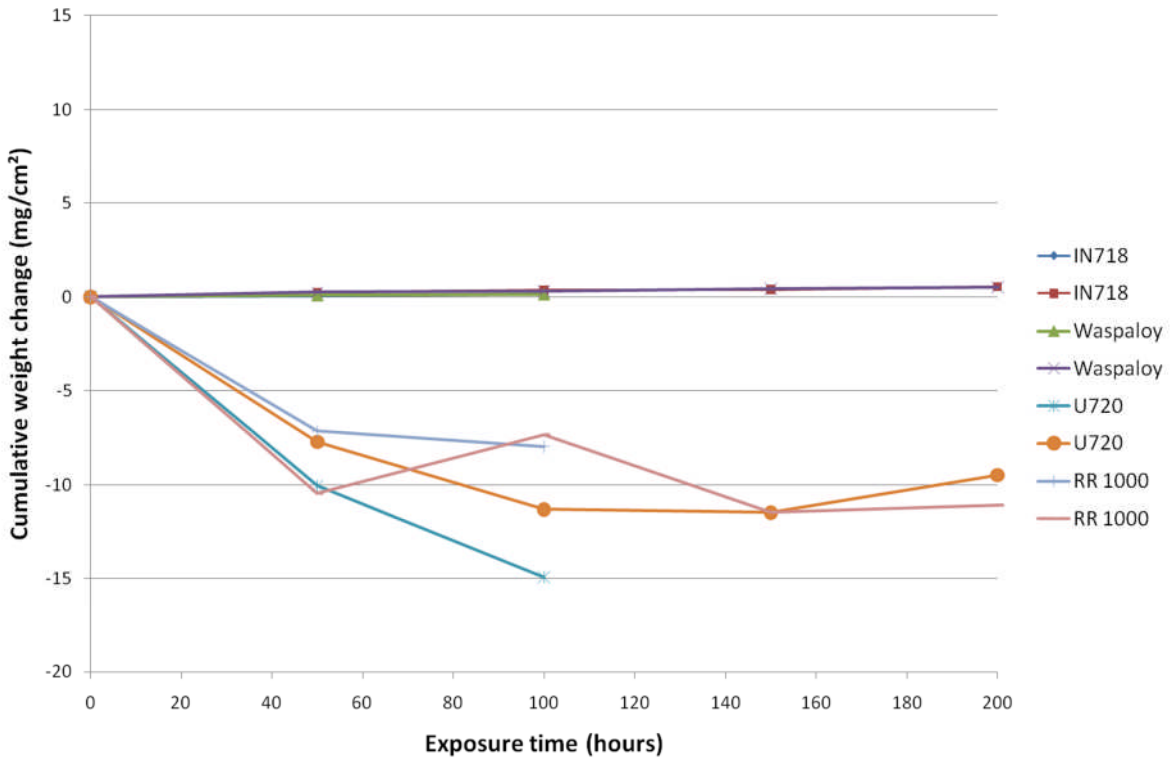

Figure 4.23: Test 6 weight change data using 10 µg/cm²/h of a 2% NaCl 98% Na_2SO_4 deposit.

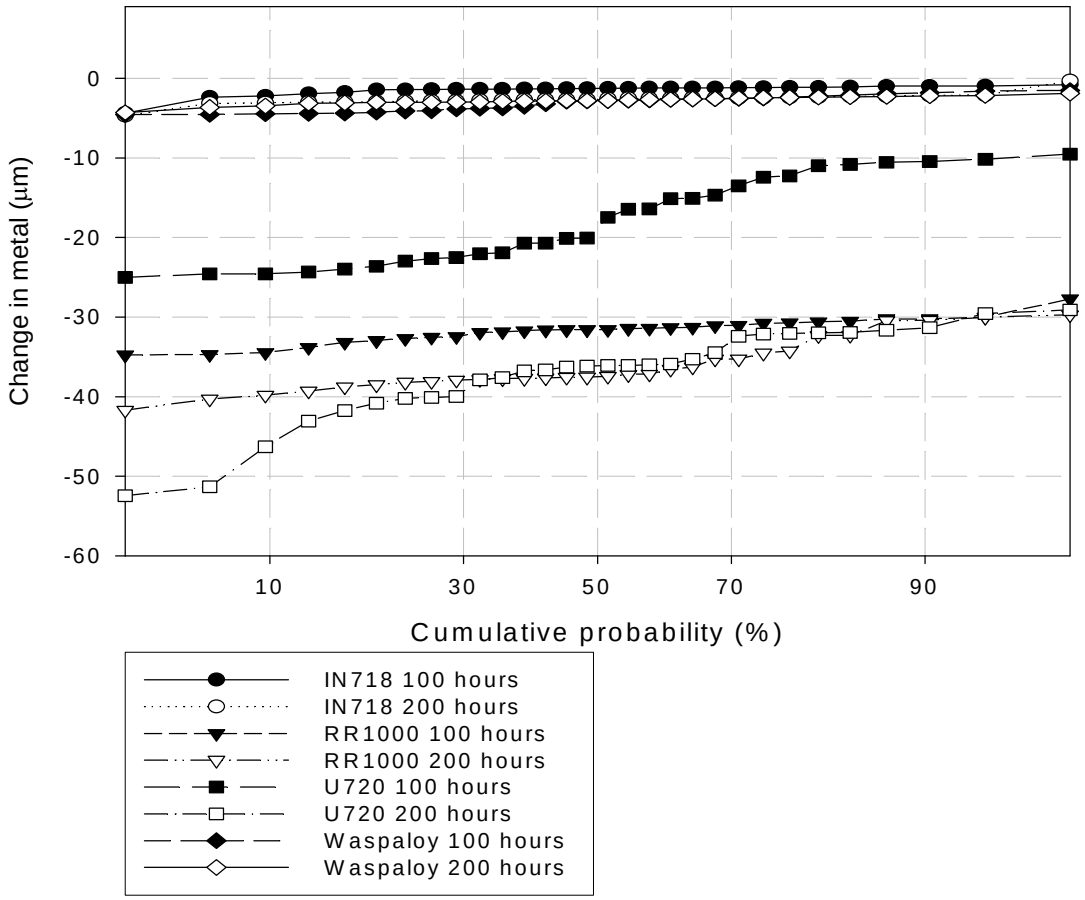

Figure 4.24: Cumulative normal probability plot for test 6 using 10 µg/cm²/h of a 2% NaCl 98% Na_2SO_4 deposit (change in metal scale from 0 to -60).

The cumulative probability plots for test 6 (Figure 4.24) at 650°C show greater metal loss for all the alloys than test 5 (Figure 4.22) at 620°C. As with the test 5 data at 620°C, IN718 and Waspaloy have been relatively unaffected by corrosion at 650°C whereas U720 and RR1000 samples show more significant damage. When comparing the cumulative weight change data for test 5 (Figure 4.21) and test 6 (Figure 4.23), test 5 exhibits a universally positive cumulative weight change and test 6 an almost universally negative cumulative weight change. This may infer that samples become afflicted by spalling to a greater degree when exposed at a higher temperature.

It should be noted in Figure 4.24 that one U720 sample appears to follow a corrosion trend similar to that of the RR1000 samples, whereas the other has suffered a more intermediate degree of attack in keeping with the previous tests results.

4.6 Test 7

Test 7's parameters are the same as the standard set by test 1. However the exposure time was limited to 100 and 200 hours to match those of tests 5 and 6 and allow direct comparisons to be made between these tests. The details of this test are as follows:

- Temperature: 700°C
- Materials: IN718, Waspaloy, U720 and RR1000
- Exposure times: 100 and 200 hours
- Deposit composition: 2% NaCl 98% Na_2SO_4 (molar %)
- Deposit flux: 10 µg/cm²/h
- Atmosphere: 300ppm SO_2 in air

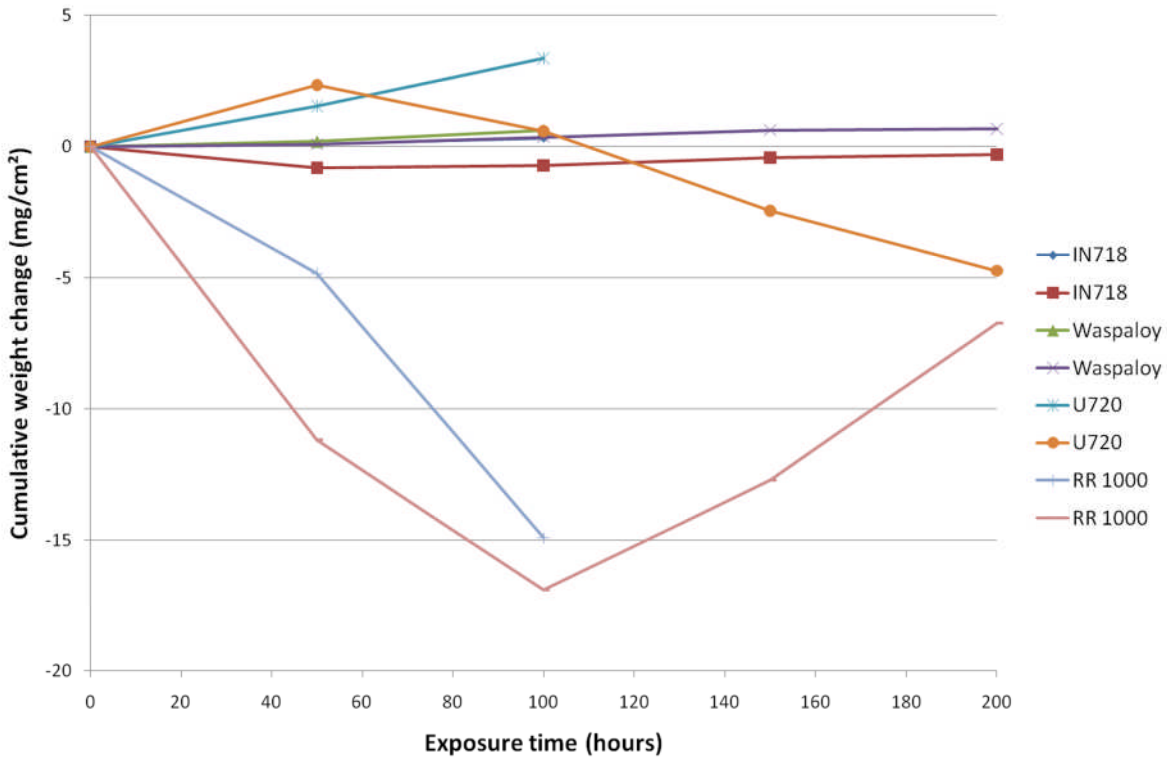

Figure 4.25: Test 7 weight change data using 10 µg/cm²/h of a 2% NaCl 98% Na_2SO_4 deposit.

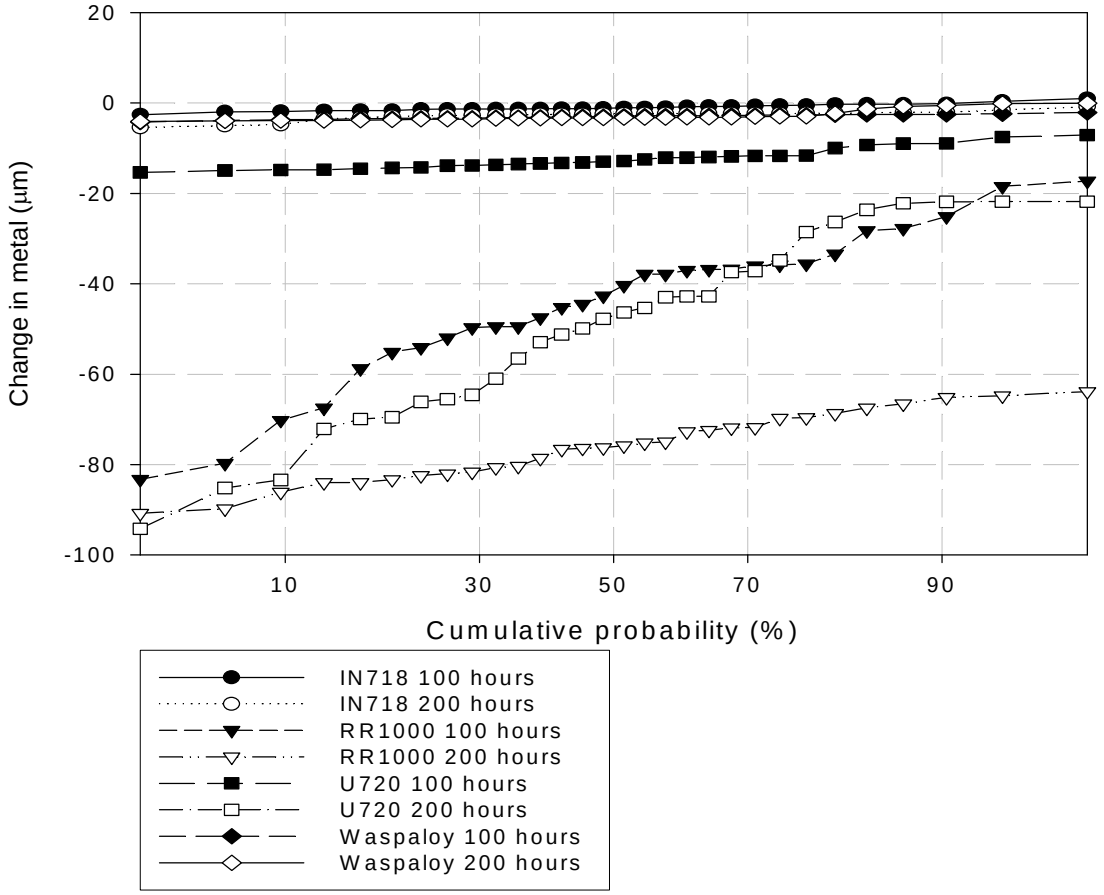

Figure 4.26: Cumulative normal probability plot for test 7 using 10 µg/cm²/h of a 2% NaCl 98% Na_2SO_4 deposit (change in metal scale from 20 -100).

Test 7's conditions mirror those of test 1 but include the alloy IN718 and uses exposure times of 100 and 200 hours. The results concur with the other tests in this study; IN718 and Waspaloy show very little corrosion damage after 200 hours of exposure whereas RR1000 and U720 exhibit higher levels of attack. However, Figure 4.26 shows that after 100 hours of exposure U720 has suffered only a minor degree of corrosion.

4.7 Test 8

Like test 6, this test aimed to investigate the effect of corrosion on various selected disc alloys at 650°C. However, whereas test 6 was limited to 200 hours of exposure, test 8 looks at the effects of a longer 500 hour exposure. The parameters of this test are listed below:

- Temperature: 650°C
- Materials: IN718, Waspaloy, U720 and RR1000
- Exposure times: 500 hours
- Deposit composition: 2% NaCl 98% Na_2SO_4 (molar %)
- Deposit flux: 10 µg/cm²/h
- Atmosphere: 300ppm SO_2 in air

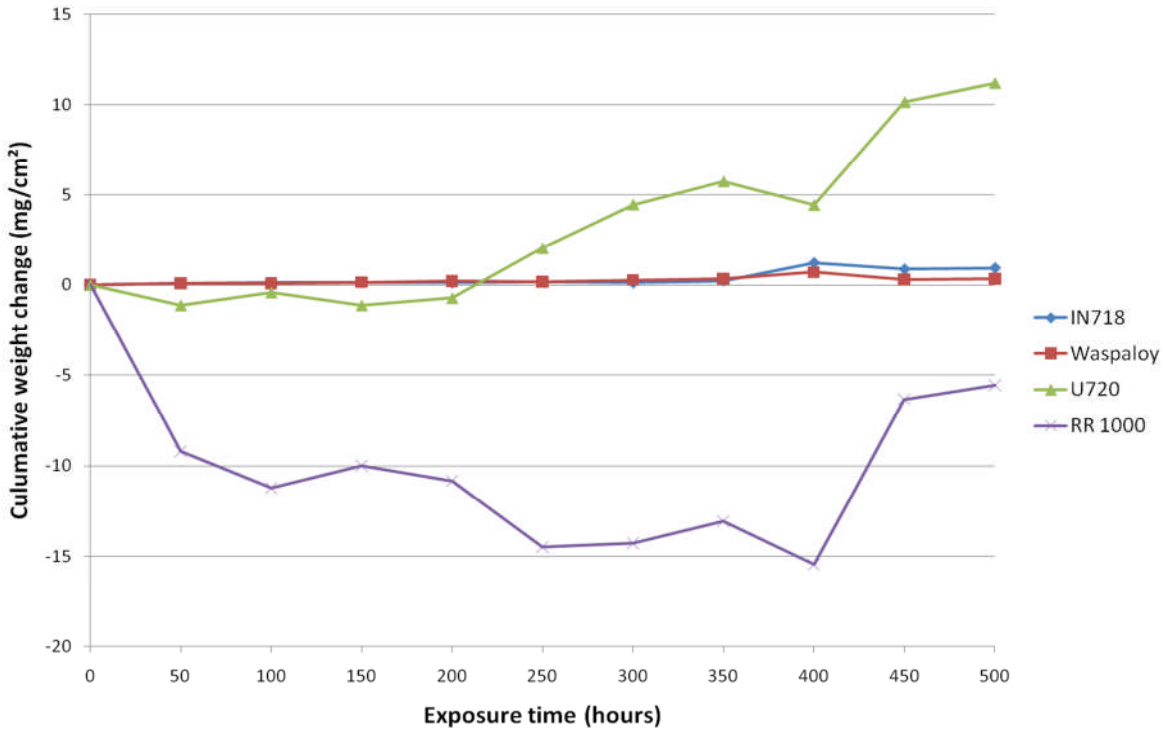

Figure 4.27: Test 8 weight change data using 10 µg/cm²/h of a 2% NaCl 98% Na_2SO_4 deposit.

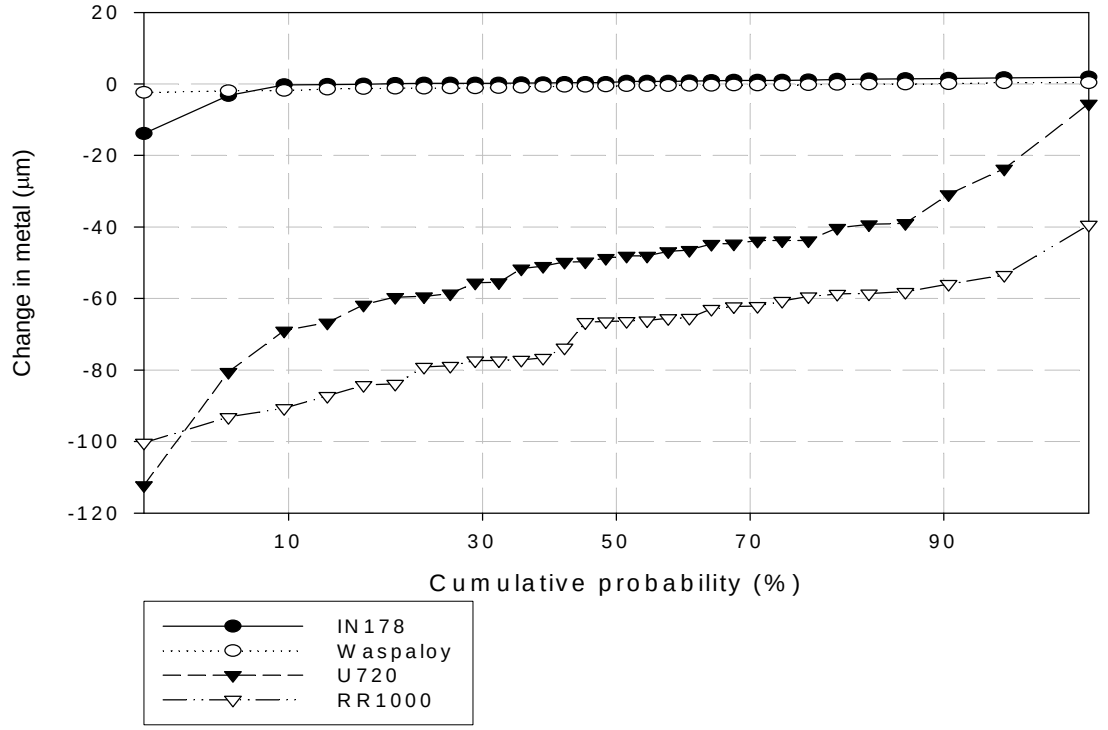

Figure 4.28: Cumulative normal probability plot for test 8 using 10 µg/cm²/h of a 2% NaCl 98% Na_2SO_4 deposit and an exposure time of 500 hours (change in metal scale from 20 to -120)

Test 8 uses the same test parameters as test 6, but extends the exposure time to 500 hours. Both Figures 4.27 and 4.28 Show that IN718 and Waspaloy still have not incurred significant corrosion damage. In comparison RR1000 and U720 have continued their rapid rate of corrosion as seen in test 6.

At a low level of probability, the alloy IN178 has begun to show a small degree of corrosion. This is likely to correspond to the early stages of the formation of a pit feature and it could be hypothesized that if the test were to continue for longer the rate of corrosion would increase.

4.8 Test 9

The alloy RR1000 used in the earlier tests of this study had an unknown grain size. This test utilized RR1000 samples manufactured to have a specifically coarse grain to provide a comparison with the earlier tests. The test conditions mirror the standard set by test 1 and are listed below:

- Temperature: 700°C
- Materials: RR1000 (course grain)
- Exposure times: 100, 200 and 500 hours
- Deposit composition: 2% NaCl 98% Na_2SO_4 (molar %)
- Deposit flux: 10 µg/cm²/h
- Atmosphere: 300ppm SO_2 in air

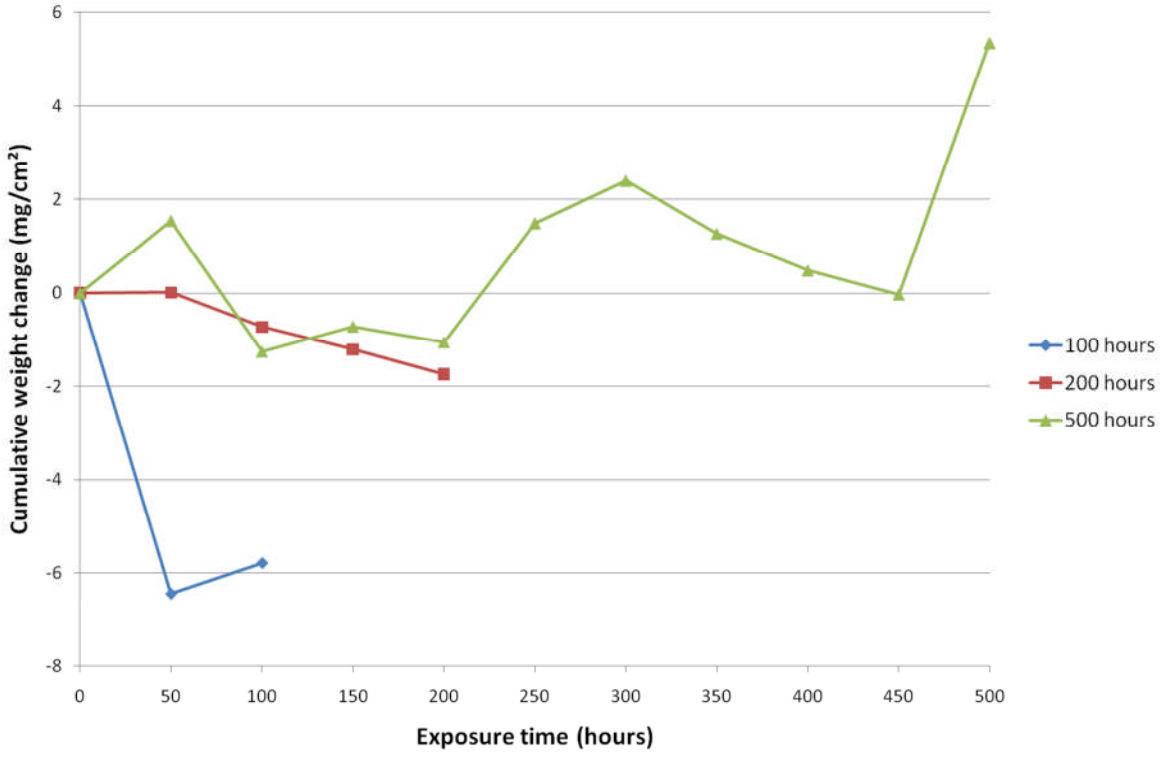

Figure 4.29: Test 9 RR 1000 course grain samples weight change data using 10 µg/cm²/h of a 2% NaCl 98% Na_2SO_4 deposit.

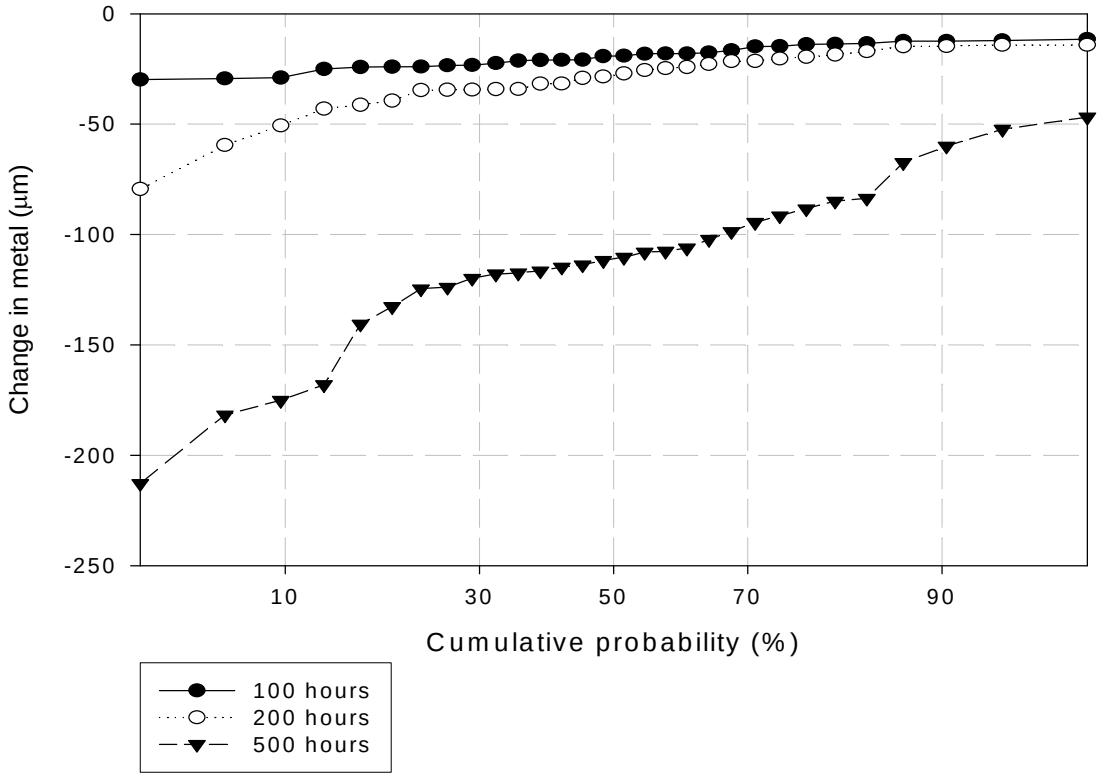

Figure 4.30: Test 9 RR 1000 course grain cumulative normal probability plots using 10 µg/cm²/h of a 2% NaCl 98% Na_2SO_4 deposit.

Figure 4.30 shows relatively little difference in the median metal loss of samples exposed for 100 and 200 hours when compared to the sample exposed for 500 hours. However the data series for 200 hours of exposure shows an increased degree of metal loss at a low level of probability for the samples exposed for longer than 100 hours. As previously mentioned, this indicates the presence of pitting features. The erratic cumulative weight change data presented in Figure 4.29 seems not to bare much relation to the measured metal loss data in Figure 4.30.

5. Discussion

As discussed in chapter 1, the further development in efficiency of jet turbines has led to a desire for higher operating temperatures. As a consequence, there is a need to accurately assess and better understand the corrosion of alloys involved in the hot gas pathway of a jet engine under a variety of new parameters. Additionally, flying over or through different environments can lead to a variation in particles passing through the engine and depositing on various gas turbine components. Therefore it is important to better understand the relationship between deposit composition and flux, and hot corrosion.

In this chapter the hot corrosion mechanism is identified and a case is made for the use of dimensional metal loss as a method for measuring corrosion. Then, data from the different corrosion tests is combined to investigate the effects of specific parameters including the following:

- Alloy type and composition
- Deposit flux and composition
- Grain size and the effect of shot peening
- Exposure temperature

5.1 Hot corrosion mechanism

To draw meaningful conclusions from the test data and to develop models of corrosion performance, it is essential to first identify the mechanism of hot corrosion taking place. Based on the literature concerning this topic (discussed in Chapter 2.5), type II hot corrosion would be expected because the exposure temperatures were between 620 and 750°C. This type of hot corrosion tends to produce areas of localised attack in the form of pitting features which can easily be identified under a microscope. Gas phase induced type II hot corrosion does not allow the protective oxide scale to repair itself and therefore there should be no preferential depletion of alloying elements. Finally, when the acidic fluxing mechanism is in effect, oxides of nickel and cobalt tend to precipitate out at the gas-deposit interface whereas the oxides and sulphates of other alloying elements are formed closer to the deposit-metal interface. Such an elemental distribution can be identified using an ESEM (demonstrated in Chapter 3.4).

Figure 5.1 shows that the surfaces of RR1000, U720 and Waspaloy have all undergone an uneven form of attack with no internal damage below the surface. In addition, where it has not spalled away, the corrosion product has built up in layers of two different products. Figure 5.2 shows a backscattered electron image of a pit feature on a U720 sample. Generally speaking, the surface of RR1000 samples appeared to be more evenly attacked

than the other samples tested, this is reflected in the cumulative probability of metal loss graphs in chapter 4. However it is likely that this is not caused by the absence of pit features, but rather the pits developing in such a way that they cover the whole sample surface.

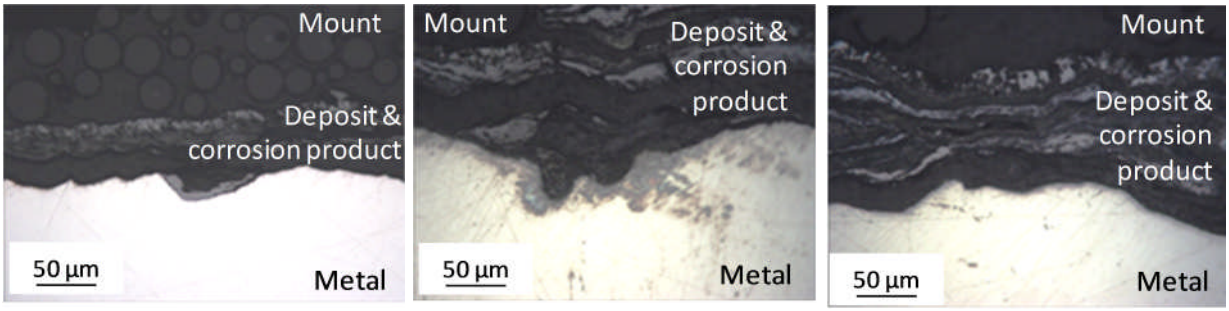

Figure 5.1: Optical micrographs of RR1000 (left), U720 (middle) and Waspaloy (right) after 500 hours of exposure in test 1.

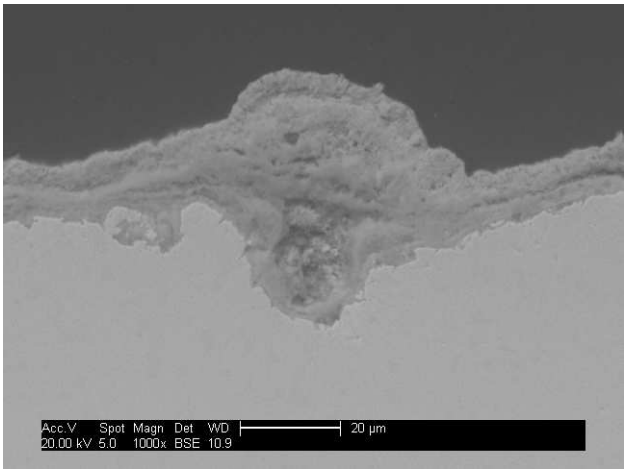

Figure 5.2: Backscattered electron image of U720 exposed in test 1 (using 10 µg/cm²/h of a 2% NaCl 98% Na_2SO_4 deposit for 500 hours at 700°C) showing a typical pitting feature.

The EDX analysis capabilities of an ESEM have been used to analyse the elemental distribution close to the metal surface and in the corrosion product. Examples of these are shown in Figures 5.3, 5.4 and 5.5 for RR1000, U720 and Waspaloy respectively. These images show that there has been no preferential depletion of elements at the sample surface. Additionally, the corrosion product has formed into two layers; the inner layer is predominately oxides and sulphates of chromium whereas the outer layer is mostly made up from oxides of nickel and cobalt. It should be noted that the energy of major electron transition peaks for molybdenum and sulphur is very similar and so the EDX software cannot reliably distinguish between these two elements. However, the maps show molybdenum and sulphur are present in the inner layer of corrosion product with only trace amounts in the outer layer so while the identification between these two elements may be in question, the location is not.

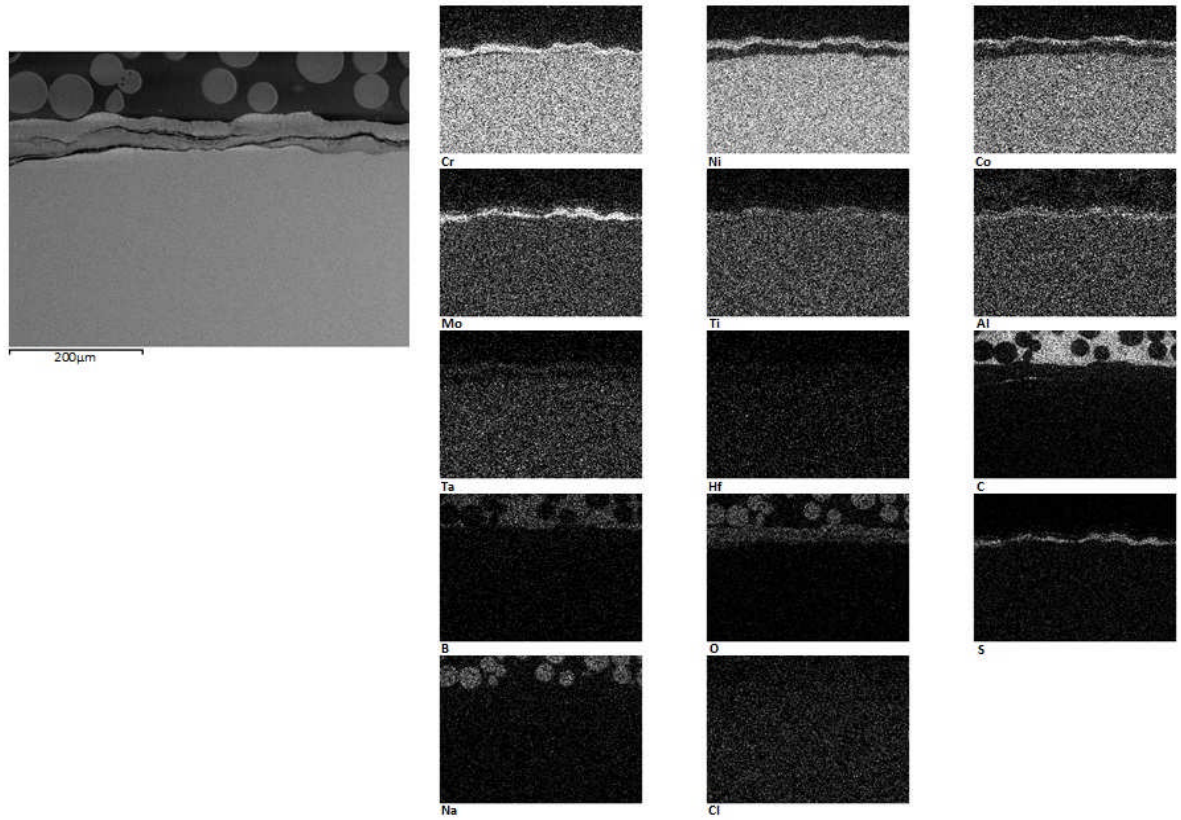

Figure 5.3: EDX images showing the elemental distribution in RR1000 after 500 hours of exposure in test 1 (using 10 µg/cm²/h of a 2% NaCl 98% Na_2SO_4 deposit at 700°C).

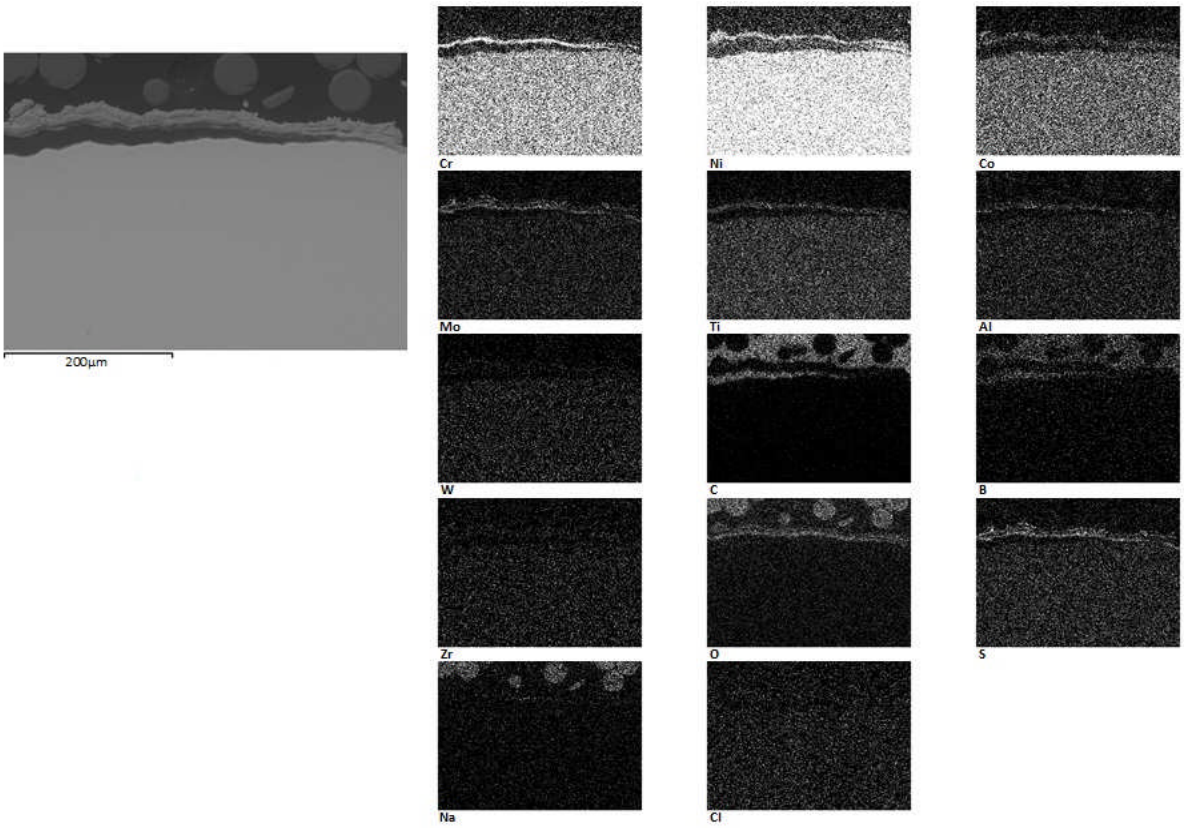

Figure 5.4: EDX images showing the elemental distribution if U720 after 500 hours of exposure in test 1 (using 10 µg/cm²/h of a 2% NaCl 98% Na_2SO_4 deposit at 700°C).

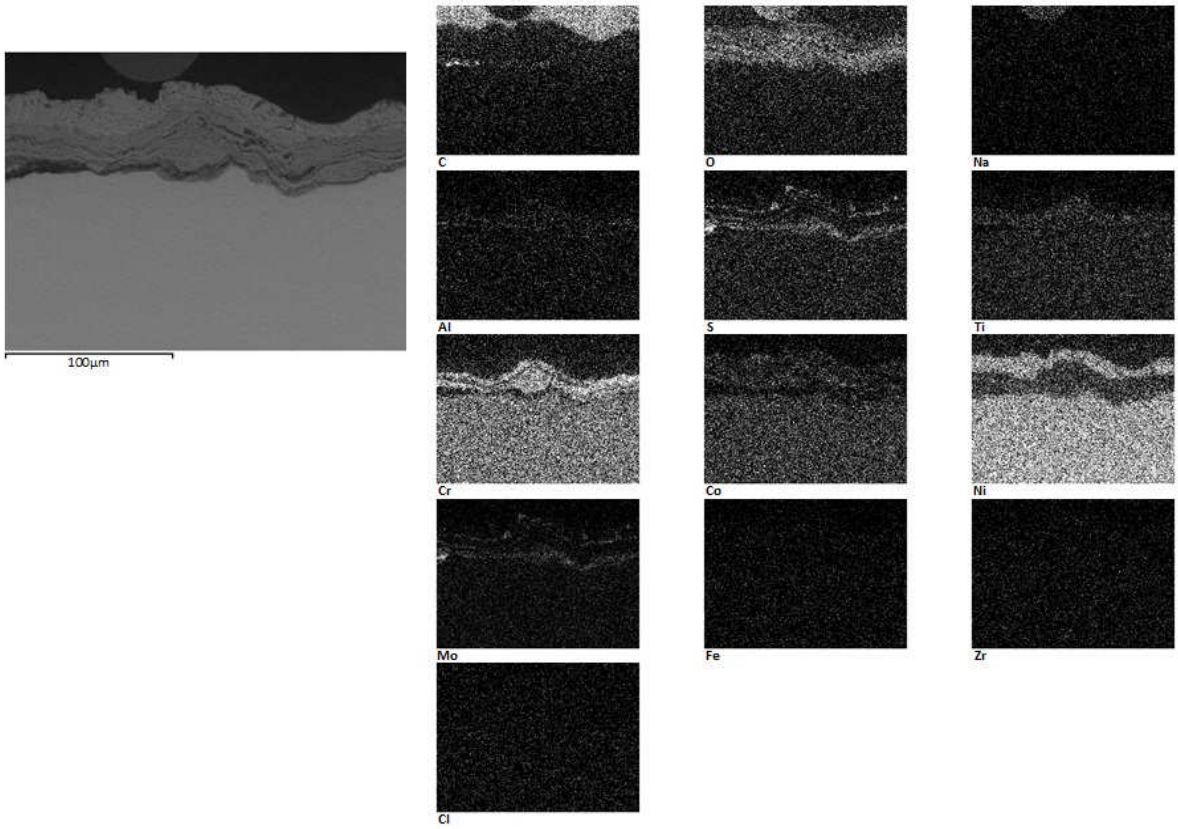

Figure 5.5: EDX images showing the elemental distribution in Waspaloy after 500 hours of exposure in test 1 (using 10 µg/cm²/h of a 2% NaCl 98% Na_2SO_4 deposit at 700°C).

The morphological features observed using optical and ESEM microscopy combined with the elemental distribution obtained via EDX mapping confirm that type II corrosion has occurred and that it has followed an acidic fluxing mechanism. It is most likely that the acidic conditions are established by the gas phase, however it is not certain that other elemental species from within the alloy are not contributing in some way or indeed if such a contribution would have any noticeable effect on the corrosion process. Although the type II corrosion features may differ slightly between the alloys, they do still pertain to the same type of corrosion degradation mechanism.

5.2 Rationalization of the metrological approach

Although the phenomenon of hot corrosion is well recognised, there is no consensus regarding the best method for quantifying it. Some studies present results in terms of weight change data, whereas others present dimensional metal loss data [6; 10; 21; 34]. A comparison between the cumulative weight change data and the median dimensional metal loss data for samples exposed in test 1 is shown in Figure 5.6.

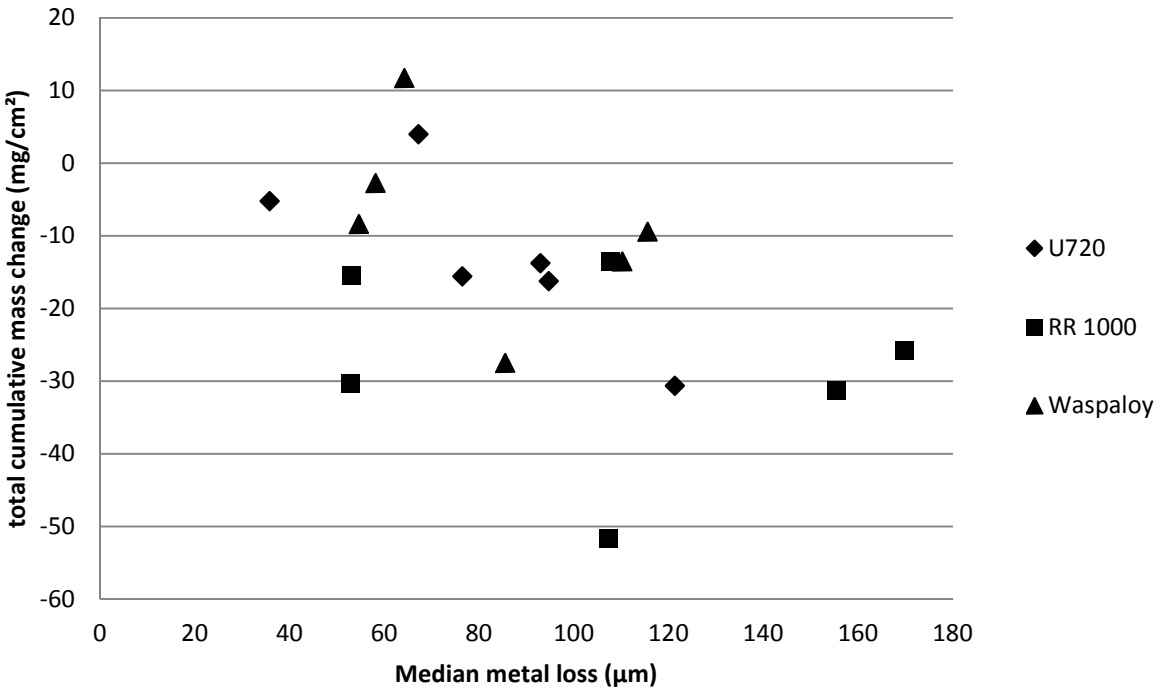

Figure 5.6: A comparison between weight change and measured metal loss for samples exposed in test 1.

Although the data in Figure 5.6 do show a slight correlation between mass change and median metal loss, there is a large enough variance between the data points to make the sole use of mass change data an unreliable measurement of corrosion damage. The discrepancy between the two types of measurement is most likely due to the sporadic and inconsistent nature of the spalling of oxides and corrosion products from the sample surfaces and the localised nature of pitting. Indeed, the nature of sample spalling inevitably introduces an element of variation in the corrosion test process. Alloys that have entered the propagation stage of the corrosion sequence, and therefore suffered greater damage, have a larger discrepancy between the two types of measurement as spalling becomes a more important factor. Some earlier studies eliminated this source of variation by deliberately removing the corrosion product from the sample surface prior to each deposit recoat. However, this method further removes the test from the practical environment where accumulated corrosion product and various degrees of spalling exist and may influence the progression of corrosion.

Mass change data can be a useful tool, easy to measure and non-destructive for each sample, and giving a general corrosion performance indication. These features make such data useful for comparisons to other studies that make exclusive use of this type of data. However, mass change data is unable to give an indication of the distribution of damage depths and specific morphological features such as sample pitting, which can be a common feature of type II hot corrosion and can cause the premature failure of engine components.

Therefore, while mass change data may be able to give a general corrosion performance indication for an alloy, it is not as accurate as dimensional metrology for more robust comparisons and does not provide enough information for an in depth investigation into the corrosion damage where corrosion distribution data is needed.

5.3 Comparison of the different alloys performance in a type II hot corrosion regime

All the test data combines to give a good overview of the different superalloys' behaviours within a hot corrosion environment. These data can then be compared to the differences in the superalloys' compositions to identify which factors affect the corrosion performance and to quantify their effects. In terms of corrosion resistance, the concentration of the protective oxide scale forming element is most relevant and is therefore the focus of this discussion. The alloys involved in this study form Cr_2O_3 as a protective oxide scale. The full elemental compositions of these alloys were given Table 2.1.

Because manufacturers hope to improve the thermal efficiency of their engines by increasing the disc rim operating temperature to 700 °C or higher, most of the test data obtained has been exposed at this temperature with a specific deposit to match the practical environment (more recent comparisons with real jet engines suggest these conditions may be too aggressive and therefore results should be scaled accordingly). This study can make the best comparisons between the different superalloys at this temperature with fluxes of 10 µg/cm^2/h of a 98% Na_2SO_4 2% NaCl deposit. Under these conditions, the corrosion test program has focused on the following superalloys: RR1000, U720 and Waspaloy, of which the Cr content is 15%, 16% and 19.5% respectively. The combined data for all the superalloys exposed under these conditions is presented in Figures 5.7, 5.8 and 5.9.

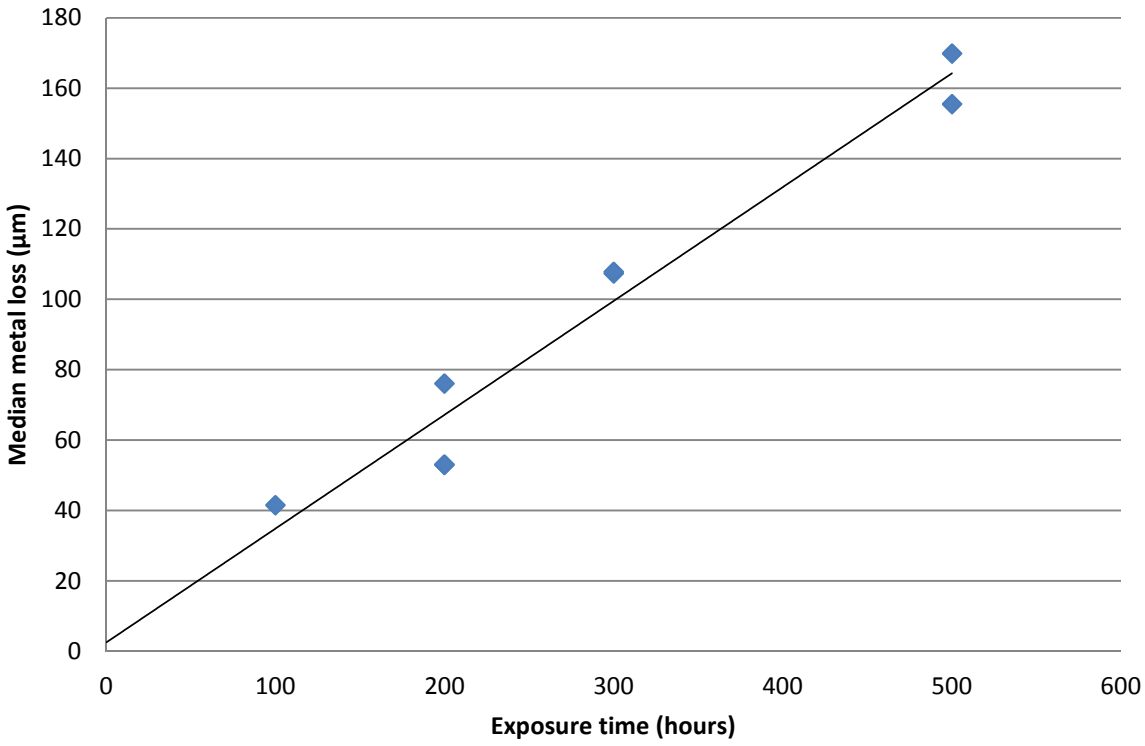

Figure 5.7: Median metal loss for RR1000 at 700°C with a deposition flux of 10 µg/cm^2/h of a 98% Na_2SO_4 2% NaCl deposit.

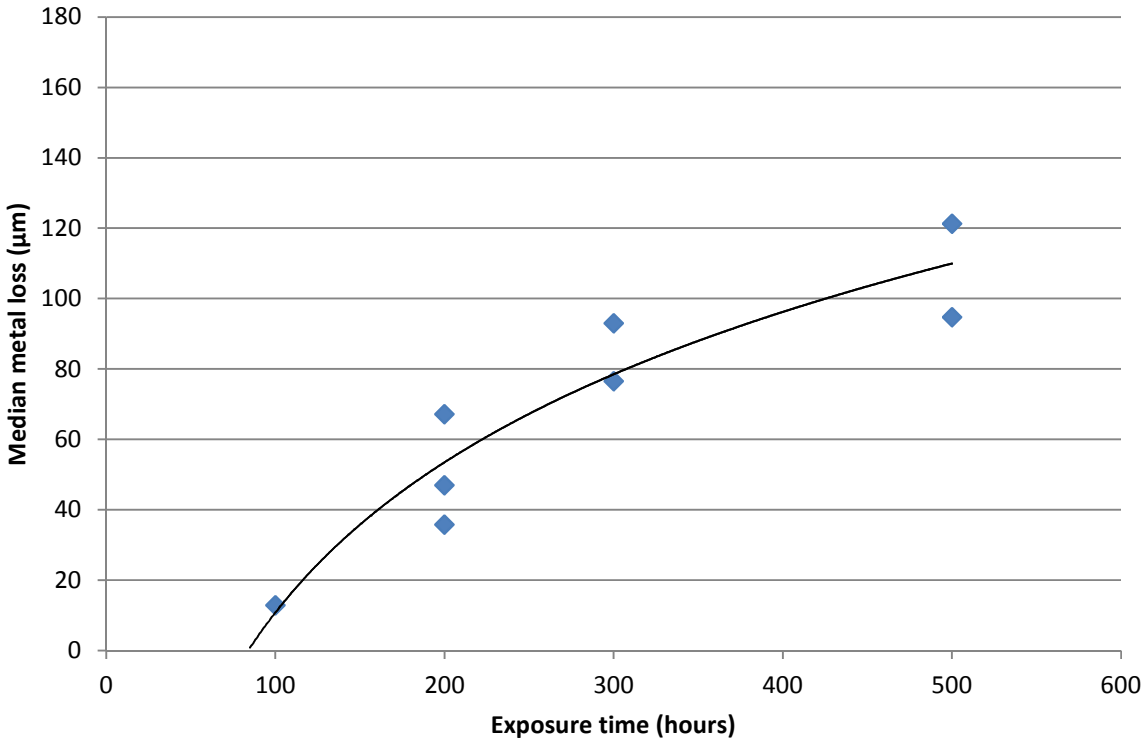

Figure 5.8: Median metal loss for U720 at 700°C with a deposition flux of 10 µg/cm^2/h of a 98% Na_2SO_4 2% NaCl deposit.

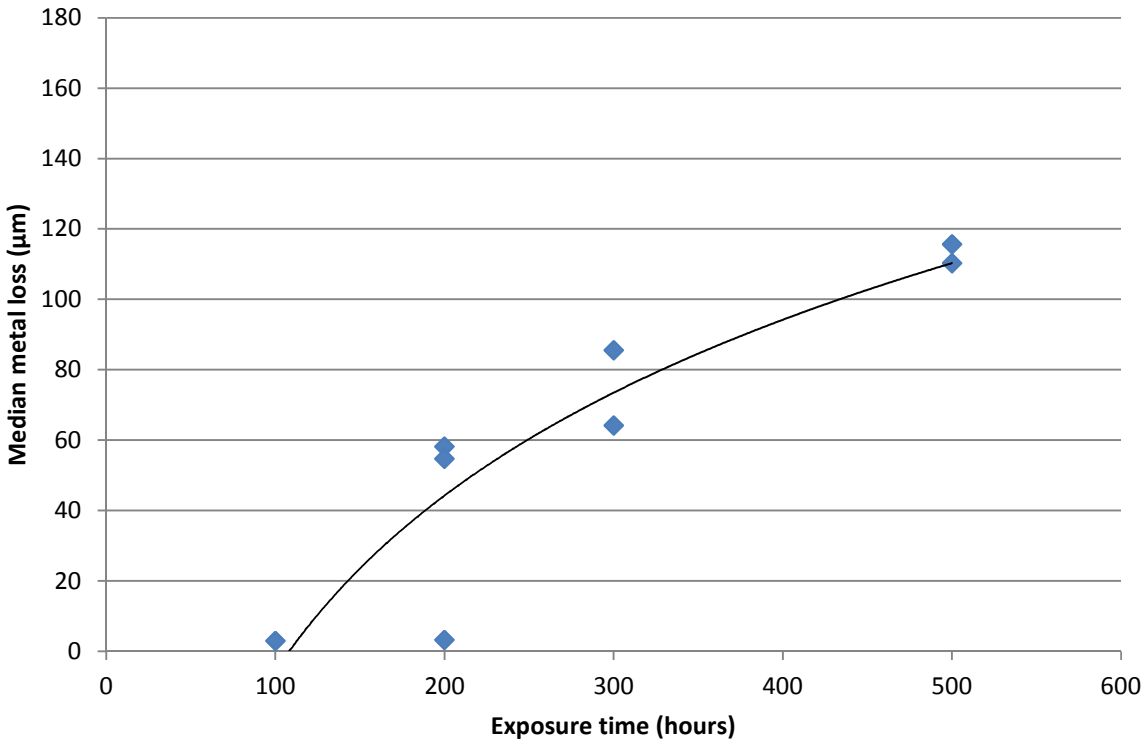

Figure 5.9: Median metal loss for Waspaloy at 700°C with a deposition flux of 10 µg/cm^2/h of a 98% Na_2SO_4 2% NaCl deposit.

Figure 5.7 shows that the median metal loss for RR1000 seems to follow a linear trend over the 500 hour test period whereas Figures 5.8 (U720) and 5.9 (Waspaloy), are depicted with non-linear trend lines. Because corrosion tests are not reproducible to an exact degree of accuracy and the test programme had only a limited number of samples, the identification of the trend lines on these figures may be unreliable. However, by extrapolating the trend lines backward to the points where they cross the zero metal loss, the approximate length of the corrosion incubation period can be deduced.

One can see in Figure 5.7 that the RR1000 trend line crosses the abscissa at a point close to the origin inferring a short incubation period; possibly only a few hours. In contrast, Figure 5.8 shows U720 to have an incubation period of approximately 80 hours; whereas Waspaloy is shown to have an incubation period of ~110 hours in Figure 5.9. Because the smallest increment in the corrosion test length is at 100 hours, these incubation period values can only be approximate; however they are suitable for use in preliminary models.

Because of the inherent errors in replicating corrosion test data, statistical analysis is more accurate using the mean of a large sample population. However this approach is balanced against the cost in both resources and time of such experimentation. Figure 5.10 shows a plot of the mean median metal loss for the alloys RR1000, U720 and Waspaloy. The corrosion rates for all three alloys are initially faster and then slow down after the 300 hour

point; although this is only slight for RR1000. Indeed, there is not a great difference in the gradient for all three alloys; the biggest difference is in the time lapse before rapid corrosion occurs. This indicates that corrosion rate after the incubation period is not significantly altered by changing the alloy composition and that developing superalloys to withstand hot corrosion should focus on extending the length of the incubation period.

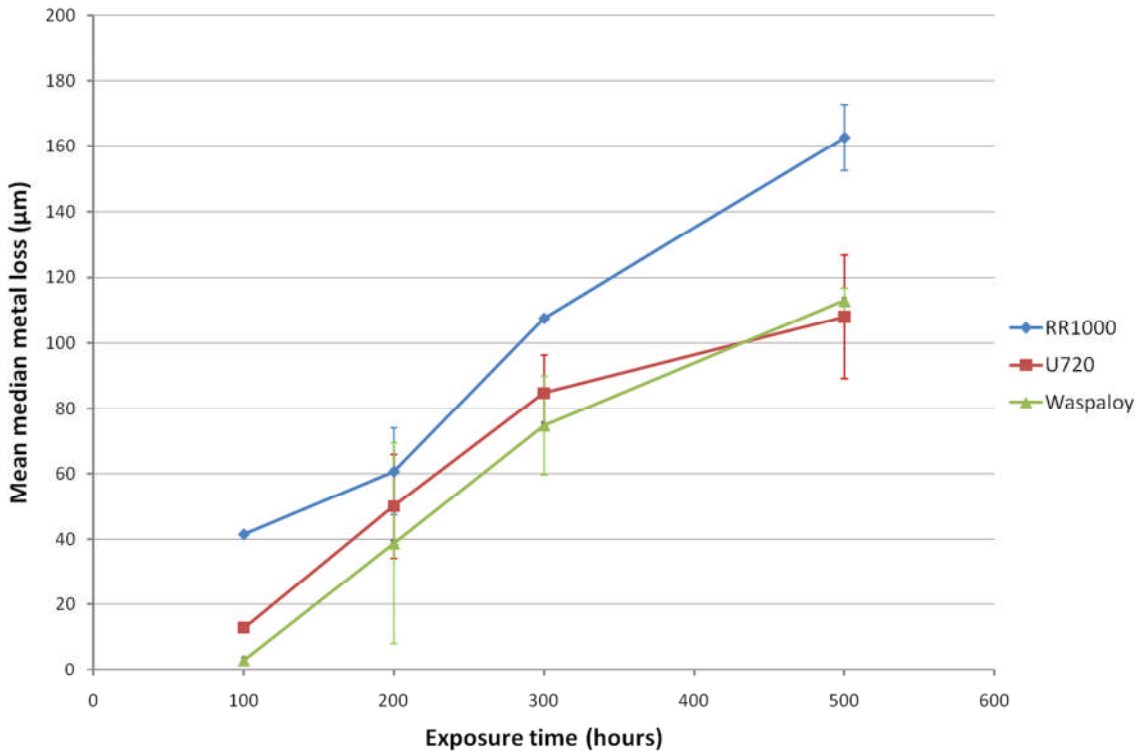

Figure 5.10: Mean median metal loss plot for RR1000, U720 and Waspaloy in the standard test conditions set by test 1 (error bars show the standard deviation from the mean).

Although the median metal loss data shows generally how corroded an alloy sample is, it does not take into account the presence of pitting features. As discussed in Chapter 2, the presence of such features can cause premature component failure and are therefore an important factor when predicting alloy life spans. The 4% probability of metal loss exceedance effectively shows the greatest degree of metal loss on each sample, which in most cases corresponds to a pit feature. A graphical plot of the mean 4% probability of metal loss is shown in Figure 5.11.

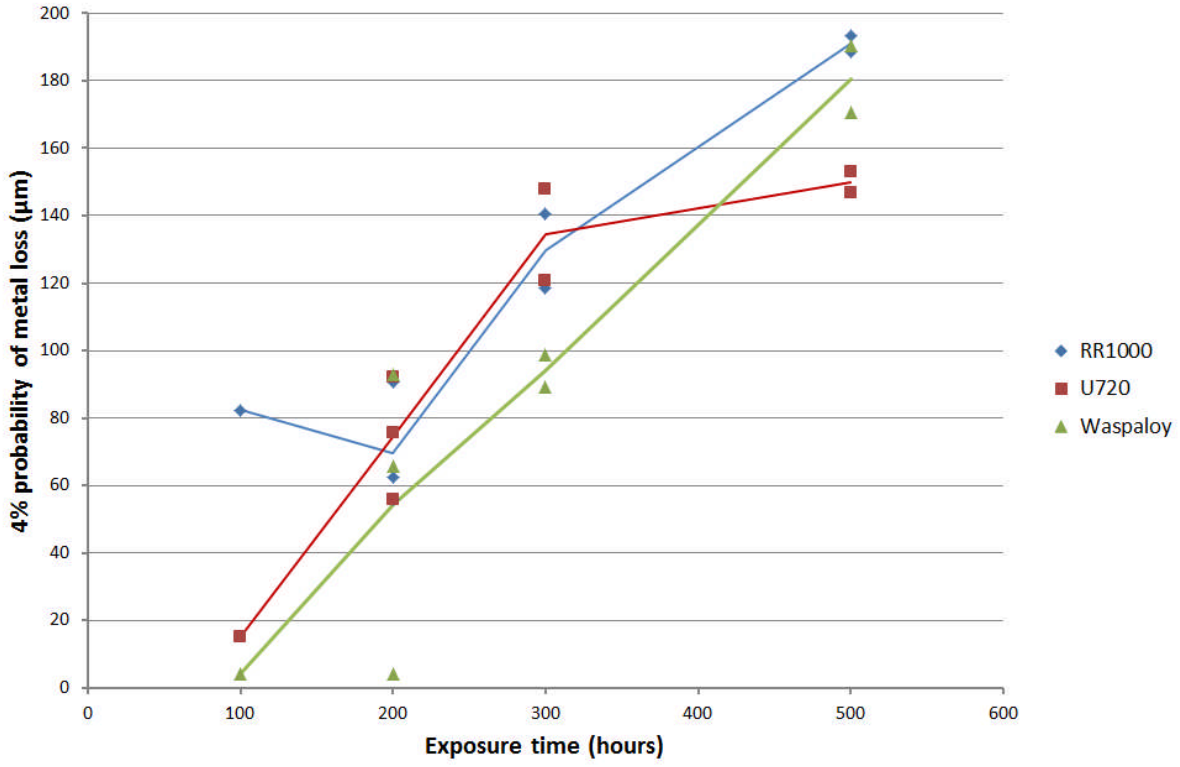

Figure 5.11: Mean metal loss with a 4% chance of exceedance plot for RR1000, U720 and Waspaloy in the standard test conditions set by test 1. The trend lines follow the average for each series at any given exposure time.

When comparing the mean median metal loss (Figure 5.10) with the 4% probability of metal loss exceedance (Figure 5.11), it can be seen that the data plot for the 4% probability has a steeper gradient than the median metal loss plot, but is otherwise very similar. If extrapolated back to zero metal loss, U720 and Waspaloy would cross the abscissa at approximately the same point on both graphs (U720 at between ~70 and 80 hours, and Waspaloy ~90 hours). This indicates that pitting features do not start to form until the corrosion process has entered the propagation stage and therefore median metal loss data is suitable statistic to base an experimental model on. Aside from at 100 hours, the 4% probability of metal loss exceedance for RR1000 is much closer to the data plots of the other alloys than the median metal loss data after 200 hours of exposure. However, this is misleading as a gauge of performance since the rate of corrosion in the degradation stage is not as relevant as the length of the incubation stage.

5.4: The effect of deposit flux and salt composition

Data from tests 1 and 2 can be used to investigate the effect that deposit flux and salt composition has on the hot corrosion process for superalloys RR1000, U720 and Waspaloy. Test 1 used 10 µg/cm²/h of a 98% Na_2SO_4 2% NaCl deposit; this data can be used as a standard when compared to test 2 data which used 10 µg/cm²/h of a 95% Na_2SO_4 5% NaCl deposit and 2 µg/cm²/h of a 98% Na_2SO_4 2% NaCl respectively.

The full data obtained from tests 1 and 2 are shown in chapter 4; to make comparisons between the different deposit setups, the mean median measured metal loss of the duplicate samples in both tests has been plotted in Figures 5.12, 5.13 and 5.14.

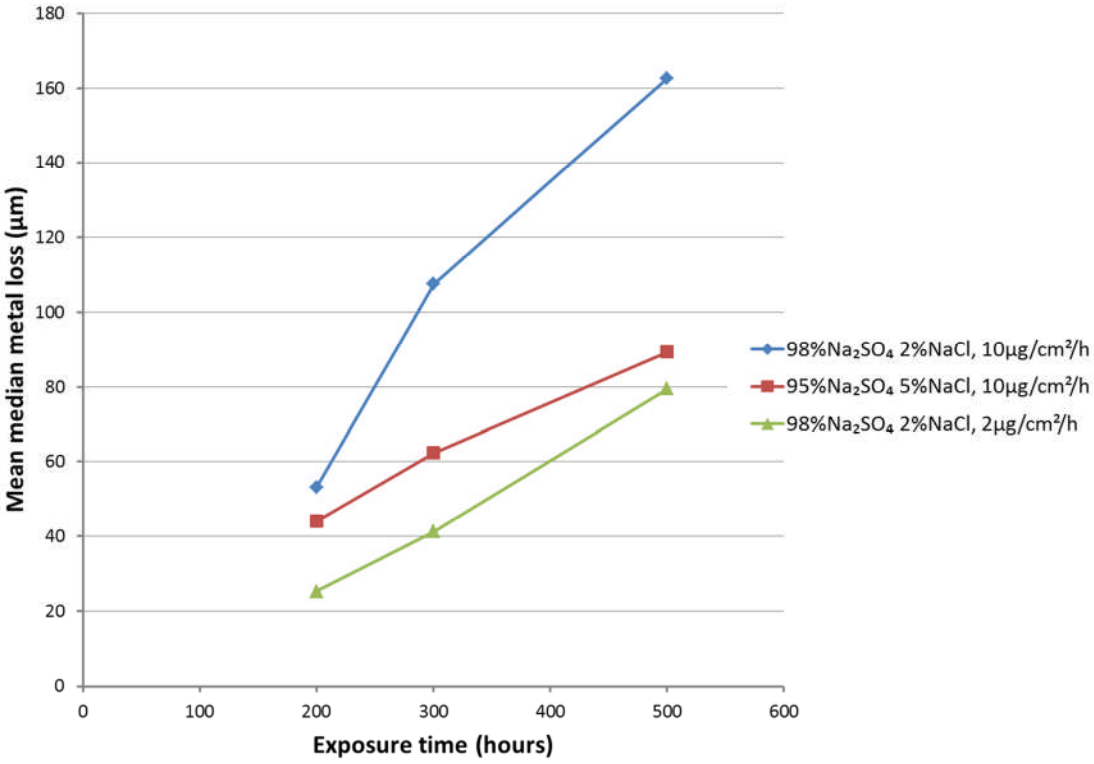

Figure 5.12: Mean median metal loss plot for RR1000 with various deposit compositions and fluxes derived from test 1 and 2 data exposed at 700°C.

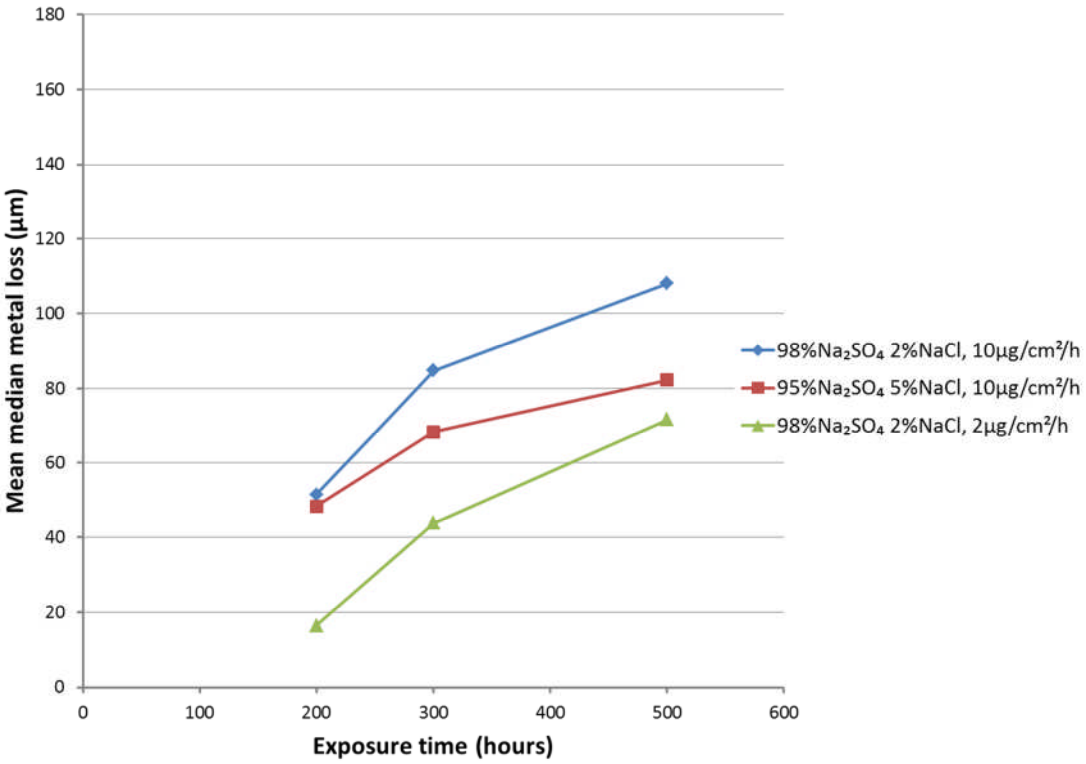

Figure 5.13: Mean median metal loss plot for U720 with various deposit compositions and fluxes derived from test 1 and 2 data exposed at 700°C.

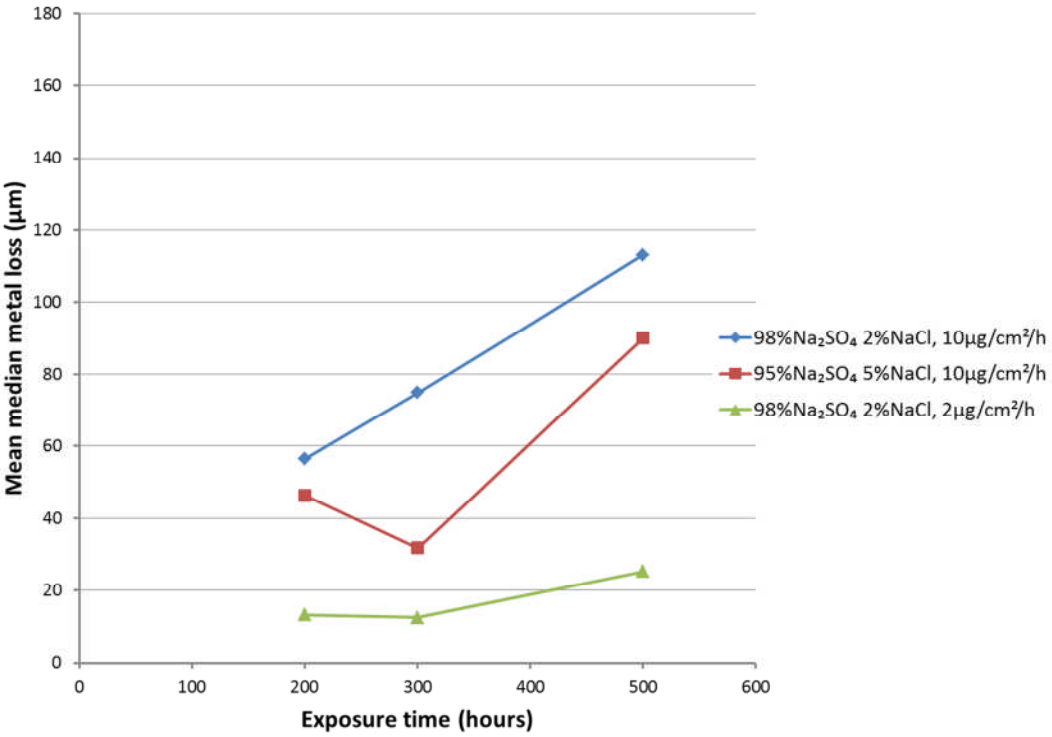

Figure 5.14: Mean median metal loss plot for Waspaloy with various deposit compositions and fluxes derived from test 1 and 2 data exposed at 700°C.

Figures 5.12, 5.13 and 5.14 show that both changing the deposit composition to 95% Na_2SO_4 5% NaCl and reducing the deposition flux to 2 µg/cm²/h have the effect of reducing the overall level of corrosion damage. Regarding the deposit composition, the degree of corrosion suffered after 200 hours of exposure for both deposit compositions is relatively close. However, it is also apparent that the corrosion damage after 200 hours of exposure is greater when 98% Na_2SO_4 2% NaCl is deposited compared to 95% Na_2SO_4 5% NaCl. These results suggest that the reaction between the Na_2SO_4 in the deposit and the SO_2/SO_3 in the gas phase is a rate limiting factor. As might be expected, the magnitude of the difference in corrosion rate is influenced by the corrosion performance of the alloy; RR1000 shows a much greater increase than U720 or Waspaloy. The EDX images in section 5.1 (Figures 5.3, 5.4 and 5.5) do not show any sodium or chlorine on the surface of the sample or in the corrosion product, therefore it is likely that they have evaporated.

Figures 5.12, 5.13 and 5.14 also show that reducing the deposition flux applied at each recoat to 2 µg/cm²/h reduces the degree of corrosion incurred. However, the rate of corrosion damage after the 200 hour point for RR1000 and U720 remains approximately the same as the corrosion when using 10 µg/cm²/h of deposit on the same alloy (therefore the trend lines for these different fluxes are seen to run in parallel). The degree of corrosion suffered by Waspaloy remains relatively low over the 500 hour period for the lower quantity of deposit. This data suggests that the flux of the salt deposit affects the length of the initiation period but not the rate of attack during the propagation period of the corrosion process. The corrosion rates remain low for Waspaloy because the lower deposition flux is insufficient to complete the initiation period during the 500 hour exposure time or it completes this stage close to the 500 hour point.

Because of the destructive nature of the sample analysis, dimensional measurements of the corrosion damage were only taken at 200, 300 and 500 hours in tests 1 and 2. The data obtained suggests that, apart from Waspaloy with 2 µg/cm²/h of deposit, the initiation period for all the alloys and conditions is less than 200 hours. Therefore to more accurately model the corrosion performance of these superalloys in these specific conditions, data need to be measured at more frequent time intervals.

Although these data show the effect of increasing the percentage of NaCl in the deposit, it does not fully explore the relationship between deposit composition and corrosion. To do so, future work could focus on testing different deposit compositions. Previous research [22] has shown that altering the composition of a deposit containing Na_2SO_4 cannot completely inhibit the corrosion process, but it has not yet established the deposit compositions that equate to a maxima or minima of corrosion.

5.5: The effect of alloy grain size and shot peening.

By comparing the test 1 RR1000 median metal loss data with that of tests 3 and 9, the effects of metal grain size and surface preparation can be observed. The test 3 RR1000 samples were shot peened prior to exposure; a technique whereby the surface is bombarded by small beads of a hard material. The purpose of this is to compress the surface grains, creating dislocations near to the surface of the alloy which allows faster transport of metal ions to the surface and thus promoting the growth of a more protective oxide scale. Test 9 involved RR1000 samples manufactured to have a larger grain size than those of the previous tests. These samples were investigated using Focused Ion Beam (FIB) techniques to observe the grain structure and shot peened effect on the alloy prior to exposure. FIB techniques were developed to prepare samples for use in Transmission Electron Microscopy (TEM) by sputtering away trenches either side of a targeted area. In this case, the FIB technique was used to cut away a single trench to allow imaging of grain structures in the near sub-surface region. To protect the surface during the sputtering process, a layer of Pt was deposited in situ. The grain structure of both test 3 and test 9 RR1000 samples can be seen in Figure 5.15.

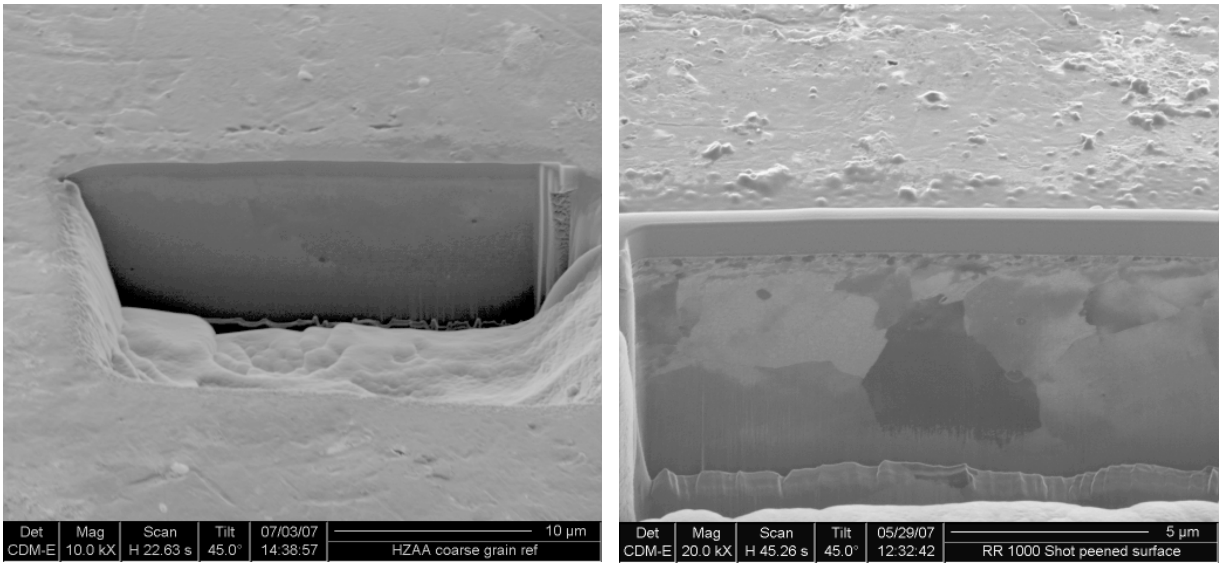

Figure 5.15: Focused ion beam micrograph of coarse grain RR1000 (left) and shot peened RR1000 (right).

Both increasing the grain size and shot peening the alloy surface can be seen to have improved the corrosion performance of RR1000 in Figure 5.16, with shot peening appearing to have a greater effect than increasing the grain size. If it is assumed that the grain size and initial shot peening does not affect the corrosion rate during the propagation stage of corrosion, then the trend line of standard RR1000 samples (which can be said to have a negligible incubation period) can be applied to the other samples to determine the length of the incubation period. This model of corrosion behaviour is shown in Figure 5.16; from this

the length of the incubation stage for coarse grain samples is calculated to be approximately 160 hours and for shot peened samples approximately 305 hours. However, this model does not consider that there may a small degree of metal loss incurred during the incubation stage of corrosion and therefore represents the minimum possible incubation length. If an approximate line of best fit is drawn for the incubation stage of the reaction, then the point at which it meets the propagation line represents the maximum possible length of the incubation stage. This model of corrosion is shown in Figure 5.17 and from this a maximum possible incubation length can be derived to be approximately 260 hours for coarse grain and 410 hours for shot peened samples, assuming that propagation rates are linear.

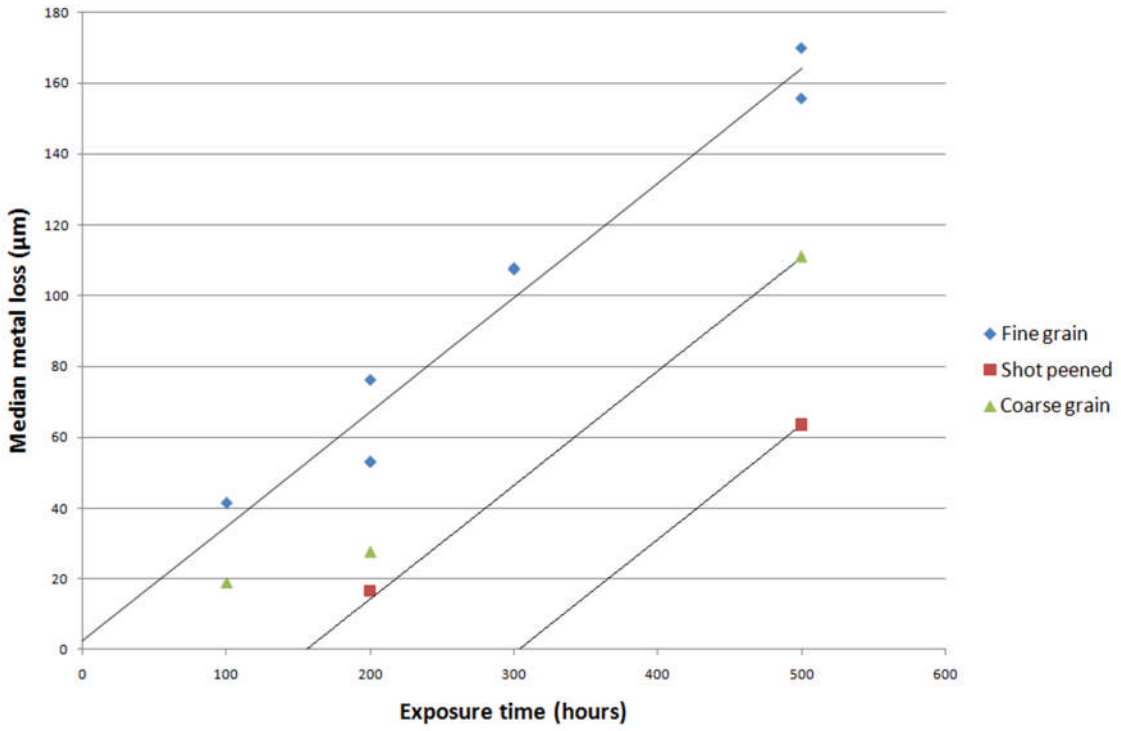

Figure 5.16: Median metal loss data for standard, coarse grain and shot peened RR1000 with trend lines following the rate of standard RR1000 extrapolated back from the 500 hour data. Tested at 700°C with a deposition flux of 10 µg/cm^2/h of 98% Na_2SO_4 2% NaCl.

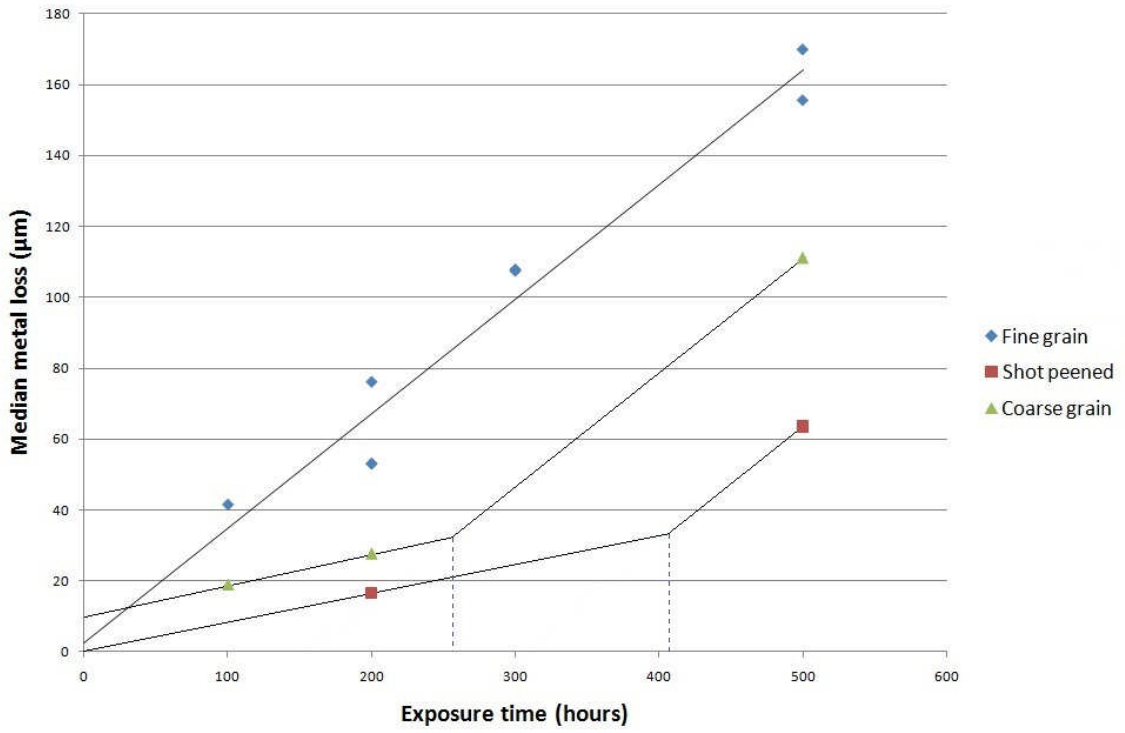

Figure: 5.17: Median metal loss data for standard, coarse grain and shot peened RR1000 with trend lines taking into account the incubation metal loss. Tested at 700°C with a deposition flux of 10 µg/cm^2/h 98% of Na_2SO_4 2% NaCl.

From these data it can be said that, for RR1000 samples, manufacturing to a coarse grain size has increased the incubation stage length by between 160 and 260 hours. Likewise, shot peening the surface of the sample has increased the incubation period by between 305 and 410 hours. Although these tests have produced relatively abundant data for standard RR1000 under test 1 conditions, the data for coarse grain size relies on 3 samples and just 2 for shot peened. Despite the median metal loss being calculated from 30 separate measurements per sample, some error causing factors could affect the whole sample systematically such as inaccuracies in applying the correct deposit flux. Therefore for a more accurate experimental model, further tests would be required with greater numbers of samples. In addition, as with all the tests in this study, by taking metal loss measurements at smaller time increments the transition between incubation and propagation stages can be more accurately observed and modelled.

Finally, the experimental data modelling the effect of grain size and shot peening only pertains to RR1000. The effect that these factors may have on other superalloys is likely to be positive, but maybe not by the same value because of the varying chromium content in other alloys.

5.6: The effect of exposure temperature.

The effect temperature has on the rate of hot corrosion has been thoroughly investigated in previous studies and is commented on in Chapter 2.5. During the course of this study's experimental work, alloys have been exposed at 620°C, 650°C, 700°C and (for shot peened RR1000) 750°C. These temperatures are all within the regime of type II hot corrosion and can provide confirmation of trends observed in previous work. Data sets from tests 5, 6 and 7 can be combined to indicate the performance of the various alloys over the temperature range; these data are presented graphically in Figures 5.18 and 5.19. Because the test at 750°C involved shot peened samples, the results cannot directly be compared with non-shot peened samples at lower temperatures. However, in chapter 4.3, Figure 4.20 can be used to compare the temperatures of 700°C and 750°C; this shows significantly less metal loss at 750°C.

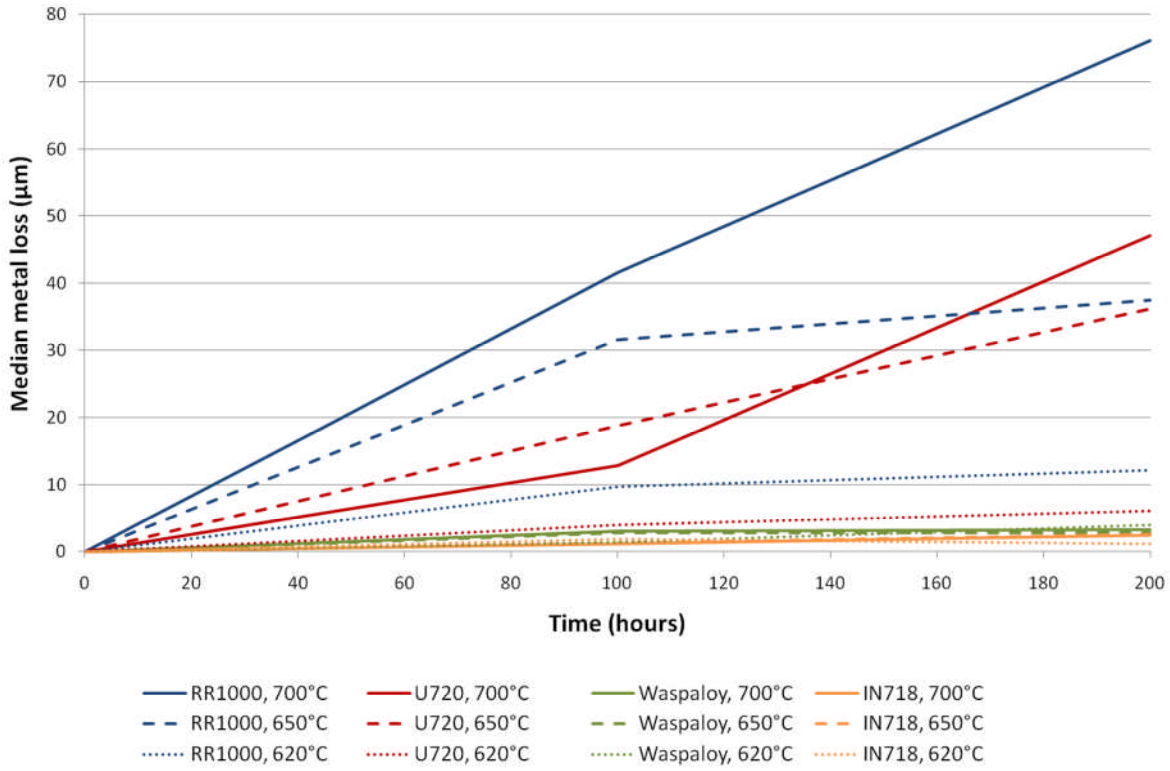

Figure 5.18: Combined median metal loss data for tests 5, 6 and 7 using 10 µg/cm²/h of a 2% NaCl 98% Na_2SO_4 deposit.

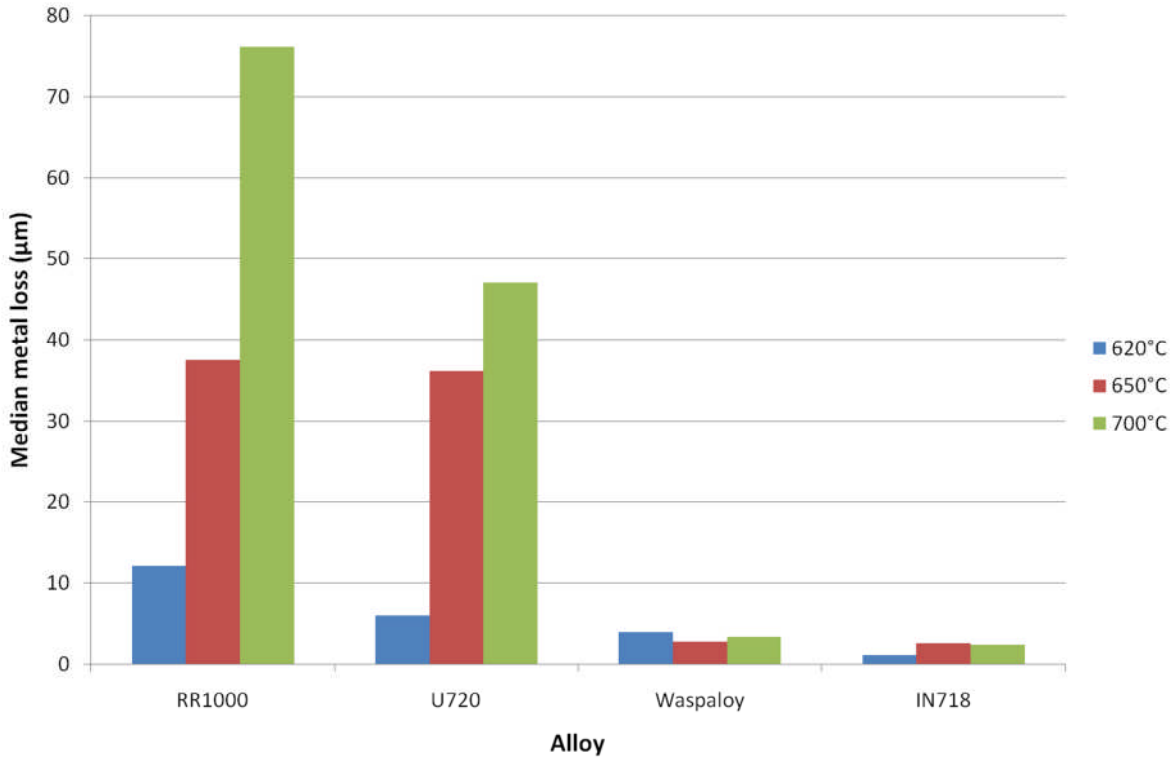

Figure 5.19: Combined median metal loss data for tests 5, 6 and 7 exposed for 200 hours using 10 µg/cm²/h of a 2% NaCl 98% Na_2SO_4 deposit.

Figures 5.18 and 5.19 show that, increasing the exposure temperature from 620°C to 700°C has the general effect of increasing corrosion damage. However, this trend cannot be observed for the alloys Waspaloy and IN718 which appear to remain in the initiation stage of hot corrosion for over 200 hours at all exposure temperatures.

In Figure 5.18, alloys RR1000 and U720 have clearly already passed into the propagation stage of hot corrosion at the 100 hour mark. It can be seen that the rate of corrosion for both these alloys between the 100 and 200 hour mark is greater at 700°C than 650°C. Therefore temperature seems to affect the actual rate of corrosion in the propagation stage rather than just altering the length of the initiation stage. Given that the rate of corrosion is generally slower at lower temperatures, it is difficult to determine what effect temperature has on the length of the initiation stage from these data. To further investigate this, the metal loss should be measured at more frequent time increments and over a longer exposure period.

6. Conclusions

A series of laboratory corrosion tests designed to reproduce the type of corrosion found on the disc section of a jet turbine engine have been carried out and successfully reproduced type II hot corrosion. These tests introduced the variables described in Chapter 1.2: alloy, deposit flux and type, temperature, grain size and the effect of shot peening.

It was found that for this type of corrosion damage, weight change data did not accurately correlate to measured metal loss. Therefore an argument has been made for using dimensional metal loss measurements over weight change data to quantify corrosion damage.

A correlation can be observed for the tested alloys between chromium content and median metal loss. This has been shown to be proportional to the length of the hot corrosion initiation stage rather than corrosion rate in the propagation stage. When exposed at 700°C using 10 µg/cm²/h of a 2% NaCl 98% Na_2SO_4 deposit, the incubation time for RR1000 (15% Cr) was found to be less than 20 hours, U720 (16% Cr) was approximately 80 hours and Waspaloy (19.5% Cr) approximately 110 hours.

Reducing the Na_2SO_4 and thereby increasing the NaCl composition of the deposit has the effect of overall reducing the degree of corrosion suffered as measured by median metal loss. EDX analysis at cross section surfaces did not find any trace of sodium or chlorine species, it is likely these species evaporated during the corrosion process and that SO_3^{2-} ions determine the reaction rate.

Reducing the deposition flux also reduces the degree of metal loss incurred although this relationship is not directly proportional. It was shown that this reduction in metal loss was caused by the lengthening of the incubation period; the rate of corrosion in the propagation period remained approximately the same.

An experimental model for RR1000 has been presented showing the effects of grain size and shot peening. Both features appear to have significantly extended the length of the incubation period; coarse grain size by between 160 and 260 hours, and shot peening by between 305 and 410 hours.

The rate of corrosion has been shown to increase with increasing exposure temperature between 620 and 700°C, and to decrease when further increasing the temperature from 700 to 750°C. This trend of the effect of temperature on type II hot corrosion degradation supports the literature which states type II corrosion rates peak at approximately 700°C.

6. Future work

Under the test conditions chosen for the majority of tests in this study, the length of the incubation stage was shorter than the shortest sample test period. To construct more accurate experimental models, samples should be investigated after much shorter increments of exposure time or under much less aggressive conditions. In addition, more data would help to confirm if corrosion rates are linear in each of the hot corrosion stages.

This study considers a number of variables including deposit flux and composition, temperature, grain size and the effect of shot peening. However it does not investigate these variables in great detail, to do so would require a much more extensive testing program such as a wider range of deposit compositions. Of particular interest to the manufacturing industry would be to determine the most effective shot peening method to improve corrosion resistance. Shot peening may have been introduced to the production of turbine discs for reasons other than corrosion resistance, but the benefits of refining this process with hot corrosion in mind could be significant.

Although the corrosion tests have successfully reproduced the type of corrosion found on jet turbine discs in service, they do not reproduce all the conditions that these components would be subjected to. The effect of hot corrosion on materials under stresses represents a logical step in the performance analysis of disc alloy materials.

In a journal article by J. A. Goebel and F. S. Pettit [9], the effect of transient oxides on the corrosion process was discussed. During their experimentation they attempted to reduce the transient oxide growth and subsequently observed a reduction in the rate of corrosion. Because transient oxides could potentially add a great deal of complexity to the initial oxide melt, the removal of such species may have beneficial effects. Such a study should first investigate the extent of transient oxides on an alloy surface and the best method for removing them.

Thin film coatings are used to protect components in the hotter part of jet and industrial gas turbines [23]. This same technique could be applied to disc alloys to enhance their corrosion resistance if new alloys prove unsuitable for operation at elevated temperatures.

7. References

[1] Airbus (2009), *Airbus Global Market Forecast 2009-2028*, available at: http://www.airbus.com/en/corporate/gmf2009 (accessed 19/10/2009).

[2] Birks, N., Meier, G. H. and Pettit, F. S. (2006), *Introduction to the high-temperature oxidation of metals,* 2nd ed, Cambridge University Press, Cambridge, UK.

[3] Bornstein, N. S. and DeCrescente, M. A. (1969), "The relationship between compounds of sulfer and sulfidaion", *Transactions of the metallurgical society of A.I.M.E.,* vol. 245, pp. 1947-1952.

[4] Donachie, M. J. and Donachie, S. J. (2002), *Superalloys: a technical guide,* 2nd ed, ASM International, Materials Park,OH.

[5] Encinas-Oropesa, A., Drew, G. L., Hardy, M. C., Leggett, A. J., Nicholls, J. R. and Simms, N. J. (2008), "Effects of oxidation and hot corrosion in a nickel disc alloy", *Proceedings of the International Symposium on Superalloys,* pp. 609.

[6] Encinas-Oropesa, A., Nicholls, J. R. and Simms N.J. PhD thesis Cranfield University. School of Industrial and Manufacturing Science (2005), *Study of hot corrosion of single crystal superalloys and platinum-aluminide coatings \cA. Encinas-Oropesa,* .

[7] Gao, W. (1997), "Standard free energy change of formation per unit volume: A new parameter for evaluating nucleation and growth of oxides, sulphides, carbides and nitrides", *Materials Research Innovations,* vol. 1, no. 3, pp. 157-160.

[8] Giggins, C. S., Pettit, F. S., Pratt & Whitney Aircraft Group. Commercial Products Division and United States. Department of the Air Force. Office of Scientific Research (1979), *Hot corrosion degradation of metals and alloys - A unified theory,* Pratt & Whitney Aircraft Group.

[9] Goebel, J. A. and Pettit, F. S. (1970), "Na_2SO_4-induced accelerated oxidation /hot corrosion/ of nickel (Sodium sulfate induced accelerated oxidation of Ni and superalloys, investigating thermodynamics and reaction mechanism)", *Metallurgical Transactions,* vol. 1, pp. 1943-1954.

[10] Goebel, J. A., Pettit, F. S. and Goward, G. W. (1973), "Mechanisms for the Hot Corrosion of Ni-Base Alloys", *Metall.Trans,* vol. 4, no. 1, pp. 261-278.

[11] Goodger, E. M. (1993), *An appreciation of hydrocarbon fuel chemistry with particular reference to aviation,* Landfall Press, Norwich.

[12] Goodger, E. M. (1994), *An overview of jet fuel supply and quality,* Landfall Press, Norwich.

[13] Hagel, W. C. and Seybolt, A. U. (1961), "Cation Diffusion in Cr_2O_3", *Journal of the Electrochemical Society,* vol. 108, no. 12, pp. 1146-1152.

[14] Hardy, M. C., Zirbel, B., Shen, G. and Shankar, R. (2004), "Developing Damage Tolerance and Creep Resistance in a High Strength Nickel Alloy for Disc Applications", in TMS, , pp. 83-90.

[15] Horton, G. (2006)*, Forecasts of CO_2 emissions from civil aircraft for IPCC*, available at: http://www.berr.gov.uk/files/file35675.pdf (accessed 11/15).

[16] International Air Transport Association (2009)*, International air transport association annual report 2009*, available at: http://www.iata.org/pressroom.htm (accessed 11/16).

[17] J. H. Chen, P. M. Rogers, J. A. Little (1997), "Oxidation Behavior of Several Chromia-Forming Commercial Nickel-Base Superalloys", *Oxidation of metals,* vol. 47, pp. 381-410.

[18] Khanna, A. S. (2002), *Introduction to high temperature oxidation and corrosion,* ASM International, Materials Park, OH.

[19] Kofstad, P. (1988), *High temperature corrosion,* 2nd ed, Elsevier Applied Science, Barking, UK.

[20] Levin, E. M., Robbins, C. R. and McMurdie, H. F. (1964), "Phase Diagrams For Ceramists", American Ceramic Society.

[21] Luthra, K. L. and Shores, D. A. (1980), "Mechanism of Na_2SO_4 Induced Corrosion at 600°-900°C", *Journal of the Electrochemical Society,* vol. 127, no. 10, pp. 2202-2210.

[22] McKee, D. W., Shores, D. A. and Luthra, K. L. (1978), "Effect of SO_2 and NaCl on High Temperature Hot Corrosion", *Journal of the Electrochemical Society,* vol. 125, no. 3, pp. 411-419.

[23] Nalin, L., Simms, N.J. and Nicholls, J.R. MSc thesis Cranfield University. School of Applied Sciences (2008), *Degradation of environmental protection coatings for gas turbine materials,* .

[24] Nicholls, J. R. and Hancock, P. (1983), "Analysis of oxidation and hot corrosion data - a statistical approach.", in Rapp Robert A. (ed.), *High Temperature Corrosion.* San Diego, CA, USA, NACE, Houston, Tex, USA, pp. 198.

[25] Nicholls, J. R. and Simms, N. J. (2010), "Gas Turbine Oxidation and Corrosion", in J.A. Richardson (ed.) *Shreir's Corrosion,* Elsevier, Oxford, pp. 518-540.

[26] Nicholls, J. R., Simms, N. J. and Encinas-Oropesa, A. (2007), "Modelling hot corrosion in industrial gas turbines", *Materials at High Temperatures,* vol. 24, no. 3, pp. 149-162.

[27] Rapp, R. A. (2002), "Hot corrosion of materials: a fluxing mechanism?", *Corrosion Science,* vol. 44, no. 2, pp. 209-221.

[28] Rapp, R. A., Devan, J. H., Douglass, D. L., Nordine, P. C., Pettit, F. S. and Whittle, D. P. (1981), "High temperature corrosion in energy systems", *Materials Science and Engineering,* vol. 50, no. 1, pp. 1-17.

[29] Reddy, U. C., Blanchard, C. E. and Schlein, B. C. (2011), "FT8-3 advanced low emissions combustor design", *Journal of Engineering for Gas Turbines and Power,* vol. 133, no. 11.

[30] Reed, R. C. *The superalloys: fundamentals and applications,* , Cambridge University Press UK, 2006.

[31] Rolls-Royce Ltd (2005), *The jet engine,* 'Late ' ed, Rolls-Royce, London.

[32] Saravanamuttoo, H. I. H. (2008), *Gas turbine theory,* 6th ed, Pearson Prentice Hall, Upper Saddle River, N.J.

[33] Schütz, M. (1995), *Protective oxide scales and their breakdown, John* Wiley and sons, Chichester, UK.

[34] Simms, N. J., Heikinheimo, L., Encinas-Oropesa, A., Tuurna, S., Kilgallon, P. J., Nicholls, J. R. and Oakey, J. E. (2003), "Predicting type II hot corrosion in industrial gas turbines", *Journal of Corrosion Science and Engineering,* vol. 6, p 25.

[35] Sims, C. T. and Hagel, W. C. (1972), *The superalloys,* Wiley-Interscience, New York.

[36] Smith, P. J., Nicholls, J. R. and Simms N.J. PhD thesis Cranfield University. School of Industrial and Manufacturing Science (1994), *Predicting hot corrosion rates under coal fired combined cycle power plant conditions,* .

[37] Soares, C. (2008), *Gas turbines*, Butterworth-Heinemann, Amsterdan ; Boston.

[38] Stoloff, N. S., Sims, C. T. and Hagel, W. C. (1987), *Superalloys II,* Wiley, New York.

[39] United Nations Framework Convention on Climate Change (1997)*, Kyoto Protocol*, available at: http://unfccc.int/kyoto_protocol/items/2830.php (accessed 11/16).

[40] Wood, G. C. and Stott, F. H. (1987), "Oxidation of alloys", *Materials science and technology,* vol. 3, no. 7, pp. 519-530.

[41] Wood, G. C. and Chattopadhyay, B. (1970), "Transient oxidation of Ni-base alloys", *Corrosion Science,* vol. 10, no. 7, pp. 471-476, IN1-IN3, 477-480.

[42] Zhang, T.-. and Hou, X.-., (2011), *NOx emission control in gas turbines*, Applied Mechanics and Materials (Nanchang ed), vol. 66-68, pages 319-321.